Politecnico di Torino

Master's Degree in Mechanical Engineering
A.a. 2023/2024
Graduation Session of July 2024

Optimization of a simulation framework for assessing the NVH signature of an electric drive unit

Supervisors:

D'Ambrosio Stefano

Salamone Nicolò

Candidate:

Rulfi Enrico

Dedicato ai miei genitori Bruna e Umberto,
alle mie sorelle Vittoria e Marianna
ed a Noemi
Che mi hanno accompagnato
in questi 5 anni

Abstract

Electric motors are one of the most crucial components in today's industrial landscape. With the introduction of new components and the inherent challenges posed by range limitations in electric mobility, performance parameters like energy consumption have become even more critical. Electric motor manufacturers increasingly recognize that energy efficiency must be complemented by acoustic performance. Integrating sound quality markers into optimization objectives is essential for designing higher-quality electric machines. Although the noise produced by electric drives is generally less than their Internal Combustion Engines (ICEs) counterparts, it often features high tonal components that significantly compromise sound quality. Additionally, structural resonances can exacerbate these effects, further impacting the overall acoustic performance.

This work focuses on the vibroacoustic response of a Permanent Magnet Synchronous Motor (PMSM), an electric motor designed by the Electrical Engineering Department at Universitat Politècnica de Catalunya (UPC), and kindly made available for this analysis. The e-motor is characterized by five pairs of magnetic poles, internal permanent magnets and is powered by three-phase currents. These currents are provided by an inverter and the modulation technique is the Pulse Width Modulation (PWM).

The Noise Vibration and Harshness (NVH) problem is based on the presence of harmonics in the electromagnetic (EM) forces that are generated in the motor. These harmonics are linked to the topology of the machine and the presence of current ripples which respectively cause low and high frequency harmonics. The topology of the machine is responsible for the so-called "slotting effect" while the current ripples are a direct consequence of the modulation of the currents, performed by the inverter.

A digital framework that combines different simulation environments is modeled to recreate the vibroacoustic behavior of the PMSM. A high-frequency, linear, 1D model of the electric drive unit is designed to estimate the phase currents and the rotor's angular position in the time domain. These results are employed in a 2D electromagnetic FE model to estimate the air gap's magnetic forces. While the conventional workflow included a complete section of the electric motor as the 2D electromagnetic model, for this analysis these results are employed in a partial one, consisting of only an angular sector. The comparison between this reduced model and the complete one highlights a significant gain in computational time and results size.

A complete structural FE model is then built to obtain the structural modes of the stator of the motor. Finally, the vibroacoustic simulation based on a 3D model of the stator is matched to the structural modes and the EM forces from the 2D simulation in order to obtain the sound pressure level at a microphone point outside the stator.

The results obtained from the digital framework, referred to as the "Finite Element framework", are then compared to those from an alternative simulation framework. A State Space framework is developed with the goal of producing results more quickly and with lower computational demands. This data-driven State Space model is derived from a series of frequency response functions.

Table of Contents

List of Tables

List of Figures

Acronyms

ICE

Internal Combustion Engines

PMSM

Permanent Magnet Synchronous Motor

UPC

Universitat Politècnica de Catalunya

PWM

Pulse Width Modulation

NVH

Noise Vibration and Harshness

FE

Finite Elements

EM

Electromagnetic

FRF

Frequency Response Function

AC

Alternating Current

DC

Direct Current

RMS

Root mean square

dq0

Direct-quadrature-zero reference frame

CAE

Computer Aided Engineering

FEA

Finite Elements Analysis

CFD

Computational Fluid Dynamics

ATVs

Acoustic Transfer Vectors

AML

Automatic Matched Layer

SPL

Sound Pressure Level

1. Introduction

The growing concern about climate change and the race to design more energy-efficient propulsion systems led to the increased use of PWM-fed permanent magnet synchronous motor. Electric motor manufacturers are increasingly realizing that this must be complemented by including acoustic behavior. Indeed, incorporating sound quality markers into optimization objectives is useful in order to design more high-quality electric machines.

In the acoustic analysis of electric machines, electromagnetic noise is the most significant component, with mechanical and aerodynamic effects generally being neglected [1]. EM noise is caused by the excitation of the machine's active elements through magnetostriction and reluctance forces. Since the magnetostriction effect on noise generation can typically be ignored [2], the primary contributors are the reluctance forces originating from the air gap. These forces' radial components are absorbed by the rotor and stator, resulting in elastic deformation and subsequent vibrations [3].

The harmonics that compose the stresses have high-pitch components directly resulting from the use of PWM [4]. This affects the acoustic behavior because the stresses lead to structural vibrations, which finally produce a pressure field radiated from the stator's outer surface to the surroundings. As a consequence, the sound quality is then compromised due to the high tonal nature of the generated noise [1]. This effect can be aggravated by the presence of structural resonances. Vibro-acoustic simulation and analysis must be performed early in the design process to prevent these issues from happening [4].

This work focuses on the vibroacoustic response of a PMSM, an electric motor designed by the Electrical Engineering Department at Universitat Politècnica de Catalunya, and kindly made available for this analysis. The e-motor is characterized by five pairs of magnetic poles, internal permanent magnets and is powered by three-phase currents. The project has been carried out in Siemens Industry Software research headquarters in Leuven, Belgium. The simulations were conducted using proprietary software from the company, including Simcenter 3D and Simcenter Amesim.

In order to simulate accurately the Noise, Vibration and Harshness behaviour of the electric machine, a multiphysics simulation framework is built. Four different numerical models are employed in the framework.

A 1D functional model of an electric drive unit is developed to simulate the power electronics of the electric motor, aiming to estimate the phase currents and the rotor's angular position in the time domain. The model incorporates parameters specific to the power electronics, such as the carrier frequency. Initially, the model is configured to be linear, with constant physical parameters. However, to enhance the accuracy of the results, it is later refined to include spatially-dependent physical features. This represents the first major modification aimed at optimizing the simulation framework.

The electric drive unit model results are fed to the 2D Finite Element electromagnetic model of the section of the motor. The novelty of this work consists of the EM model being a partial one, consisting of an angular sector of 1/5 of the complete section of the motor. An in-depth analysis is performed focusing on the gains in terms of computational time compared to a complete model, without compromising accuracy. The electromagnetic model computes the EM stresses applied on the internal surface of the stator.

The EM stresses are the excitation input of the 3D complete FE model of the motor's stator [3], which performs the vibroacoustic simulation. An external point, positioned radially to the stator, is set as a target for the results, working as a virtual microphone point.

The fourth model implemented in the framework is the structural one, built to compute the modal analysis of the stator. The structural modes of the stator are then also fed to the 3D vibroacoustic model in order to obtain the acoustic pressure level considering the structural behavior of the stator itself.

The 1D functional model, the 2D electromagnetic model, and the two 3D vibroacoustic and structural models together constitute the "FE framework". The 1D model generates results that include phase currents and the rotor's angular position in the time domain. Initially, the simulation approach involved setting time limits based on a single electrical cycle, as the 2D model simulates 1/5 of a full rotor revolution, which corresponds to one electrical cycle. However, after further analysis, it was decided to extend the simulation time to cover multiple electric cycles. This adjustment was made to achieve more accurate results and further optimize the simulation framework. The output of the 2D electromagnetic model is the electromagnetic nodal force densities that originate in the air gap and act on the inner surface of the stator. Finally, the vibroacoustic simulation performed with the 3D model focuses on the sound pressure levels at the external microphone point.

In the final part of the project, an alternative analytical framework is created to replace the vibroacoustic model within the FE framework. The goal is to accelerate the simulation process and reduce computational costs. A data-driven State Space model is developed based on a series of frequency response functions. The identification of the State Space model is carried out through a modal-based approach [5]. The FRFs, calculated using the same vibroacoustic model from the FE framework, represent the transfer functions between the lumped EM forces applied to the stator's inner surface and the acoustic pressure level at the microphone point. The inputs of the State Space model are the lumped EM forces on the stator's inner surface, computed by a separate 2D EM model, resulting from integration of the nodal force densities over the entire tooth surface.

Finally, the acoustic pressure level results computed by the FE simulation framework and the State Space simulation framework are compared.

2. The electric motor

The electric motor is a fundamental component in modern engineering, employed in a wide array of applications, from household appliances to industrial machinery and electric vehicles. Its primary function is to convert electrical energy into mechanical energy, allowing motion and operation in countless devices. The efficiency, reliability, and versatility of electric motors have made them indispensable in advancing technology and improving energy utilization. In this chapter, a brief introduction of the different types of electric motors is presented, followed by the description of the specific electric motor analyzed in this thesis.

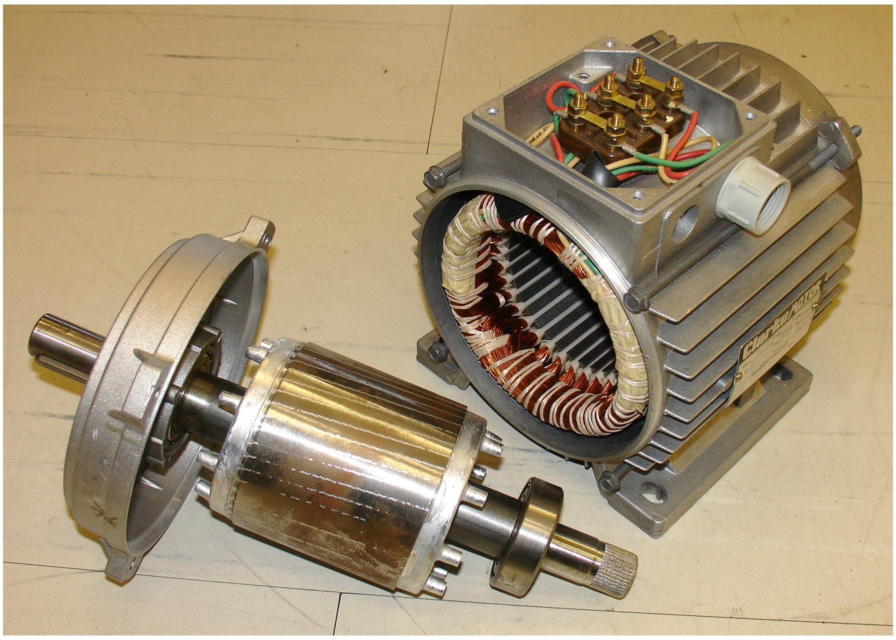

Figure 2.1: Disassembled electric motor.

2.1 Synchronous electric motors

Synchronous electric motors are AC machines where the operating speed is directly tied to the frequency of the voltage applied to the stator terminals. In steady-state conditions, the rotor rotates in sync with the magnetic field generated by the stator. The currents in the stator coils are adjusted to match the required speed and torque at the shaft. These phase currents generate a magnetic field in the stator, which then interacts with the magnetic field of the rotor.

These machines were initially developed for AC power generation, especially in high-power applications. However, their use in medium and small power motors has become increasingly common in recent times. Figure 2.2 illustrates a typical 2-pole-pair, 3-phase synchronous motor. The black lines depict the stator magnetic field lines, which drive the rotor magnets—schematically represented—to rotate in sync with the stator field.

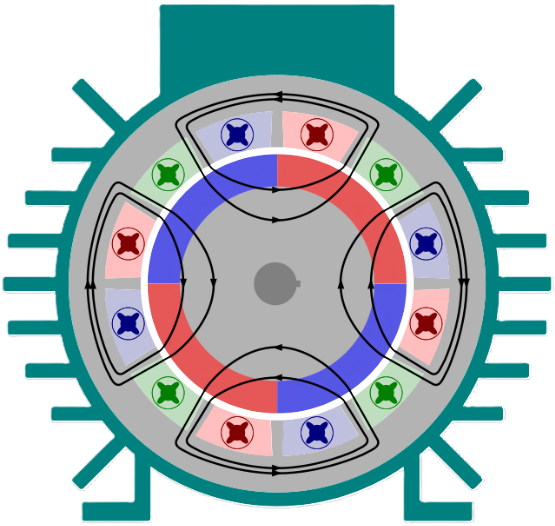

Figure 2.2: Synchronous motor's working principle.

Synchronous machine differentiation is based on the rotor structure:

- **Externally excited motors**, that require DC to magnetize the rotor. The currents flow in the coil windings that envelop the rotor core magnetic poles inducing the magnetic field. Figure 2.3 shows the red coil windings and the so-called damper windings: a short-circuited winding at the top of the rotor poles used to damper the transient oscillation and facilitate the start-up operation [6]. When running at synchronous speed the damper windings carry no current, as there is no slip, but any deviation from synchronous speed, will create slip and induce a current and hence damping torque, which will serve to reduce the magnitude of the transient oscillations or disturbance.
- **Reluctance machines**, a type of non-excited electric motor that induces non-permanent magnet magnetic poles on the ferromagnetic rotor. The rotor does not have any windings and it generates torque through magnetic reluctance. In the aligned position, when the rotor poles' angular position coincides with the stator poles one, the magnetic reluctance is minimized. Once the stator magnetic field starts to rotate, the rotor is dragged into rotation to keep minimal magnetic reluctance, so mechanical torque is created [7]. Figure 2.4 shows the moment when the stator fields lead by a small angular value the rotor magnetic poles.

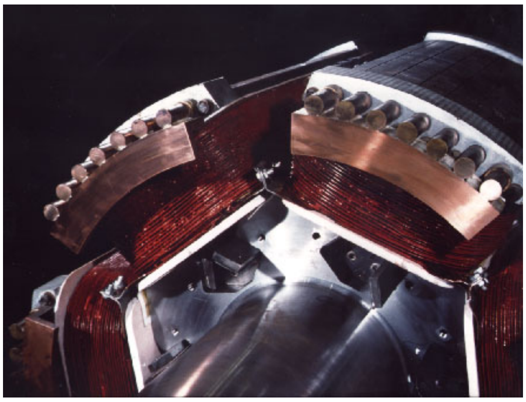

Figure 2.3: Externally exited rotor.

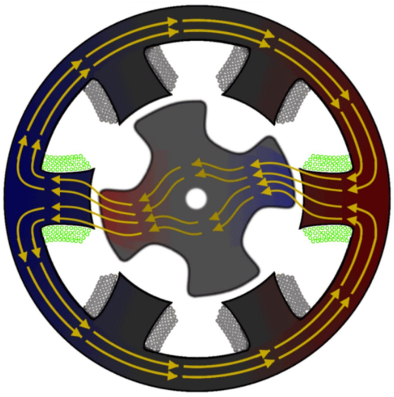

Figure 2.4: Reluctance machine.

- **Hysteresis machines**, that generally have a solid cylindrical rotor made with high coercivity and magnetically hard cobalt steel. This means that the material has a wide hysteresis loop which leads to the need for a very high magnetic field to reverse the direction of magnetization [8]. The working principle consists of having the rotating magnetic field to cause each small volume of the rotor to experience a reversing magnetic field. Because of the large hysteresis loop, the magnetization direction of the material lags behind the phase of the stator magnetic field and this produces torque, as the material of the rotor tries to "catch up" in the revolving motion.
- **Permanent magnet synchronous motors**, discussed in an in-depth analysis in Section 2.2.

Another classification regarding synchronous electric motors is based on the rotor construction features:

- **Cylindrical rotor synchronous machines**, also identified as “round” rotor. These feature a uniform air gap, because the rotor poles do not need to project out the surface of the rotor. This leads to a significantly smaller inertia contribution, so the rotational speed can be higher, and the whole motor can be longer. These motors are suitable for high-speed applications.
- **Salient-pole rotor synchronous machines**. The air gap is not uniform because the rotor poles are projecting out from the surface of the rotor. These motors are generally smaller and are suitable for low-speed applications.

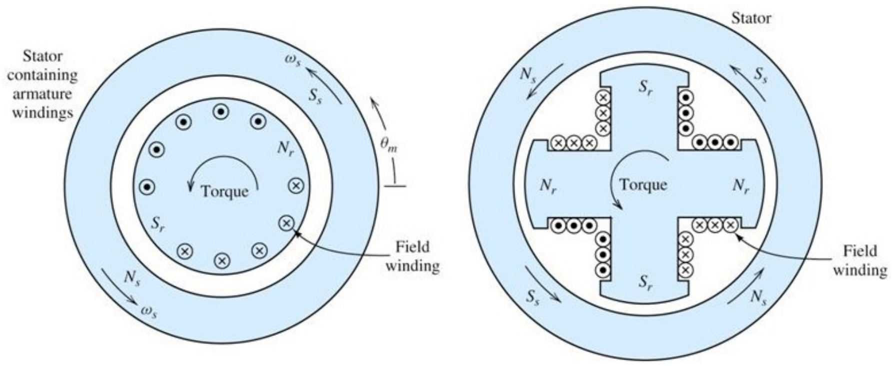

Figure 2.5: Rotor construction classification. Round rotor (left) and Salient-pole rotor (right).

2.2 Permanent magnet synchronous motors

In permanent magnet synchronous motors, permanent magnets are embedded in the rotor to create an homogeneous magnetic field. The rotor does not need currents to magnetize so it has generally lower mass and lower moment of inertia compared to the externally exited motor counterparts. Due to these advantages and the high power density and efficiency, PMSM are a very popular solution in electrical drives [9].

The classification is also based on the position of the magnets:

- **Internal permanent magnet**: the permanent magnets are embedded into the rotor. This is suitable for high-speed applications, because of the better mechanical performance. The air gap is uniform because PMSMs are generally cylindrical rotor synchronous machines. Figure 2.6 is a photograph of the case study PMSM.

  Internal permanent magnets include also the so-called "flux barrier" inside the rotor, as it can be observed in Figure 2.6. A schematic representation of the position of the magnets, which are absent in the photograph, highlights the presence of air on the side of the magnets. The void space is designed to prevent the magnetic field lines from closing in between two different magnets and as a result, the overall performance of the electric motor is increased [10].

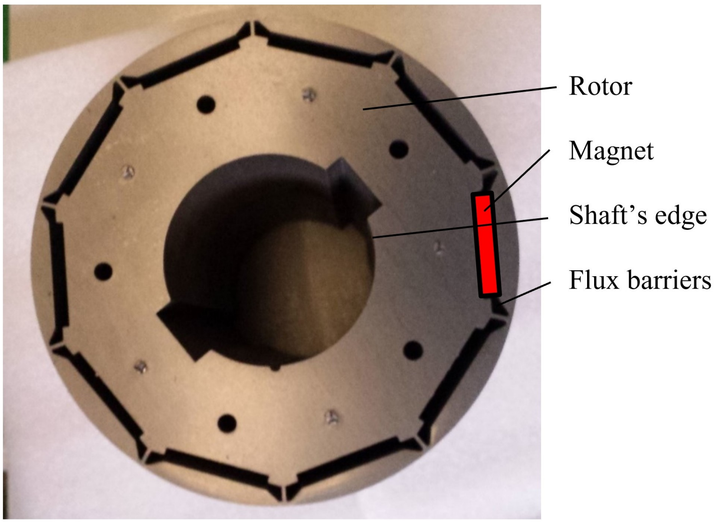

Figure 2.6: Internal permanent magnet synchronous motor’s rotor.

- **Surface Permanent Magnet (SPM)**: In this configuration, the magnets are mounted on the surface of the rotor. The presence of salient poles causes the air gap permeability to be non-uniform. Consequently, the mechanical strength of the magnets is lower, which limits the motor's maximum safe mechanical speed. Figure 2.7 illustrates an example of a surface permanent magnet motor.

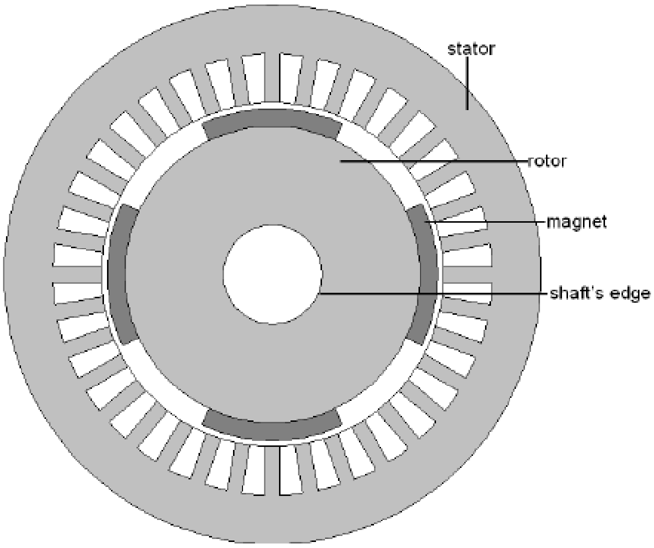

Figure 2.7: Surface permanent magnet synchronous motor.

2.3 The case study

The subject of this analysis is the distributed winding internal permanent magnet synchronous motor designed by the Electrical Engineering Department at UPC. The e-motor is characterized by five pairs of magnetic poles, internal permanent magnets and is powered by three-phase currents. Figures 2.8 and 2.9 are two photographs of the electric motor.

Tables 2.1 and 2.2 list the salient physical characteristics of the electric motor and its materials:

Rotor type	Round
Rotor magnetic field source	Permanent magnet
Magnet position	Internal
Number of pole pairs	5
Number of phases	3
Number of slots	30
Stator outer diameter	200 mm
Rotor outer diameter	137 mm
Stack length	150 mm
Air gap thickness	1.2 mm

Table 2.1: Salient characteristics of the electric motor.

Rotor Core	Electric steel M270-35A
Stator Core	Electric steel M270-35A
Permanent magnet	Neodymium magnet N40SH
Coil Windings	Copper

Table 2.2: Materials of the electric motor.

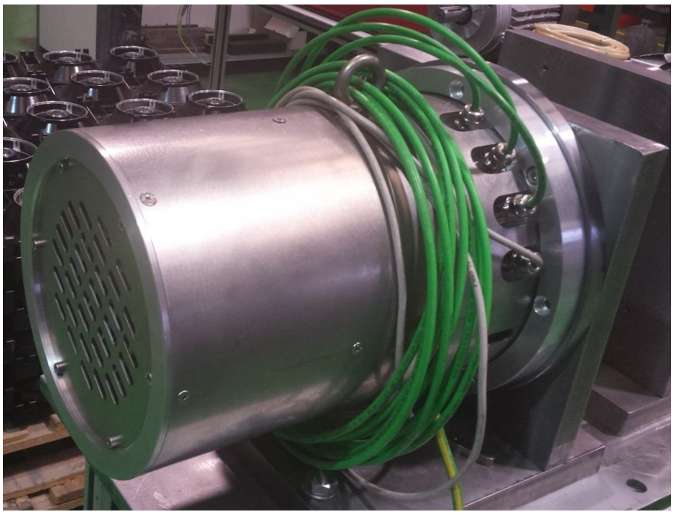

Figure 2.8: The assembled electric motor.

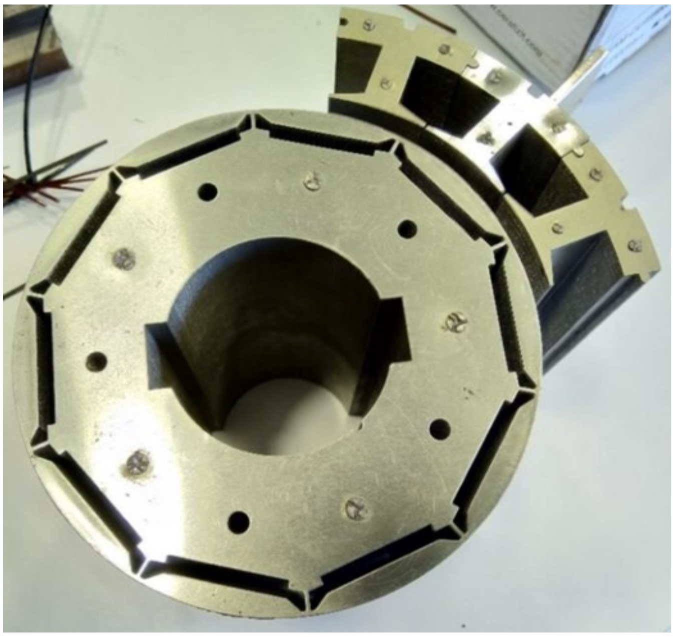

Figure 2.9: Stator teeth and rotor.

3. E-motor noise

The noise produced by a rotating electric machine can be categorized into three distinct components: electromagnetic, mechanical, and aerodynamic [11]. Among these, electromagnetic noise is the most significant, primarily resulting from the excitation of the machine's active elements by magnetostriction and reluctance forces [1]. While the impact of magnetostriction is generally negligible, reluctance forces are the primary contributors of noise generation [2]. Maxwell stresses mathematically formalize how reluctance forces arise due to the magnetic field interacting with materials of different magnetic permeabilities [12]. In this project, Maxwell stresses are computed by the 2D FE electromagnetic model implementing the Maxwell tensor within the FE method, as described in Section 6.3.

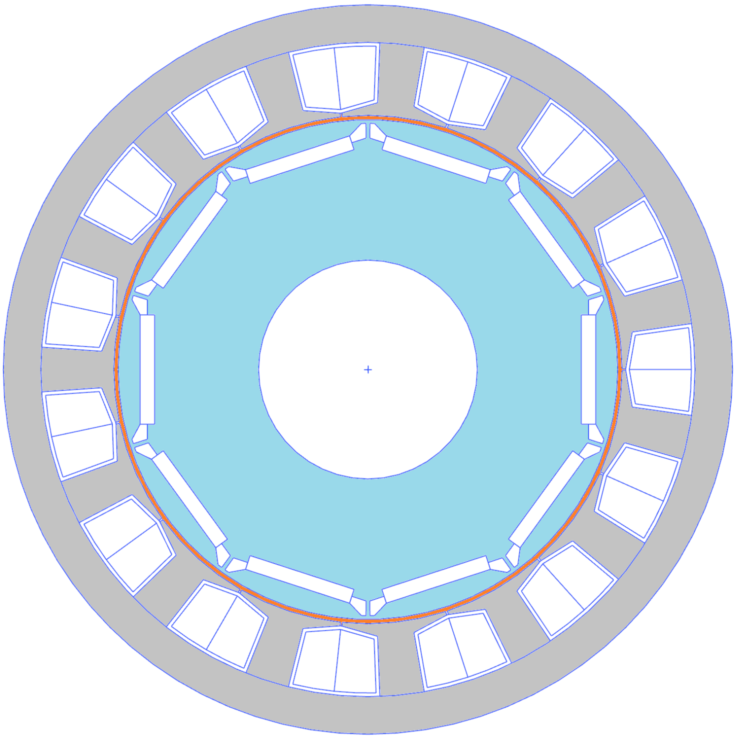

Figure 3.1: Section of the PMSM. Air gap (orange) between the stator (grey) and the rotor (light blue).

The net tangential reluctance force exerted on the rotor determines the average electromagnetic torque of the electrical machine. However, tangential and radial harmonics in this force can lead to unwanted vibrations and acoustic noise [11]. The primary contributor to acoustic noise in electric machines is the reluctance force that arises in the air gap between the stator and rotor, acting on the inner surface of the stator. The normal component of this reluctance force is the main responsible for the acoustic noise [12]. When the dynamic excitation of the magnetic forces matches the frequency of a structural mode of the stator, resonance occurs, significantly amplifying vibrations and acoustic emissions.

Regarding the electromagnetic noise, two distinct effects are notable:

- The slot-to-pole interaction influenced by the machine's topology;
- The generation of high-frequency harmonics in the stator currents due to modulation control in power electronics.

The slot-to-pole interaction, also called "slotting effect" is one of the main sources of acoustic noise and vibrations [13]. It refers to the impact of the stator and rotor slots on the motor's electromagnetic performance, particularly in terms of noise and vibration. The slots create periodic variations in the air gap magnetic field, which induce harmonic components in the electromagnetic forces acting on the motor.

High-frequency harmonics in the stator currents, induced by Pulse width modulation control, can produce high-pitched components in the acoustic noise of electric machines [9]. These harmonics are created because the PWM signal is not a pure sine wave but rather a series of pulses that approximate a sine wave. This pulsed nature of the PWM closely correlates with the carrier frequency, a key characteristic of PWM. The switching actions of transistors in the inverter arms are directly responsible for the current ripples in the stator coils, which affect the magnetic field in the air gap and ultimately the electromagnetic forces acting on the inner surface of the stator.

The vibrations of the motor structure and the consequent propagation of sound waves are influenced by the presence of both the slotting effect and PWM-related harmonics, leading to distinct peaks in the acoustic pressure level frequency spectrum.

4. The simulation frameworks

In order to simulate accurately the Noise, Vibration and Harshness (NVH) behavior of the electric machine, two distinct simulation frameworks are built. The first simulation framework will be referred to as the "Finite Element framework", and the second one as the "State Space framework". Both compute the acoustic pressure level on a microphone point placed outside the electric motor, and the results are compared in Chapter 11.

4.1 Finite Element simulation framework

Four different numerical models are implemented in the framework:

- 1D, non-linear, functional model of an electric drive unit;
- 2D, Finite Element, partial, electromagnetic model of the section of the motor;
- 3D, Finite Element, structural model of the stator;
- 3D, Finite Element, vibroacoustic model of the stator.

Figure 4.1 illustrates the FE simulation framework with information about the software used to build the models and the data flowing from one to another.

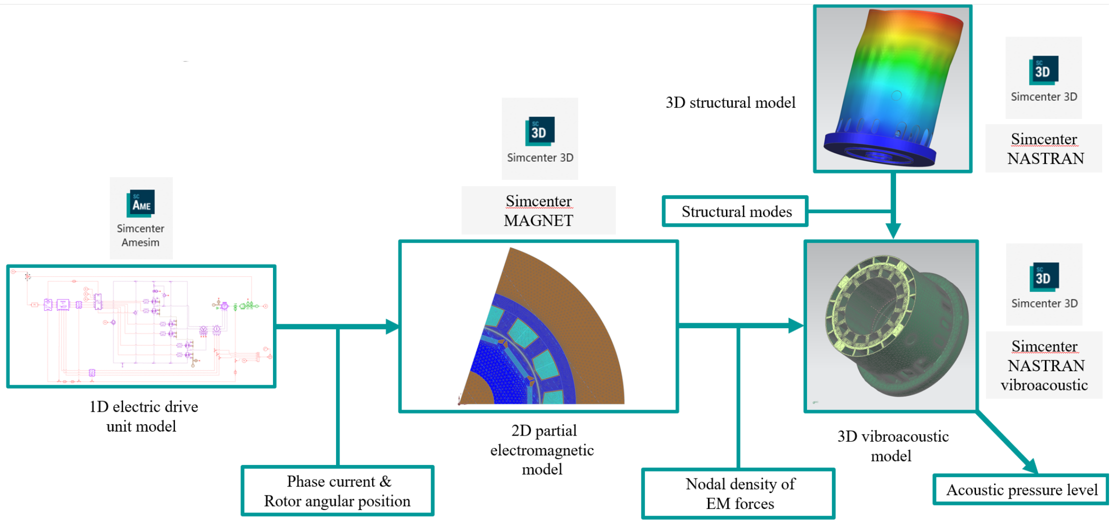

Figure 4.1: The FE simulation framework.

The 1D functional model of the electric drive unit returns the phase currents and the rotor angular position in steady state conditions. This model is built in Simcenter Amesim 2304, a commercial simulation software for the modeling and analysis of multi-domain systems. The simulation is set up with a rotational speed and the results will relate to that.

The 2D electromagnetic FE model is a partial representation, covering only an angular sector equivalent to 1/5th of the total motor section. This corresponds to a 5-pole-pair synchronous motor, where the rotor's angular sector during one electrical cycle spans exactly 1/5th of a complete revolution. After further evaluation, it was decided to simulate one full revolution of the electric motor using this partial model. This is made feasible thanks to the periodic boundary conditions implemented in the model. The solver calculates reluctance forces in the air gap, and the output consists of nodal electromagnetic forces applied to the stator's inner surface, corresponding to the temporal domain of the electrical cycle. The analysis is conducted under steady-state conditions at a specific rotational speed, which remains constant throughout the simulation.

Prior to input into the 3D vibroacoustic model, the nodal force outputs undergo preprocessing. Initially, values from the partial model are extended along the entire internal circumference of the stator and then extruded to its full stack length. Subsequently, these resultant nodal forces are mapped onto the surfaces of the three-dimensional FE elements constituting the stator teeth. Finally, a Fourier Transform is applied, computing the vibroacoustic model frequency-domain dynamic excitation, spanning from 0 Hz to 12500 Hz.

The vibroacoustic model couples the mode set of the structure, consisting of the mode shapes of the assembly and its natural frequencies, to the excitation in the form of the preprocessed nodal forces. The result is the vibroacoustic frequency response of the structure. The target point for the acoustic pressure level is a virtual microphone positioned radially with respect to the stator casing. This analysis combines the nodal results from different rotational speeds computing the vibroacoustic response for each of them.

The structural 3D model of the stator consists of the different elements of the stator assembled and accurately constrained. The materials' features are assigned to the different elements to represent accurately the modal behavior of the stator. The simulation returns the information about the mode shape of the assembly and its modal frequency, which will be fed to the vibroacoustic simulation introduced in the following paragraph.

The 2D electromagnetic model, the 3D vibroacoustic model and the 3D structural model are built in Simcenter 3D CAD environment, but the solver algorithm used for the simulation is different for each one of them. The 3D vibroacoustic model runs on Nastran Vibroacoustic, the 3D structural model runs on Nastran, while the 2D electromagnetic model runs on Magnet.

The detailed descriptions of the 1D electric drive unit model, the 2D partial electromagnetic model, the 3D structural model, and the 3D vibroacoustic model are provided sequentially in Chapters 5 through 9. The results of the FE simulation framework are presented in Chapter 11.

4.2 The State Space simulation framework

The State Space framework computes the acoustic pressure level at the same microphone point as the FE framework. This is achieved by substituting the 3D vibroacoustic and 3D structural models of the FE framework with a State Space model. The 1D electric drive unit model remains the same as in the FE framework and computes the rotor angular position and three-phase currents, which are then extracted and resampled to be used as inputs to the subsequent 2D electromagnetic model. Unlike the partial model implemented in the FE framework, the 2D electromagnetic model is a complete section model of the electric motor. It computes the lumped EM forces acting radially on selected points on the inner surface of the electric motor in the time domain. The signal lengths of the currents, rotor angular position, and lumped EM forces are matched to those of the FE framework counterparts for the specified rotational speed, facilitating a direct comparison between the final results. These lumped EM forces serve as inputs to the State Space model, which is designed to compute the acoustic pressure level at the microphone point.

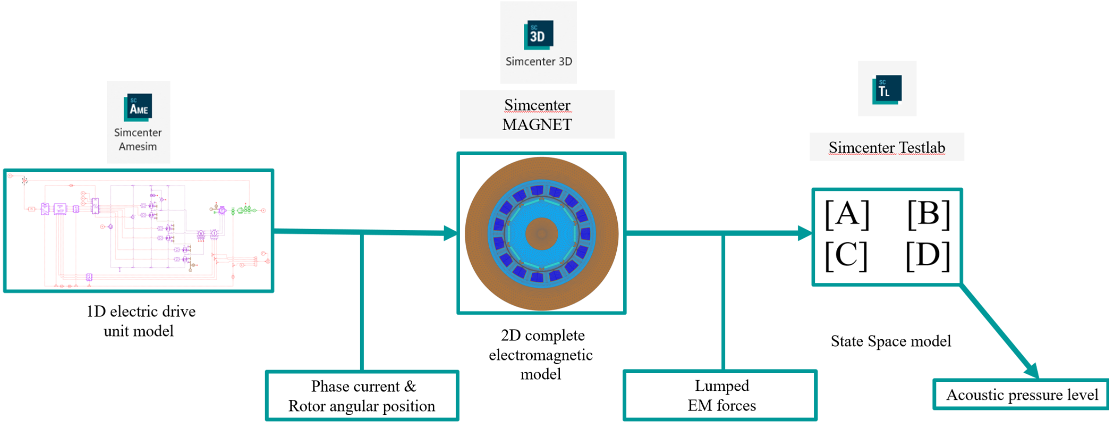

Figure 4.2: The State Space simulation framework.

The 1D electric drive unit model, shared by both frameworks, is described in Chapter 5. The complete 2D electromagnetic model and the State Space model are detailed in Chapter 9 and Chapter 10, respectively. The results of the State Space model are presented in Chapter 12, followed by a comparison of the acoustic pressure levels between the two different models.

5. The 1D electric drive unit model

The 1D, non-linear, functional model of an electric drive unit is set up to model the power electronics of the electric motor. It's a lumped parameter model working with block diagrams interacting one another.

The model is set up with the power electronics parameters, such as the carrier frequency, which is one of the control parameters in the analysis, and offers the possibility to change the PWM modulation strategy. The simulation also refers to a certain rotational speed of the rotor and the results consist of the phase currents of the rotor's winding and the angular position of the rotor. The simulation environment is Simcenter Amesim 2304, a commercial simulation software for the modeling and analysis of multi-domain systems.

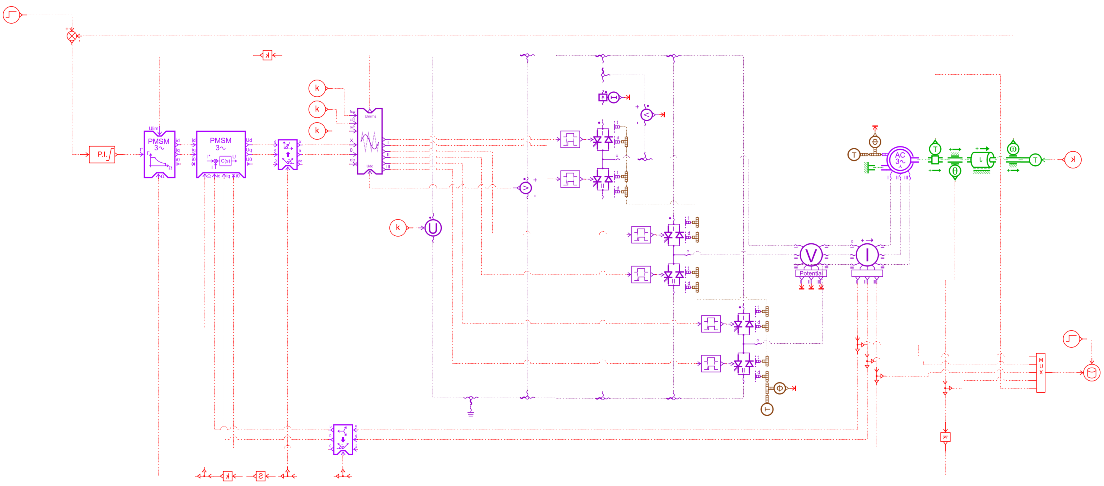

Figure 5.1: The 1D electric drive unit model.

5.1 Simcenter Amesim

The software used to design the electric drive unit model is Simcenter Amesim 2304, developed by Siemens Digital Industry Software. Its purpose is the modeling and analysis of multi-domain systems. This approach gives the capability to simulate the behavior of a system before the detailed CAD modeling are completed. The software is equipped with tools used to model, analyze and predict the performance of mechatronics systems. Models are built by linking different icons, as shown in Figure 5.1, each of them represents a submodel. Submodels are described by time-dependent analytical equations. The icons can have multiple inputs and outputs and causality is enforced by linking the input of one icon to the output of another.

While Matlab Simulink, the other commonly used software for modeling multidomain dynamic systems, enforces the casualty transferring a signal as the flow of information from one icon to the other, Simcenter Amesim implements the Bond graph theory [14]. The Bond graph theory is a graphic modeling approach that uses the transfer of energy as bonds between two graphical entities like the icons in the Amesim environment [15]. Power flowing from one submodel to another in the Amesim model can have different forms depending on the type of model it's linked to. For mechanical submodels of rotating machines, power is in the form of rotational speed and torque, while in electrical ones it's in the form of voltage and currents. Only the red lines visible in Figure 5.1 are the exception: those links transfer the information in the form of signals.

In Figure 5.2 it's possible to observe an example of energy transferred between two different icons of the model as bonds between the two entities they refer to: mechanical power in the form of torque C and rotational speed ω. In this specific case the two entities are the AC motor, on the left, and the torque sensor, on the right. The AC motor uses as input the rotational speed which is the output of the torque sensor, while the torque flows in the opposite direction: from the AC motor outputs to the torque sensor.

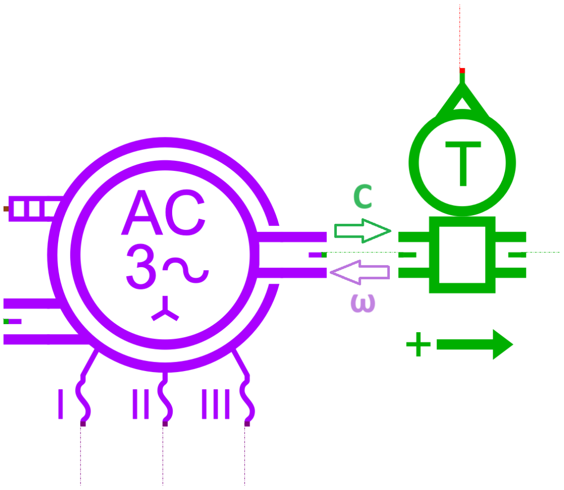

Figure 5.2: e-motor block (left) and torque sensor block (right).

5.2 The control loop

A control loop is a fundamental component of feedback control systems. They are used as control strategies and enable continuous monitoring and adjustment of system variables to maintain desired performance levels. By integrating sensors to detect process variables and controllers to analyze and respond to deviations from set points, control loops ensure that machines and devices operate reliably and efficiently.

There are two primary types of control loops: *open* and *closed*. An open control loop, also known as feedforward control, relies solely on the initial input and does not directly measure the output or account for deviations. It assumes a predictable relationship between input and output, making adjustments based on expected behaviors without real-time feedback. In contrast, a closed control loop, or feedback control, continuously compares the actual output with the desired target through feedback sensors. The controller adjusts the input based on these measurements, correcting deviations and maintaining stability and accuracy in varying operating conditions. Closed control loops are essential for systems requiring precise regulation and responsiveness, such as robotic arms, automated manufacturing processes, and advanced vehicle control systems. They ensure that any disturbances or changes in the environment are compensated for, optimizing overall system performance and reliability.

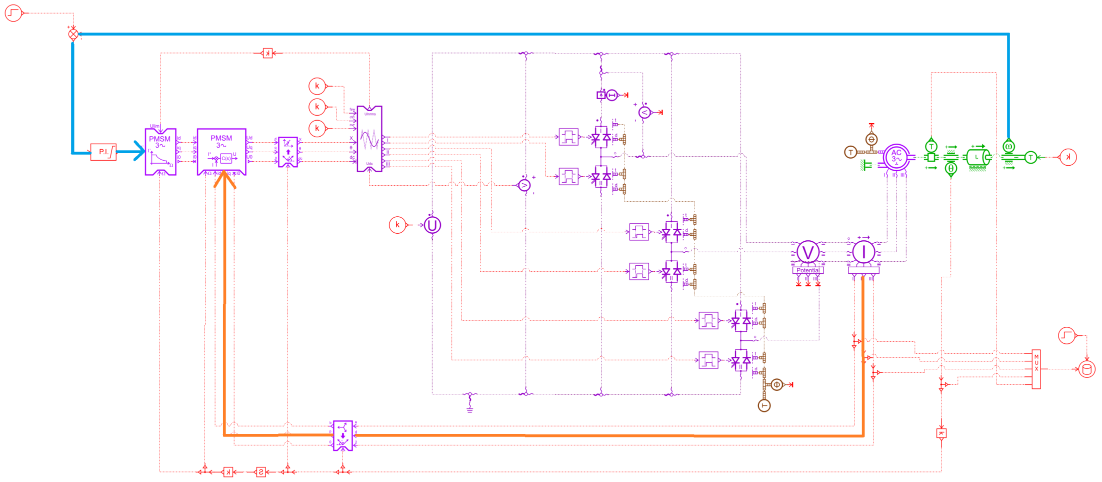

Figure 5.3: The rotational speed control loop (light blue) and the currents control loop (orange).

In particular, the model features two different closed control loops, as seen in Figure 5.3, the first one is highlighted in light blue and regulates the rotational speed of the e-motor while the second, which is nested inside the first one, regulates the 3 phase currents. The rotational speed control loop starts on the right at the speed sensor icon. The rotational speed information flows to the left, where it is compared with the reference speed and then used as feedback for the control algorithm.

The nested control loop, highlighted in orange, begins on the right at the icon representing the three-phase current sensor. The current information follows the orange line until it reaches an icon that processes the current signals to perform the Clarke and Park transformations [16]. This icon also requires the rotor's angular position, obtained from a branch coming from the bottom, linked to an angular sensor on the right. The output of this block is the transformed current signal, which leads to the PMSM control block. Here, it is compared with the reference currents and used as feedback by the control algorithm.

To better understand the mechanism of the model control loops, the following section focuses on the submodels used to implement the control algorithms.

5.3 The submodels

Each of the model's blocks implements a mathematical submodel that handles and manipulates the input information to compute the outputs. The submodels of most interest are those related to the control loops and the modeling of the electric motor. In Figure 5.4, the different blocks of interest are labeled, whose submodels will be investigated.

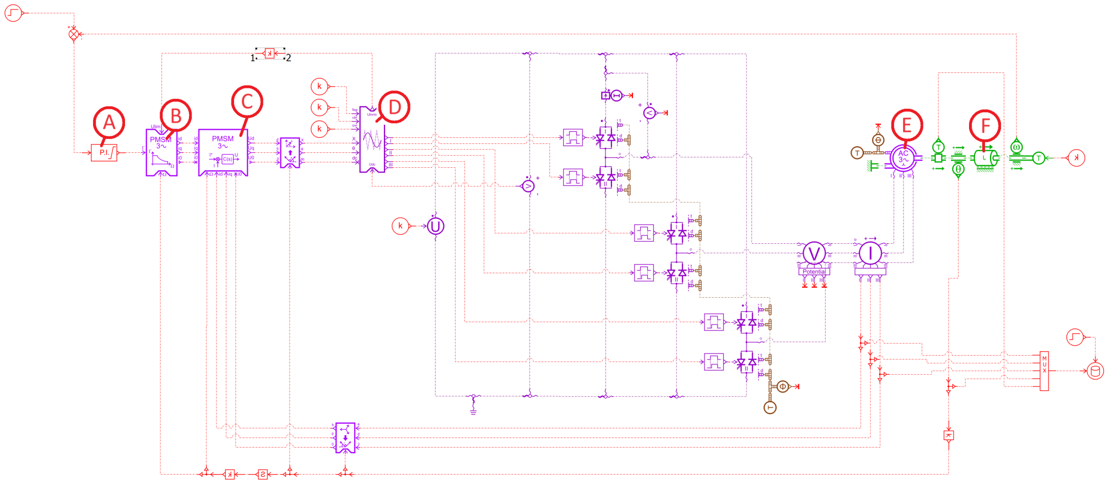

Figure 5.4: Blocks' labels.

Label	Block
A	Proportional-Integral controller
B	Torque controller
C	Current controller
D	Carrier-Based PWM controller
E	Electric machine
F	Rotary load

Table 5.1: Blocks' labels and denomination.

5.3.1 Proportional-Integral controller

This block serves as a Proportional-Integral controller, a widely used control mechanism in industrial applications due to its simplicity and effectiveness. The PI controller combines two control actions: the proportional term, which provides a control signal proportional to the error between the desired setpoint and the measured process variable, and the integral term, which accumulates the error over time and adjusts the control signal to eliminate steady-state errors. By tuning the proportional and integral gains, the PI controller can achieve a balance between fast response and stability, making it suitable for systems requiring precise and stable control.

$$u = K_p e + K_i \int_{t_{\text{start}}}^{t} e \, dt \tag{5.1}$$

where:

- u is the control output;
- e is the error signal;
- K_p is the proportional gain;
- K_i is the integral gain.

The error e is the delta between the reference and effective values of the rotational speed of the machine. The output of this equation is the torque request to the electric motor to operate at the desired speed with minimal error. The gains K_p and K_i have been tuned manually, with trial and error and observing the system response in order to need the shortest time possible to get to steady state conditions. This was possible thanks to the fact that the model operating conditions are transient, and the reference speed has a step behavior that then remains constant for the entire duration of the simulation, as explained in depth in section 5.5.

The controller also implements an anti-windup method called step-integration. The anti-windup method in PI controllers is a technique used to prevent the integrator component from accumulating excessively when the controller output is saturated and unable to increase further [17]. This is achieved by limiting the integrator's growth or by providing feedback to reduce its effect when the actuator is at its maximum or minimum limit, thereby improving the system's stability and response time.

The step-integrator anti-windup approach is the step-integrator method, which adjusts the integrator's input based on the difference between the saturated and unsaturated outputs, preventing the integrator from winding up during saturation [18].

The following table contains the PI controller gains determined in the manual tuning procedure:

Gains	**Values**
K_p	2
K_i	50

Table 5.2: PI Controller Gains.

5.3.2 Torque controller

This block serves as a torque control block for interior and surface mounted PMSM. It computes the machine's current targets to satisfy the torque request in order to close the gap between the reference and the effective value of rotational speed. This particular block offers the possibility to choose different submodels, linear or non-linear, to model accurately the controller of the e-machine. The approach that was followed for this block is to remain with a linear model, with constant physical parameters that do not depend on the angular position.

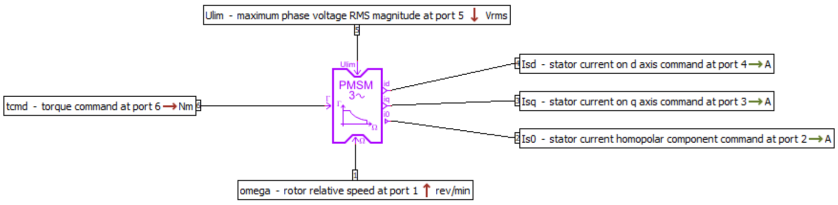

Figure 5.5: Torque controller block.

As can be seen in Figure 5.5 the inputs of the block are:

- The torque command coming from the PI controller;
- The maximum phase voltage coming from the Carrier-based PWM controller (analyzed in subsection 4.3.4), corresponds to the controlled machine maximum phase voltage RMS magnitude. This value is important in electric machine applications to ensure safe operation, optimize performance, and maintain precise control. For example, it prevents the saturation of the motor windings, which can occur if the voltage exceeds certain limits, leading to inefficient operation and potential damage;
- The rotor relative speed, necessary for the controller to locate the e-machine operating region at any moment [19].

The block computes as outputs:

- Direct stator current refers to the current component that is in phase with the magnetic field. It aligns with the d-axis in the rotor reference frame [16] contributing directly to the magnetic flux;
- Quadrature stator current is the component perpendicular to the magnetic field and leads or lags the direct current by 90 degrees. It aligns with the q-axis and is responsible for producing torque in the motor;
- Homopolar stator current, which is a type of current that flows equally in all three phases of a three-phase system and in the same direction. It typically indicates fault conditions such as ground faults or unbalanced loads. Ideally, it should be zero.

The following table lists the parameters configured in this block, as indicated by the constructor of the motor:

Parameter	**Values**
Number of pole pairs	5
Maximum phase current RMS magnitude	25 Arms
Permanent magnet flux linkage at reference temperature (20 °C)	0.408 Wb
Stator winding resistance at reference temperature (20 °C)	0.337 Ohm
Stator cyclic inductance on q axis	0.0158 H
Stator cyclic inductance on d axis	0.0125 H

Table 5.3: Torque controller parameter.

5.3.3 Current controller

This block serves as a current controller in the rotor direct-quadrature-zero reference frame for PMSM [16]. The block implements linear submodels with constant parameters as specified by the e-motor's developer.

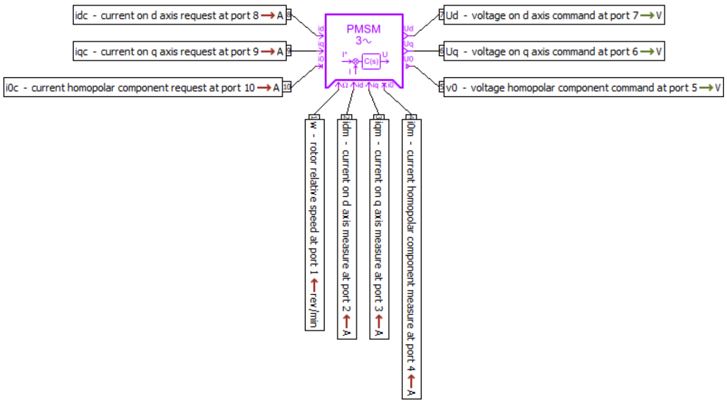

Figure 5.6: Current controller block.

As it can be observed in Figure 5.6 the block compares the currents in the dq0 reference frame coming from the left (reference values, depending on the torque request) and the bottom (effective values) and computes as output the voltage command values, again in dq0 reference frame, for the PWM based current controller.

Parameter	**Values**
Number of pole pairs	5
Permanent magnet flux linkage at reference temperature (20 °C)	0.408 Wb
Stator winding resistance at reference temperature (20 °C)	0.337 Ohm
Stator cyclic inductance on q axis	0.0158 H
Stator cyclic inductance on d axis	0.0125 H
Closed loop constant for d axis	0.001 s
Closed loop constant for q axis	0.001 s

Table 5.4: Current controller parameter.

The controller operates as a first-order closed-loop transfer function, so the behavior of the controlled machine currents will be that of a first-order transfer function [20]. The direct and quadrature currents are processed separately with two different close-loop time constants. A smaller value of those parameters gives a faster response.

5.3.4 Carrier-Based PWM controller

This block serves as a Carrier-Based PWM signal generator for switched inverter arms. It computes the switching signals for the inverter transistors according to the chosen modulation method. It also provides the value of the maximum line-to-neutral voltage RMS for the Torque controller block. Since it does not account for dead time, which is the delay in the opening and closing of the inverter transistor due to inertia and non-linearities, blocks have been added to the output branches which introduce those blanking times, in order to account for the resulting energy losses and dynamic consequences.

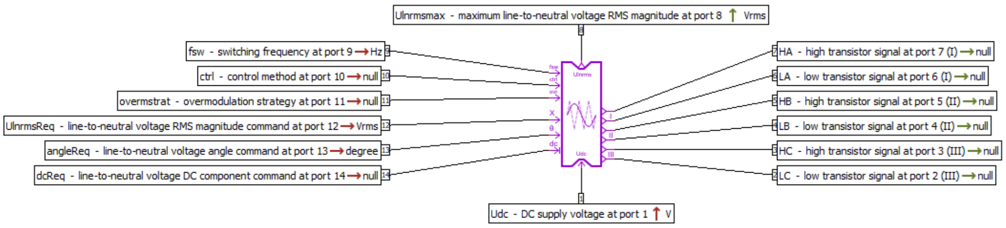

Figure 5.7: PWM controller block.

The inputs of this block are:

- The voltage command values coming from the Current controller. They are in the polar reference frame, so beforehand an additional block is implemented, responsible for computing the Inverse Park Transformation [16] followed by a conversion from Cartesian coordinates (d,q) to polar coordinates (magnitude and phase angle);
- The switching frequency, which is a fundamental parameter in PWM methods and directly affects the frequency rates of transistor switching. It has a heavy impact on the dynamic behavior and sound quality of the electric machine [9];
- The control method, which regulates how the PWM switching command is computed. This also affects the dynamic behavior and sound quality of the electric machine, other than the efficiency [9];
- Overmodulation strategy, a technique used to increase the voltage output of an inverter beyond the linear modulation range. This strategy allows the inverter to produce a higher fundamental voltage at the expense of increased harmonic distortion;
- The voltage supply value.

Pulse Width Modulation is a technique used to control the amount of power delivered to an electrical device by varying the width (duty cycle) of the pulses in a pulse train. It requires a DC electrical supply and it powers AC devices such as the PMSM of the case study. PWM can be performed with different modulation strategies.

The PWM modulation strategy chosen for the simulation is the Space Vector modulation. This modulation strategy differs from the more traditional Sinusoidal Vector Modulation because of better voltage utilization and reduced harmonic distortion. This is obtained mainly by applying a different reference voltage signal. The reference voltage signals overlap with the carrier signal to determine when to switch on or off the transistors of the inverter arms. When the carrier signal crosses the reference signal, the transistors commute.

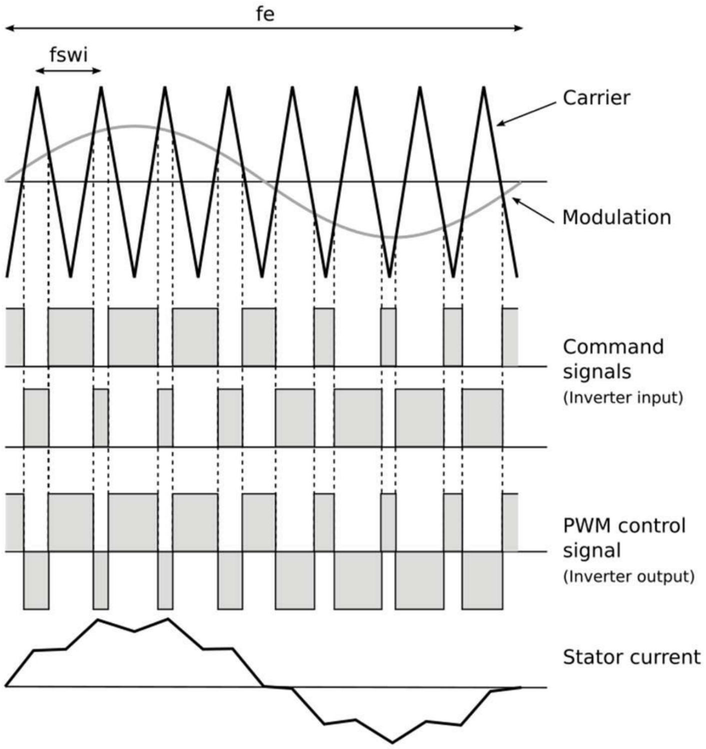

Figure 5.8: The PWM working principle.

In Figure 5.8 the reference voltage signal is labeled as "Modulation" while the carrier signal as "Carrier".

Figure 5.9 shows the reference voltages in Sinusoidal modulation. Since the 1D electric drive unit model computes the three-phase currents, the modulation is performed by implementing three reference voltages.

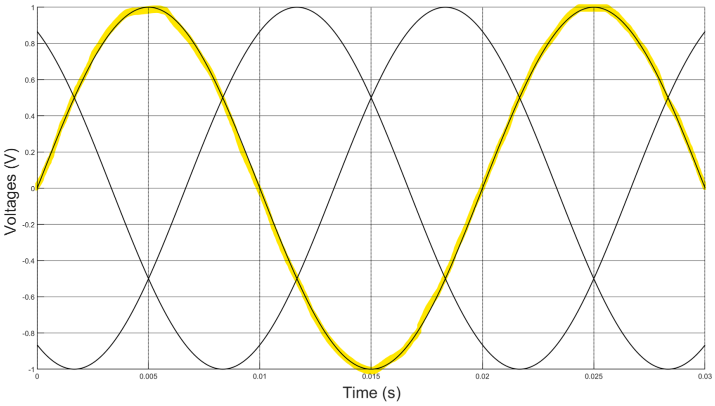

Figure 5.9: Sinusoidal modulation 3 phase reference voltages.

Figure 5.10 shows the reference voltages in Space Vector Modulation. To facilitate the observation of differences between the trends, one of the phase currents is highlighted in both figures.

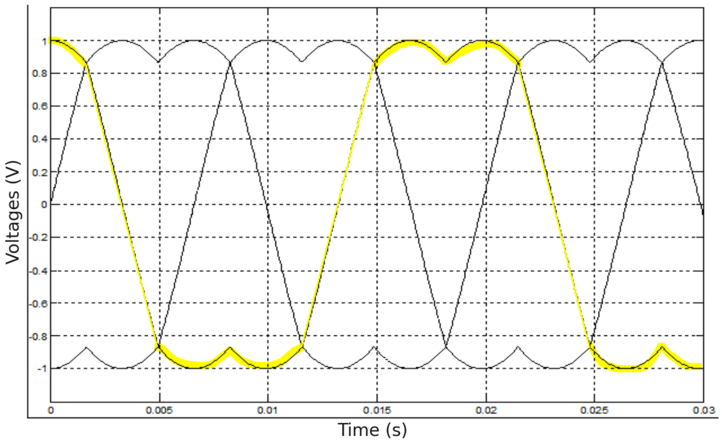

Figure 5.10: Space vector modulation 3 phase reference voltages.

The reference signals in Space Vector Modulation allow for better voltage utilization, as the difference in voltages is a crucial parameter for torque generation in the electric machine. At any given moment, the voltage difference between the three trends in Figure 5.10 is noticeably higher compared to those in Figure 5.9.

5.3.5 Electric machine

This block serves as the electric machine and it accounts for its electromagnetic characteristics. It's not anymore possible to describe the block inputs and outputs since the links with the surrounding blocks follow the bond-graph principle and, as shown in Figure 5.11, are in the form of energy exchange rather than signals. For example, on the right the information is passed through torque and rotational speed. The blocks exchanges also the currents and voltage information from the bottom and the temperature and heat power from the left.

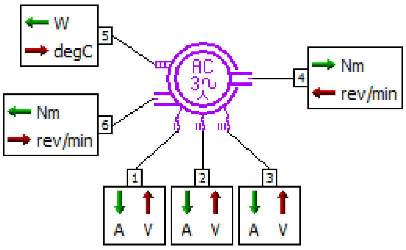

Figure 5.11: The electric machine block

This block has been the center of an in-depth analysis focusing on its submodel. Initially, the submodel was assumed to be linear, with constant physical parameters provided by the electric machine's developer. The table below lists the values used in this initial analysis, which are also applied in the torque and current controllers.

Parameter	**Values**
Number of pole pairs	5
Reference Temperature	20 °C
Permanent magnet flux linkage at reference temperature (20 °C)	0.408 Wb
Stator winding resistance at reference temperature (20 °C)	0.337 Ohm
Stator cyclic inductance on q axis	0.0158 H
Stator cyclic inductance on d axis	0.0125 H

Table 5.5: Electrical machine parameters.

As detailed in Section 11.2, it was necessary to modify the submodel of the electric machine block. In the second approach, a non-linear, spatially-dependent submodel was implemented to more accurately represent the electromagnetic characteristics of the e-motor. This change ensures that the coupling of the currents and rotor angular position is consistent between the 2D electromagnetic model and the 1D electric drive unit model. Unlike the linear model, the flux linkage is decoupled between the direct and quadrature axes of the rotary reference frame and varies with the angular position. Another spatially dependent parameter is the torque, which also depends on the angular position.

The flux linkage on the q-axis, the flux linkage on the d-axis, and the torque characteristics were determined using a separate 2D electromagnetic model, which is not part of the FE simulation framework. As shown in Figure 5.12, since these characteristics span the entire circumference of the electric machine, this 2D model must be comprehensive and not just a partial section of the e-motor.

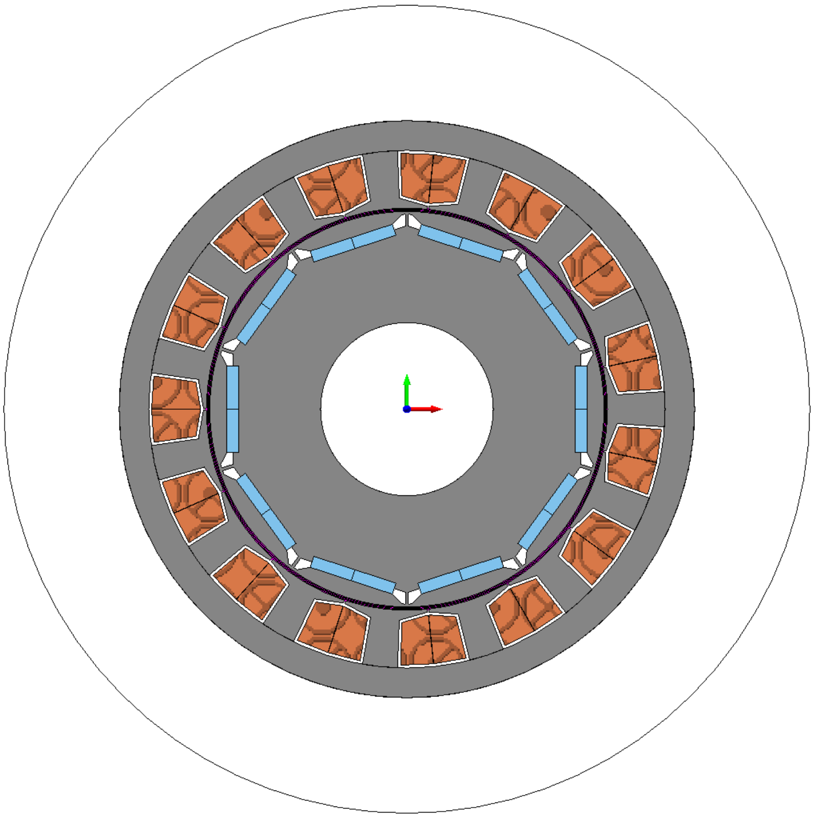

Figure 5.12: The 2D complete EM model.

5.3.6 Rotary load

This block serves as the mechanical rotary load in the form of mechanical inertia and viscous friction, which are set to model the accurate working conditions of the electric machine. Another mechanical load is introduced as constant opposite torque to the rotational speed, implementing the constant parameter block K at the end of the branch placed on the right. The surrounding blocks are sensors of the angular position and rotational speed, necessary for the closed control loops. The links are in the form of energy, following the bond-graph theory.

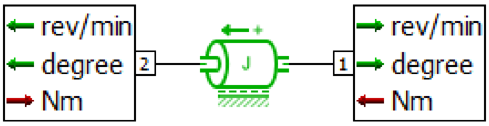

Figure 5.13: The rotary load block.

The parameters set in this block are the mechanical inertia and the viscous friction, given by the electric motor's developer and listed in the following table:

Parameter	**Values**
Mechanical inertia	$0.03898\ \mathrm{Kg \cdot m^2}$
Viscous friction	$\frac{\mathrm{Nm}}{\mathrm{rad/s}}$

Table 5.6: Rotary load.

5.4 Operating conditions

The simulation is set up in transient operating conditions which consist of an initial condition where the e-motor is stationary and the reference speed is 0 RPM. After 1 decimal of a second, the reference speed is set to start increasing until it gets to the setup reference final speed, which will, in the end, be the desired rotational speed of the simulation. The reference speed gets to its final value following an order-3-polynomial trend which lasts 0.2 s, as shown in Figure 5.14, where the final value has been set as an example at 500 RPM.

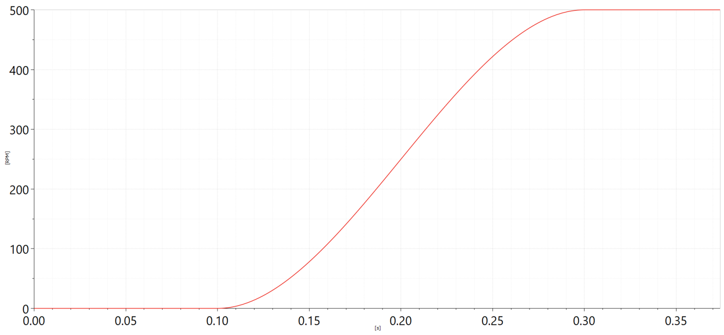

Figure 5.14: Rotational speed reference value.

Since the model's initial condition is stationary, any change in the reference rotational speed immediately creates a discrepancy between the reference and actual speeds. This difference triggers the rotational speed control loop, initiating the e-motor. The control loop has been finely tuned to ensure that the electrical machine reaches steady-state conditions as quickly as possible.

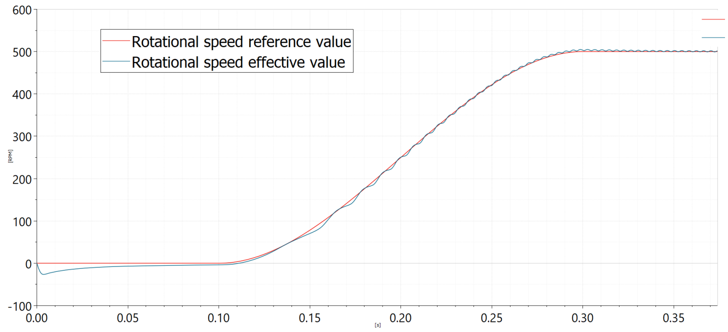

Figure 5.15: Comparison between reference and effective values of the rotational speed.

In Figure 5.15, it can be observed the comparison between the reference and effective rotational speed values during the simulation. The slight oscillations around the reference value are due to the non-linearities implemented in the electric machine submodel (subsection 5.3.5), which affect the rotational speed.

The simulation lasts for 2.5 seconds, a duration long enough to provide a substantial dataset for subsequent 2D electromagnetic simulations, yet short enough to maintain reasonable computational time. Steady-state conditions are reached at approximately 0.4 seconds for a rotational speed of 500 RPM, whereas at higher speeds, such as 1500 RPM, steady-state is achieved at around 0.5 seconds. The sampling frequency is set at 25,000 Hz, which is necessary for this simulation since the frequency of interest extends up to 12,500 Hz.

Each run of the simulation lasts approximately 10 seconds, corresponding to a specific rotational speed. The operating conditions of interest cover rotational speeds ranging from 500 RPM to 1500 RPM, with increments of 25 RPM. The PWM modulation method used is Space Vector Modulation, with a carrier frequency of 5000 Hz. The opposing torque load applied to the electric motor is 55 Nm.

The parameters set for this simulation are listed in the following table:

Parameter	**Values**
Simulation duration	2.5 s
Sampling frequency	25000 Hz
Reference rotational speed	500:100:1500 RPM
PWM modulation method	Space vector
Carrier frequency	5000 Hz
Opposing torque load	55 Nm
Run time	~10 s

Table 5.7: Simulation's operating condition parameters.

6. The 2D FE Electromagnetic model

The 2D FE Electromagnetic model is designed to estimate the magnetic forces in the air gap, which cause magnetic noise in the electric machine by acting on the inner surface of the stator as a dynamic excitation. The simulation inputs are the three-phase currents flowing in the stator coil, coupled with the rotor's angular position. Both of them are results of the 1D electric drive unit model.

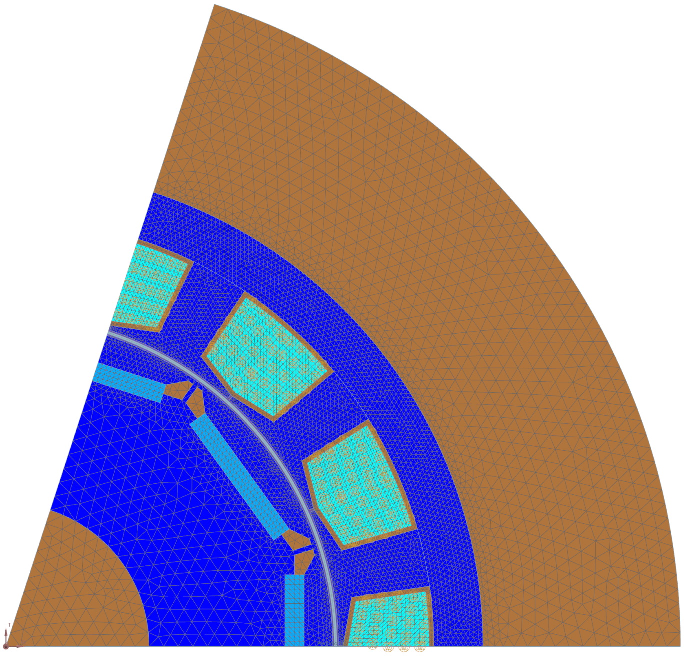

Figure 6.1: The 2D FE electromagnetic model.

Traditionally, simulation frameworks comprehend complete-section electric motor models as the 2D electromagnetic model. However, for this project, a partial model consisting of only an angular sector has been developed. Specifically, this angular sector represents 1/5th of the motor's complete section. This partial modeling approach significantly reduces computational time and result size.

6.1 Simcenter 3D Magnet

The software used to perform the 2D FE electromagnetic simulation is Simcenter 3D. Simcenter 3D is a comprehensive, fully-integrated computer-aided engineering (CAE) solution developed by Siemens PLM Software. It is designed to address complex engineering challenges by enhancing simulation efficiency across multiple physics domains. Simcenter 3D combines finite element analysis (FEA), computational fluid dynamics (CFD), and other simulation techniques into a single platform. Its range of applications are structural analysis, thermal analysis, motion simulation, and electromagnetics [21].

In particular, to perform the case study's EM simulation it has been used Simcenter 3D's EM solver Magnet. The Simcenter 3D Magnet solver is a specialized tool within the Simcenter 3D suite designed for electromagnetic field simulations. This solver is capable of accurately predicting the performance of electromagnetic devices such as motors, like the case study PMSM, generators, transformers, and sensors. It uses advanced numerical techniques to solve Maxwell's equations, enabling detailed analysis of magnetic fields, electric fields, and associated phenomena like eddy currents and magnetic hysteresis [21].

6.2 Finite Element Method

Finite Element Method (FEM) is a powerful computational technique used for solving complex physical problems in engineering and science. The method involves discretizing a large system into smaller, simpler parts called finite elements, where equations can be approximately solved. These elements are connected at discrete points known as nodes, forming a mesh that covers the entire domain of the problem. This technique is particularly effective for problems involving complex geometries, material properties, and boundary conditions. The FEM relies on the principle of virtual work, where the functional integral of the system's energy is minimized. By applying this principle, the system of equations governing the physical behavior of each finite element can be derived. These equations are then assembled into a larger system that approximates the behavior of the entire model. By breaking down a problem into finite elements and using numerical methods to solve the resulting system of equations, FEM provides accurate and reliable solutions to various physical phenomena such as stress analysis, heat transfer, fluid dynamics, and electromagnetic fields [22].

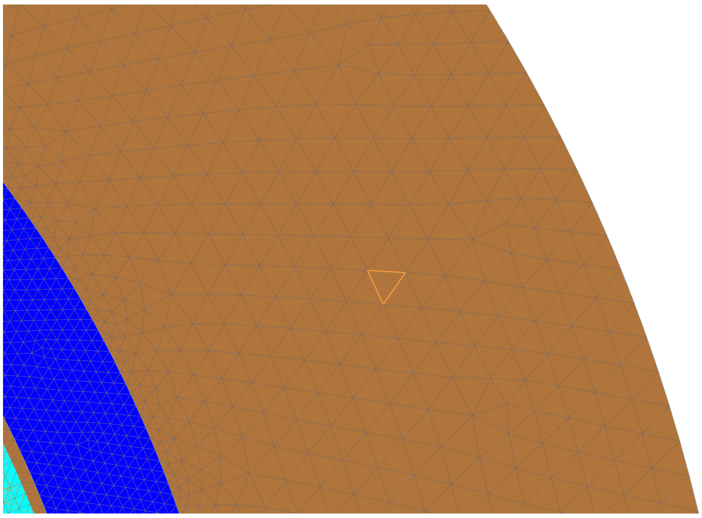

Figure 6.2: A finite element in the model.

In 2D electromagnetic applications, FEM is useful for analyzing and designing electromagnetic fields and devices. By discretizing the 2D space into finite elements, FEM enables the detailed study of devices such as antennas, sensors, and, as in our case, electric machines. This method allows for precise modeling of complex boundary conditions and material interfaces, making it an essential tool for advanced electromagnetic applications [23].

6.3 Maxwell tensor

The EM surface force density computation methods are based on the Maxwell stress concept, which directly gives the stress, or force per unit area, in terms of the magnetic flux density [24]. These forces arise due to the interaction between the magnetic fields and the structural components of the machine, leading to torque production and potential vibrations.

The Maxwell stress tensor, $\mathbf{T}$, represents the electromagnetic forces within a continuous medium. For an electric field $\mathbf{E}$ and a magnetic field $\mathbf{B}$, the Maxwell stress tensor is defined as [25]:

$$\mathbf{T} = \epsilon_0 \left(\mathbf{E} \otimes \mathbf{E} - \frac{1}{2} E^2 \mathbf{I} \right) + \frac{1}{\mu_0} \left(\mathbf{B} \otimes \mathbf{B} - \frac{1}{2} B^2 \mathbf{I} \right) \tag{6.1}$$

where:

- ϵ_0 is the permittivity of free space,
- μ_0 is the permeability of free space,
- $\mathbf{E} \otimes \mathbf{E}$ denotes the vector product of the electric field,
- $E^2 = \mathbf{E} \cdot \mathbf{E}$ is the magnitude squared of the electric field,
- $\mathbf{B} \otimes \mathbf{B}$ denotes the vector product of the magnetic field,
- $B^2 = \mathbf{B} \cdot \mathbf{B}$ is the magnitude squared of the magnetic field,
- $\mathbf{I}$ is the identity matrix.

Since in the air gap, where the EM force is evaluated, there is no electric field, the equation can be simplified and its component version is:

$$\mathbf{T}_{ij} = \frac{1}{\mu_0} \left(B_i B_j - \frac{1}{2} \delta_{ij} B^2 \right) \tag{6.2}$$

where:

- μ_0 is the permeability of free space,
- B_i and B_j are the components of the magnetic field,
- δ_{ij} is the Kronecker delta,

Since the domain of interest is the interface between the stator tooth and the air gap we can name the stress components in the equation as normal σ_n and tangential σ_t to the surface, so then the equations become:

$$\sigma_n = \frac{B_n^2 - B_t^2}{2\mu_0} \tag{6.3}$$

$$\sigma_t = \frac{B_n B_t}{\mu_0} \tag{6.4}$$

The results of the 2D EM model's simulation is the surface nodal density obtained from the numerical integration of the force densities σ_n and σ_t over the Finite Elements. As described in Chapter 3, the normal component of the electromagnetic field is the primary contributor to acoustic noise [12]. However, the Simcenter 3D Magnet solver also accounts for the tangential component without increasing computational time. Therefore, in the FE framework, the surface nodal force density includes contributions from both the normal and tangential components.

6.4 Model setup and parameterization

The 2D EM model is a FEM partial model consisting of 1/5th of the complete section of the electric motor.

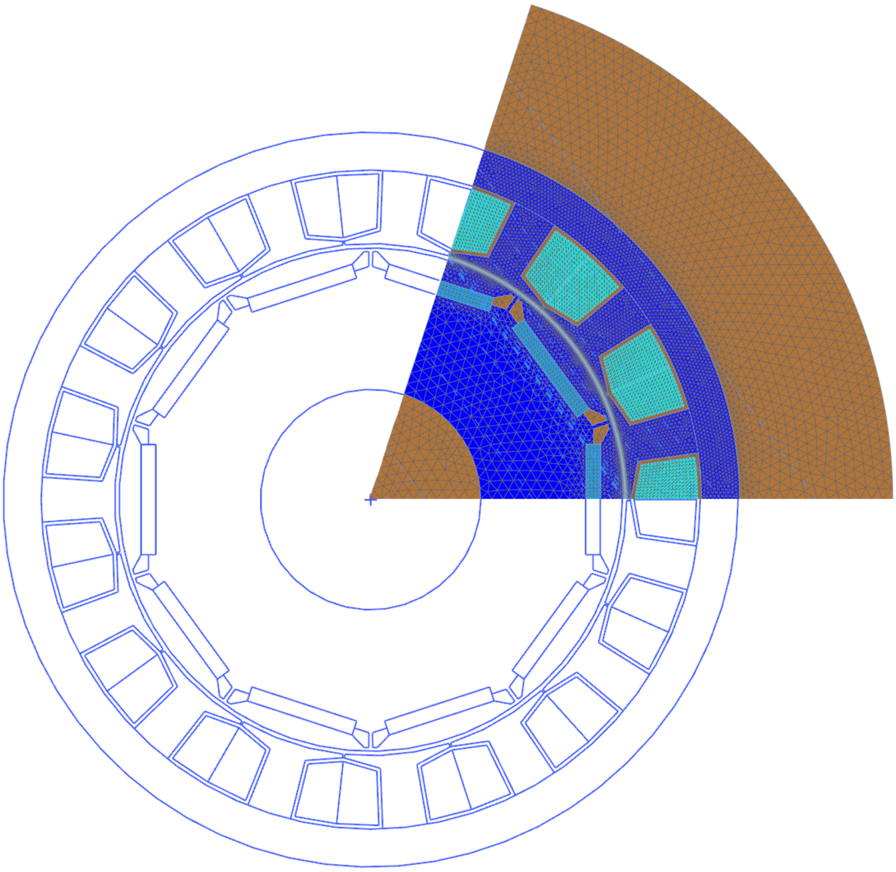

Figure 6.3: The partial model compared to the complete section of the e-motor.

6.4.1 Mesh collectors

The model is discretized into finite elements by organizing the meshes corresponding to different components of the e-motor into distinct mesh collectors. Each mesh collector is associated with specific materials, characterized by their unique electromagnetic properties. The following table lists all the mesh collectors associated with the materials and their respective colors, with labels referring to Figure 6.4.

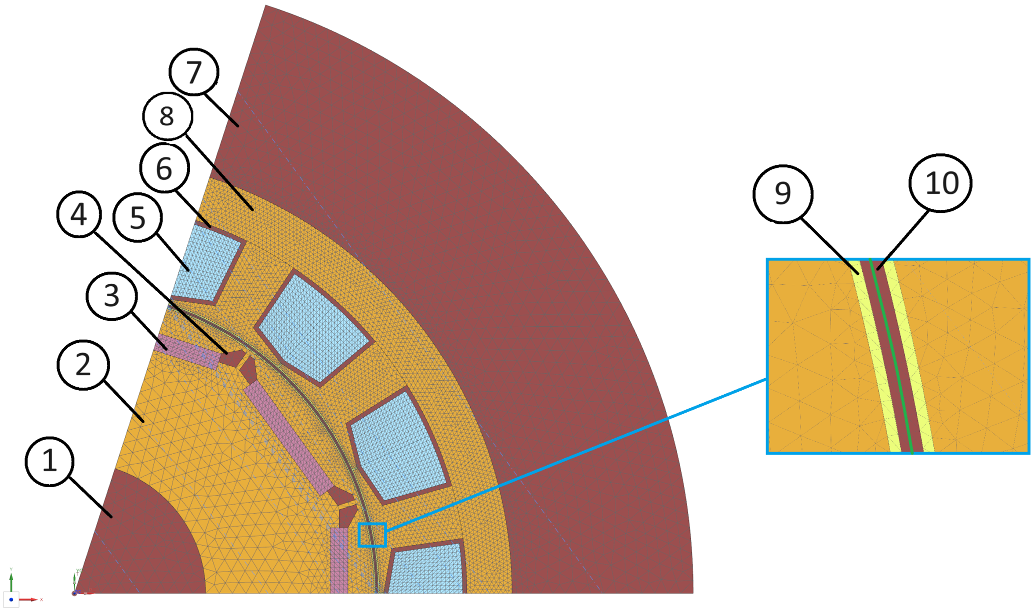

Figure 6.4: The model's mesh collectors.

Label	Mesh Collectors	Material	Color
1	Rotor air Air	Air	Brown
2	Stator Core	Electric steel M270-35A	Ochre yellow
3	Permanent magnet	Neodymium magnet N40SH	Pink
4	Rotor Air	Air	Brown
5	Stator coil	Copper	Light blue
6	Stator air	Air	Brown
7	Stator air	Air	Brown
8	Virtual air	Virtual air	Light yellow
9	Remesh region	Air	Brown

Table 6.1: Mesh Collectors, Materials, and colors referring to Figure 6.4

.

The Remesh region is a designated mesh collector that undergoes refinement or modification during the simulation process. The remeshing is essential to accommodate the relative movement of components during the simulation. In the model, the Remesh region is positioned at the boundary between the stator and the rotating rotor, as highlighted in Figure 6.4. This allows for accurate simulation of the interactions and dynamic behavior at the interface of these moving parts [26].

The Virtual air material is used as a medium in critical areas of the model, for example near the Remesh region, accurately simulating the propagation and distribution of electromagnetic fields [26]. The different mesh collectors are characterized by elements with sizes varying from 5 to 10 mm.

6.4.2 Magnets orientation

The internal magnets are oriented according to the e-motor design as shown in picture Figure 6.5. The orientation is set up in the simulation model through a tool that orients the magnetic properties of the material of the mesh collector "Permanent magnet".

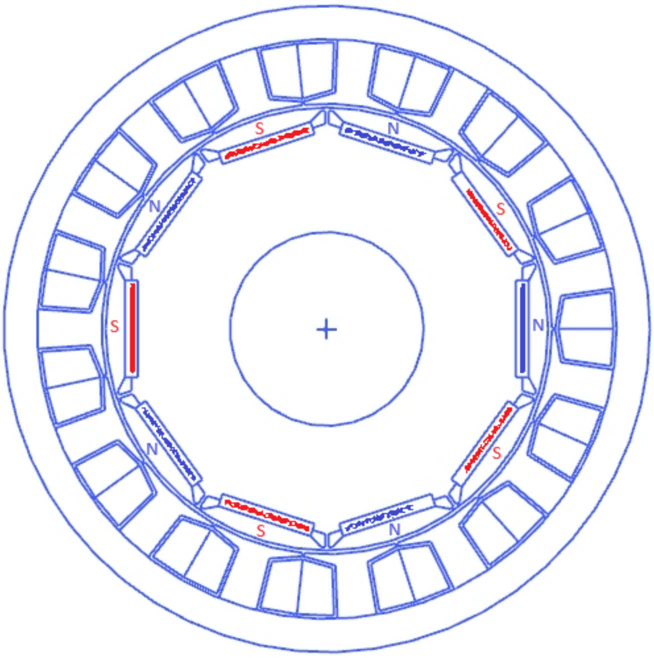

Figure 6.5: The permanent magnets arrangment

6.4.3 Coil arrangement

The coils are incorporated into the model as entities intersecting the cross-section of the e-motor. The properties associated with the coils, such as wire size and coil arrangement, are configured according to the e-motor design specifications.

As can be deduced from Figure 6.6, the coil arrangement follows a A-A, B-B, C-C pattern, going counterclockwise. The properties of the coils are listed in the following table:

Parameter	**Value**
Number of turns per coil	66
Wire section	1.56 mm^2

Table 6.2: Parameter and Value Table

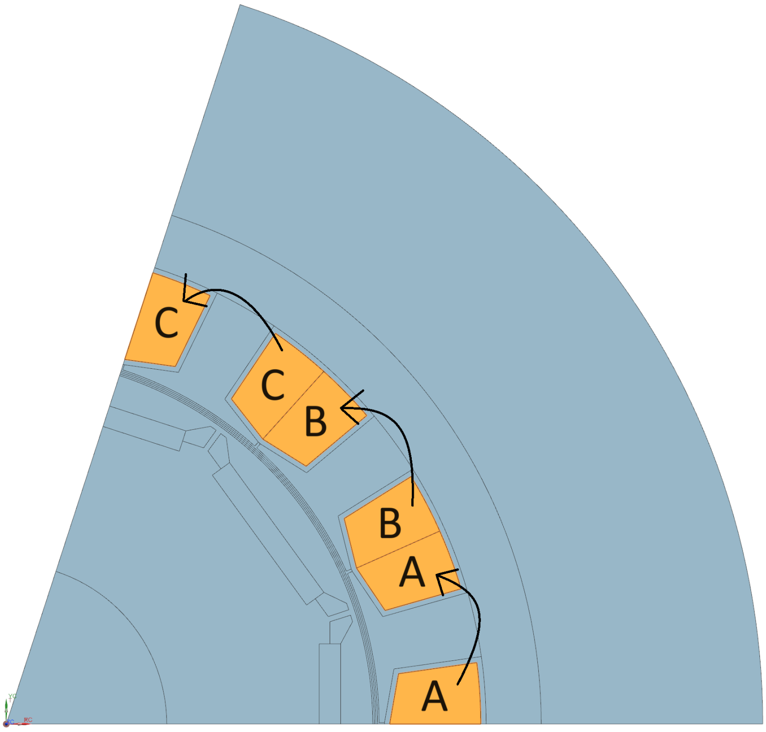

Figure 6.6: Coil arrangement.

6.4.4 Boundary conditions

The 2D EM model represents a sector of the complete section of the electric motor. Given that the motor's section exhibits exact periodicity within a 1/5th sector, this 2D model is sufficient to accurately simulate the electromagnetic behavior of the entire electric machine. To accomplish that, periodic boundaries need to be implemented. By applying periodic boundary conditions, the model ensures that the physical properties and behaviors at the boundaries of the sector align seamlessly with adjacent sectors, replicating the continuity and symmetry of the full motor. This technique significantly reduces computational requirements while maintaining accuracy in simulating electromagnetic fields and other physical properties.

The meshes must be set up so that the radial position of the nodes on the opposite edges match perfectly, as highlighted in blue and green in Figure 6.7. The nodes must align precisely to ensure that the simulation properties transfer accurately from one boundary to the opposite during the simulation.

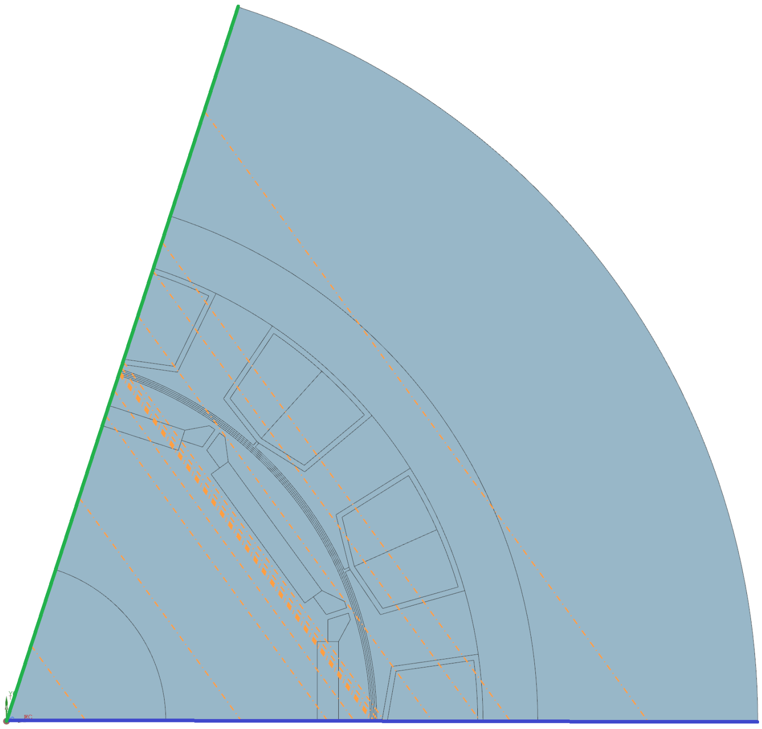

Figure 6.7: Periodic boundaries. The dotted lines are a representation of the node match between the 2 opposite edges.

6.5 Operating conditions

The simulation is conducted in the time domain under steady-state conditions with a constant rotational speed. Inputs from the 1D electric drive unit model include the rotor angular position and the three-phase currents as functions of time. The simulation outputs are the nodal force densities, computed in time domain. Both the inputs and the outputs of the simulation refer to specific time steps, which have been set up depending on the rotational speed of the e-motor.

The solution domain is limited to the stator core's edges, as highlighted in orange in Figure 6.8, but the subsequent 3D vibroacoustic simulation only uses as inputs an even more limited range of data: only the electromagnetic forces applied to the inner surface of the stator (highlighted in green) are considered as dynamic excitation for the vibroacoustic response.

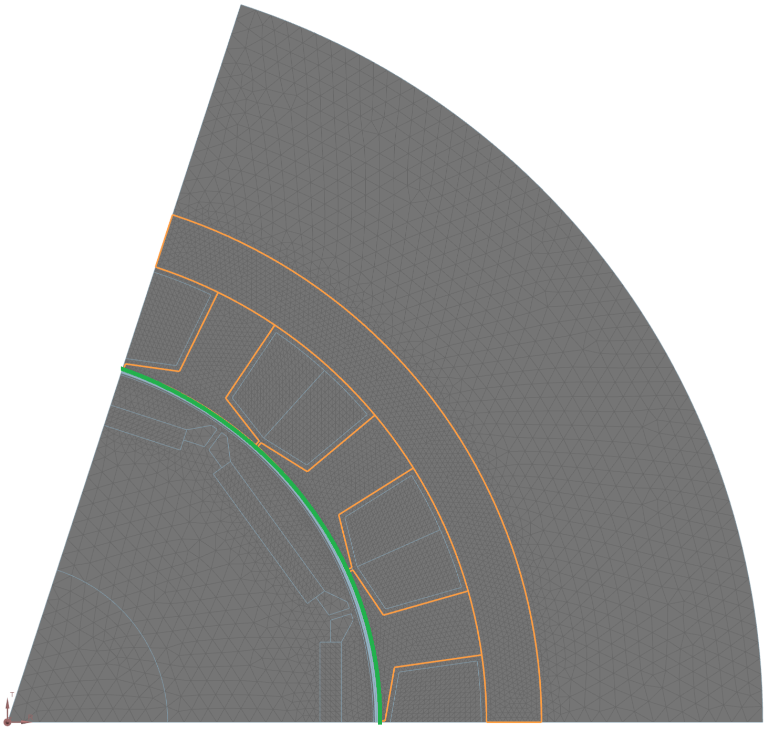

Figure 6.8: The EM simulation's solution domain.

In the first approach, the simulation run time covered only one electrical cycle, which conveniently corresponded to 1/5th of a complete revolution, exactly the size of the model's angular sector. The simulation started with the initial position of the rotor as shown in Figure 6.9 and ended as shown in Figure 6.10.

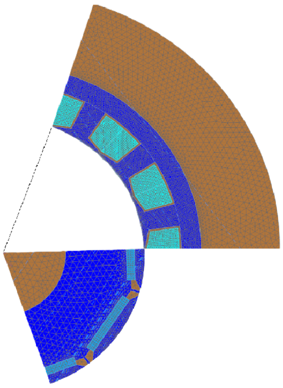

Figure 6.9: Simulation initial position.

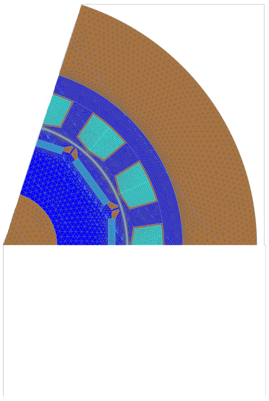

Figure 6.10: Simulation final position.

However, to improve the accuracy of the results, it was necessary to extend the simulation run time to cover a full revolution. The following images show the second approach, with the partial model rotor going beyond the first electric cycle during the simulation. The change of approach is detailed in Section 11.4.

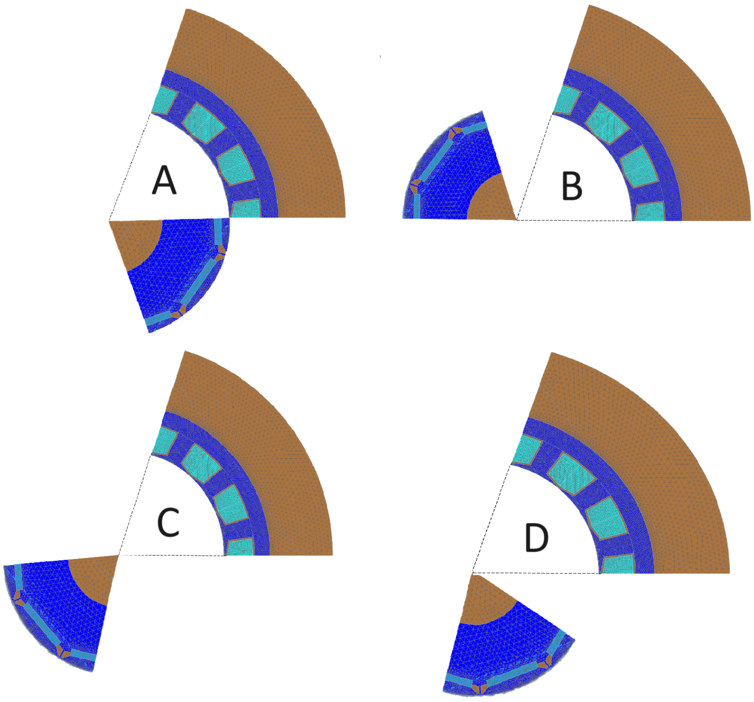

Figure 6.11: Different moments in the second approach's EM simulation, in order A, B, C, D.

Another difference between the first and second approaches lies in the setup of the time steps. In the first approach, the time step size is constant, whereas in the second approach, it varies. The time step setup is explained in detail in Section 11.4. The following table shows a series of examples of the time step size used in the first approach, so constant and in a simulation that lasts 1 electric cycle, for different rotational speeds. It can be observed that the size of the time steps has been changed in order to maintain the number of time steps as constant as possible.

Rotational speed	**Time step size**	**Number of time steps**
500 RPM	3.33 10^{-2} ms	720
650 RPM	3.84 10^{-2} ms	624
800 RPM	3.12 10^{-2} ms	768
1100 RPM	3.03 10^{-2} ms	792
1500 RPM	2.77 10^{-2} ms	864

Table 6.3: Simulation time step setup

6.6 Computational time

The comparison of computational time between the complete model and the partial model demonstrates that the partial model is significantly more efficient. This efficiency is due to the substantially lower number of nodes and elements in the FEM model, which reduces the computational load. The data presented in the following table refers to the simulation conducted at a rotational speed of 1000 RPM, revealing a 55% reduction in computational time.

Model	Computational Time
Complete	11 min and 32 sec
Partial	5 min and 10 sec

Table 6.4: Comparison in the model computational time

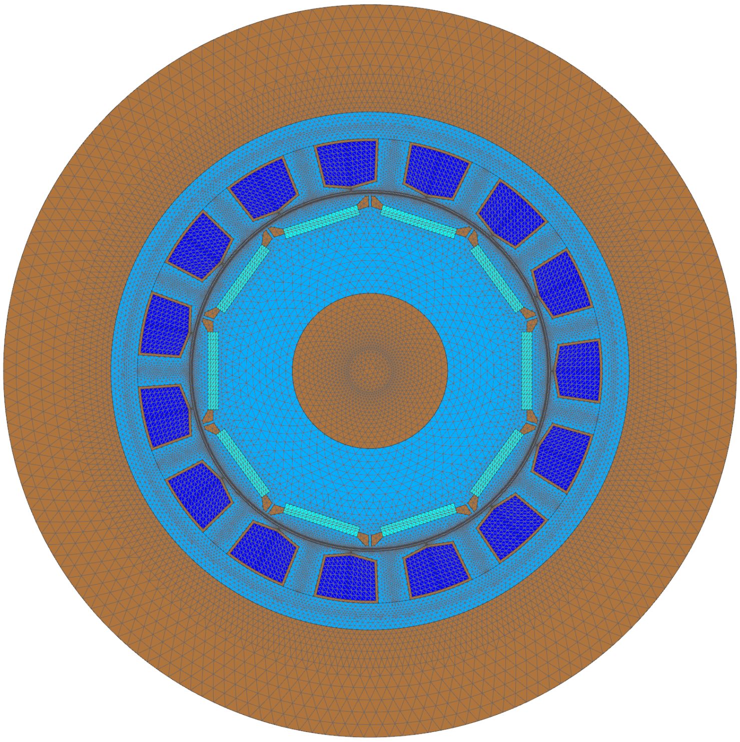

Figure 6.12: The 2D EM complete model.

The decreased computational time is achieved without compromising the accuracy of the results, as shown in Figure 6.12. The comparison between the complete and partial electromagnetic models is conducted at a rotational speed of 1000 RPM, using the same simulation parameters. The simulation covers six electric cycles, so it goes over a full revolution of the rotor. The input three-phase currents and rotor angular position are identical for both models. The plot illustrates the nodal force on a characteristic node, extracted as described in Section 11.3.

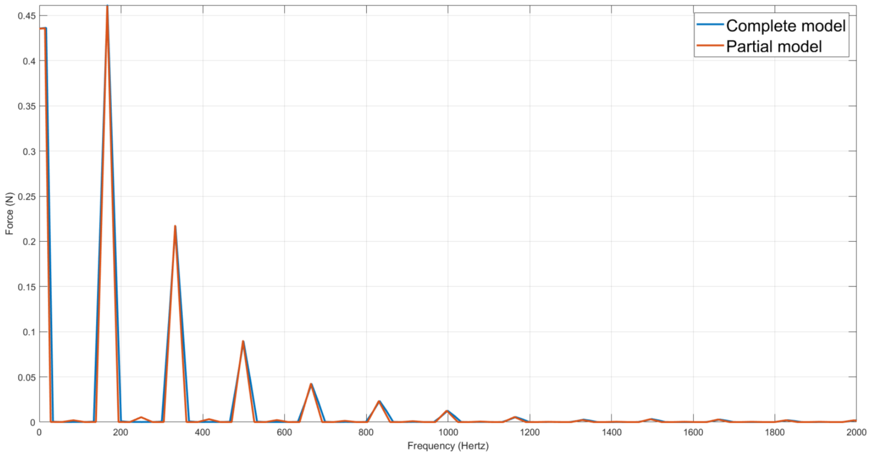

Figure 6.13: Comparison between the complete and partial model results.

7. The 3D structural model

The 3D structural model computes the mode shapes of the electric motor's stator through a procedure known as modal analysis. The mode shapes provide a condensed description of the dynamic characteristics of a structure, detailing the specific deformation patterns it undergoes when vibrating at its natural frequencies. These shapes are unique to each natural frequency and are determined by the structure's geometry, boundary conditions, and material properties.

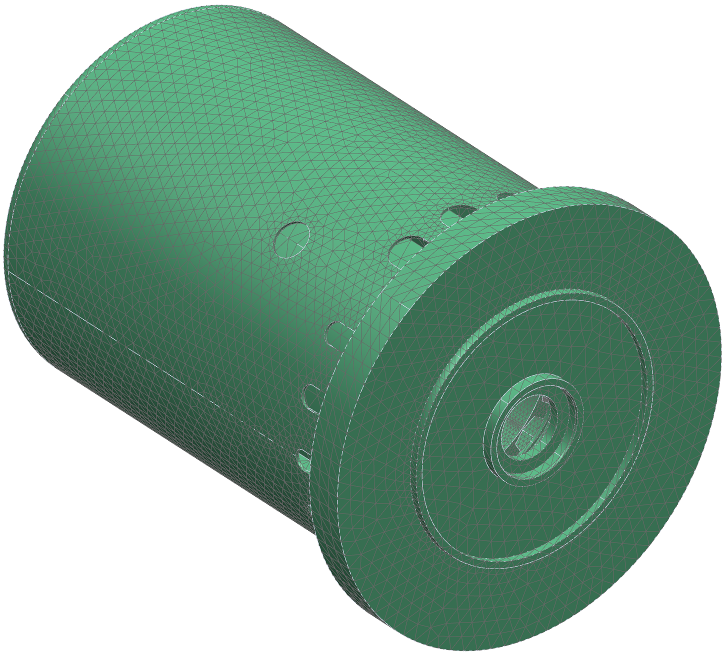

Figure 7.1: the 3D structural model.

The software used to perform the 3D finite element structural simulation is once again Simcenter 3D. However, differently from the previous analysis, Simcenter 3D's structural solver Nastran was utilized.

7.1 Simcenter 3D Nastran

Simcenter 3D Nastran is a structural analysis solver integrated within the Simcenter 3D simulation suite, developed by Siemens Digital Industries Software. It is widely recognized for its robust FEA capabilities, providing the tools necessary to perform comprehensive structural assessments, including linear and nonlinear stress analysis, dynamic response analysis, and advanced modal analysis [27].

7.2 Modal analysis

Modal analysis is a critical procedure in structural dynamics and mechanical engineering, used to determine a structure's natural frequencies, mode shapes, and damping characteristics. This analysis is accomplished by solving the eigenvalue problem associated with the system's mass and stiffness matrices, revealing the characteristic vibration patterns and their corresponding frequencies [28]. By understanding these mode shapes, engineers can predict how structures will respond to various dynamic loads, ensuring stability and performance.

In the case study, the modal analysis is conducted over a frequency range from 1 Hz to 25,000 Hz. The latter value is precisely double the maximum frequency of the analysis, in accordance with the Nyquist theorem [29].

7.3 Model setup and parametrization

The structural model consists solely of the stator of the electric motor. The rotor is not modeled for two different reasons:

- The primary source of acoustic noise in an electric motor is the EM excitation acting on the inner surface of the stator [12]. Specifically, the main causal chain of events leading to the acoustic pressure level at the microphone point outside the e-motor starts with the EM forces generated in the air gap. These forces propagate radially, causing vibrations in the stator structure. These vibrations then convert into sound waves that travel through the air surrounding the motor, moving outward toward the microphone point.
- Including revolving parts like the rotor in a frequency-domain simulation would be computationally intensive. The rotor, located internally, is not involved in the propagation of the EM-related vibrations.

Another approximation made in the design of the 3D model involves simplifying the lateral parts on the longitudinal ends of the electric motor. The holes on the left end of the motor shown in Figure 7.2 hide a fan with a bearing, which is keyed onto the rotor shaft for cooling purposes. These elements are not included in the structural simulation to simplify the model and reduce computational time.

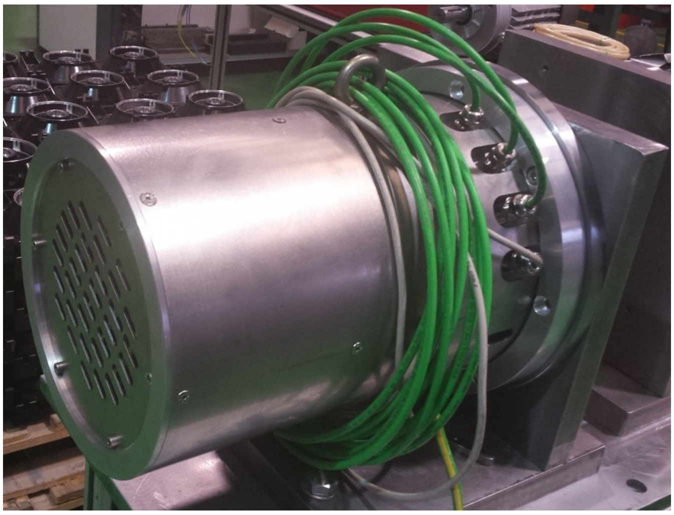

Figure 7.2: The assembled electric motor

7.4 3D Finite Elements

The simulation is performed solving the FE structural problem using the same discretization principles as described in Section 6.2, but using 3D elements. In particular, the discretization has been performed with CTETRA10 finite elements. CTETRA finite elements are a type of 3D tetrahedral element, specifically designed to model complex geometries with irregular shapes, such as the stator in case study. Simcenter 3D's meshing algorithm has two options, referring to the element's order:

- Linear (CTETRA4), which consists of four nodes, one at each vertex of the tetrahedron and is suitable for problems requiring less computational effort but can be less accurate for representing curved surfaces or varying stress gradients;
- Quadratic (CTETRA10), which consists of ten nodes, including four at the vertices and six along the edges, providing higher accuracy in capturing the behavior of curved surfaces and varying stress fields in the material [27]. They are particularly suitable for modeling objects with varying cross-sections, as in the case study.

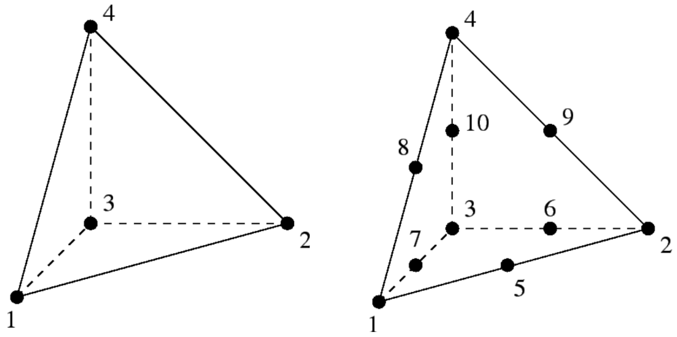

Figure 7.3: CTETRA4 (left) and CTETRA10 (right).

The size of the finite elements in the 3D structural model varies depending on the components of the assembly to minimize computational time without compromising the accuracy of the results. The maximum element size is 6 mm, assigned to the back and front covers, while the elements of the stator teeth are 3 mm in size.

7.5 Materials

The material varies depending on the different parts of the electric motor. The materials used are 3:

- M270-35A, a non-oriented electrical steel commonly used in the manufacturing of electric motors and transformers. This type of steel is specifically designed to optimize magnetic properties, such as high permeability and low core loss, making it ideal for applications where efficient magnetic performance is crucial [30].
- Aluminum 2014, a high-strength aluminum alloy known for its high strength-to-weight ratio, good machinability, and resistance to fatigue [31].
- AISI 304 stainless steel, a widely used austenitic stainless steel known for its excellent corrosion resistance, good mechanical properties, and ease of fabrication [32].

In the following page, the model is illustrated in Figure 7.4 with the different parts' labels referring to table 7.1.

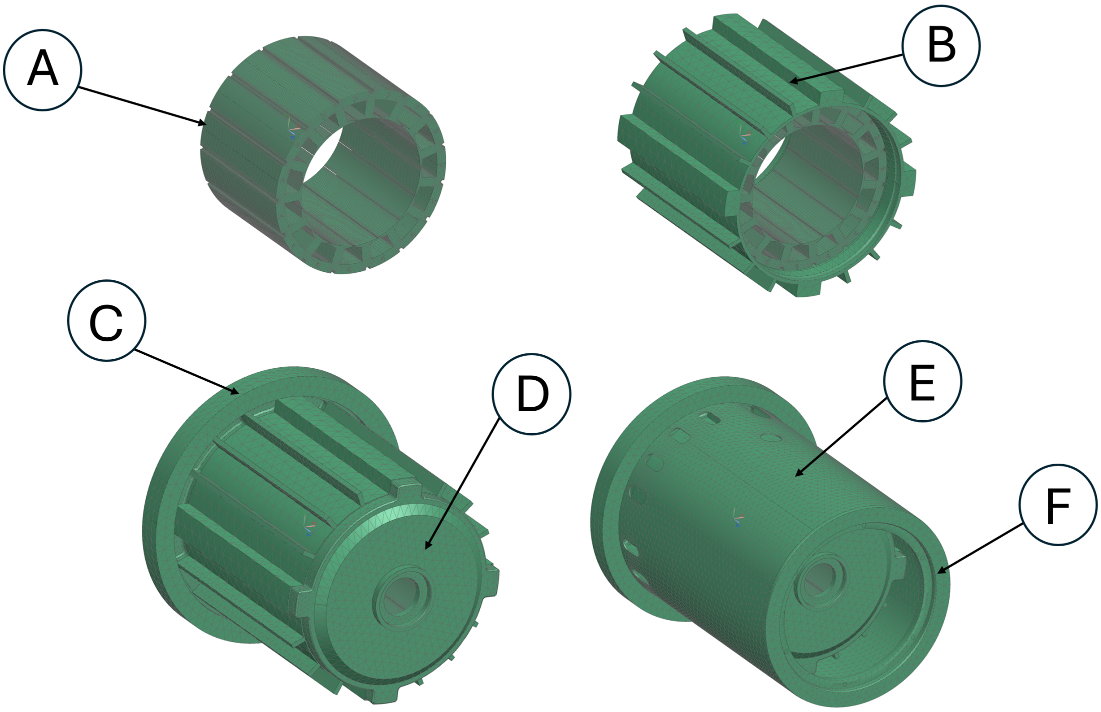

Figure 7.4: Stator parts.

Label	**Part name**	**Material**
A	Stator tooth	M270-35A
B	Finned cover	Aluminum 2014
C	Front cover	Aluminum 2014
D	Back cover	AISI 304
E	Radial cover	AISI 304
F	Backsealer	AISI 304

Table 7.1: Parts and materials

7.6 Constraints

The constraints incorporated in the model accurately reflect the real-world conditions of the electric machine during operation. As illustrated in Figure 7.2, the e-motor is constrained at one end, which is why the model includes a fixed constraint on that face.

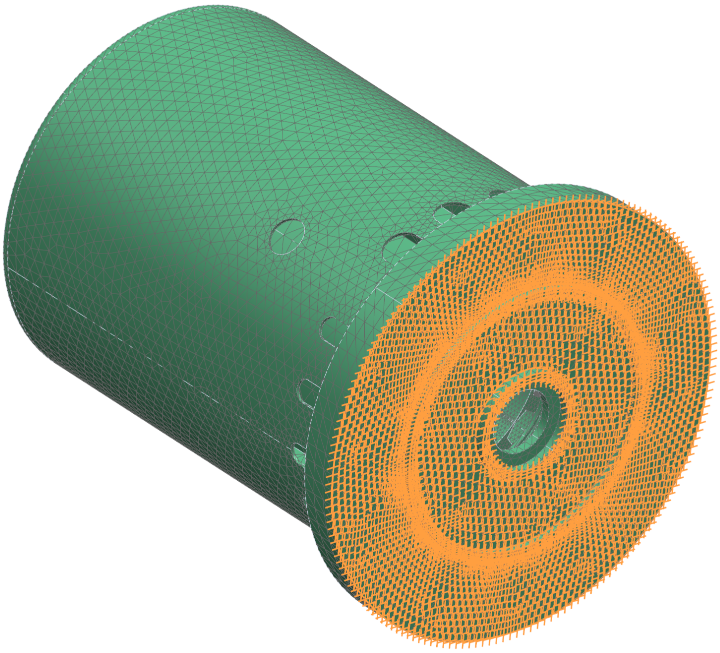

Figure 7.5: The fixed constraint, highlighted in orange.

The model is an assembly of all the parts listed in Table 7.1. The various elements are constrained to each other through a process referred to as "gluing" in the simulation environment of Simcenter 3D. This procedure involves selecting elements from adjacent parts and anchoring them together, effectively creating constraints between them. These constraints are applied to specific surfaces of the elements, and the size of these areas are adjusted to increase or decrease the stiffness of the structure. In Figure 7.6, the constrained zones of different "Stator tooth" parts are modeled to accurately represent the real-life constraints.

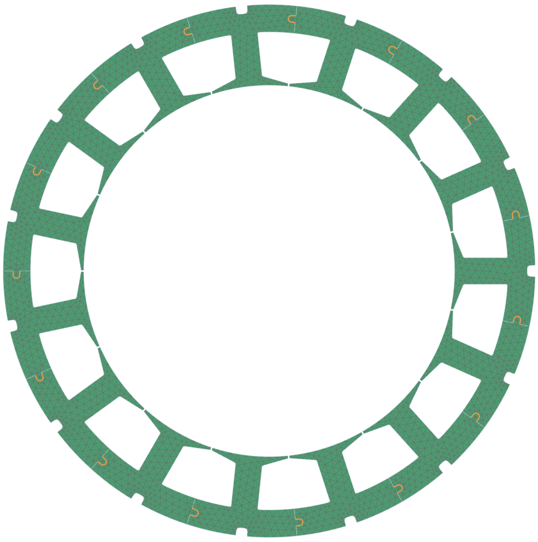

Figure 7.6: The glued elements area, highlighted in orange.

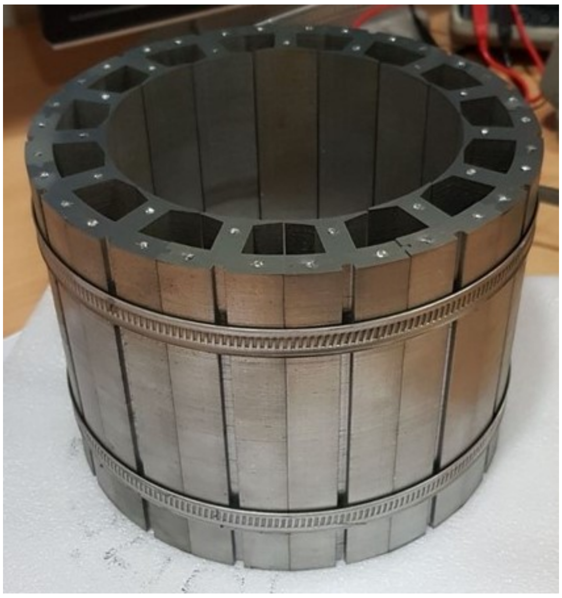

Figure 7.7: Disassembled stator teeth, held in position by the metal bands.

8. The 3D vibroacoustic model

The 3D vibroacoustic model couples the electromagnetic forces calculated by the 2D EM model with the mode shapes determined by the 3D structural model. This approach allows the simulation to know both the structural response of the e-motor stator and the dynamic excitation acting upon it. The resulting output is the acoustic pressure level at a specific point, referred to as the mic-point, which is positioned outside the stator.

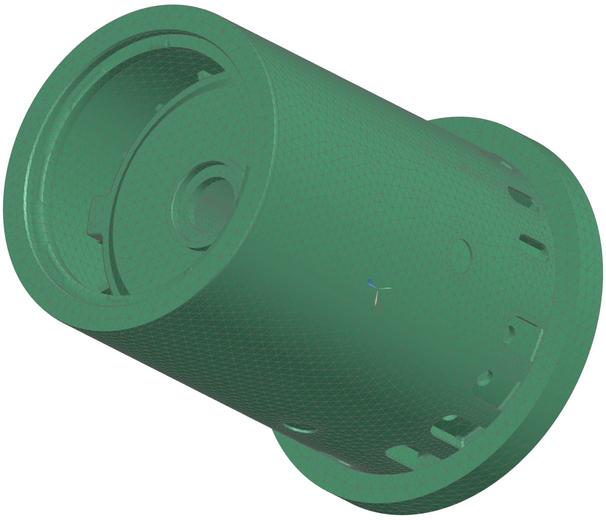

Figure 8.1: The 3D vibroacoustic model.

Figure 8.1 demonstrates that the model is essentially the same as the 3D structural model depicted in Figure 7.1. However, it serves primarily as a visual representation of the mode shapes used as inputs for the simulation, which are in fact the output of the 3D structural model. The dynamic excitation is provided by the EM forces, which are introduced as time-domain nodal force densities. In order to be utilized in this frequency-domain simulation, these forces must undergo a Fourier transform process. The model has been developed within the Simcenter 3D Vibroacoustic environment, utilizing Simcenter Nastran Vibroacoustic numerical solver.

8.1 Simcenter 3D Nastran Vibroacoustic

Simcenter 3D Nastran Vibroacoustic is an extension within the Simcenter 3D suite that focuses on the analysis of vibroacoustic phenomena. This tool integrates structural and acoustic simulations to predict how vibrations within a structure will generate sound and how this sound will propagate through different media. Utilizing the Nastran solver, it enables to perform comprehensive analyses, including the effects of dynamic excitations, modal coupling, and acoustic radiation [27]. Nastran Vibroacoustic enables the use of Acoustic Transfer Vectors (ATVs) to compute the acoustic pressure levels, significantly speeding up the simulation process and streamlining the analysis.

8.2 Acoustic Transfer Vectors

Acoustic Transfer Vectors are essential components in vibroacoustic analysis, facilitating the understanding of how structural vibrations translate into acoustic pressure at specific points in a surrounding fluid medium, such as air. By calculating the response of the acoustic field to unit excitations at various structural nodes, ATVs effectively create a mapping between structural vibrations and resulting sound pressure levels. Specifically, for the case study application, ATVs link the nodes on the surface of the stator structure to the acoustic pressure level at the mic-point. This approach significantly streamlines the analysis process, allowing for efficient and accurate prediction of acoustic behavior without repeatedly solving the full coupled structural-acoustic system.

ATV have been implemented in the 3D vibroacoustic model through a guided procedure [21], which consists of computing the vectors in a separate simulation and then introducing them in the model. Figure 8.2 illustrates the 3D FE model used for computing the transfer vectors. The model features a 3D acoustic mesh (shown in green) that is rendered transparent to reveal the stator's structure at its center.

The blue objects represent the Automatically Matched Layer (AML), a feature designed to enhance the accuracy and efficiency of vibroacoustic simulations. AML effectively simulates the infinite expanse of an acoustic domain by absorbing outgoing acoustic waves, thereby preventing reflections that can distort the results. By implementing AML, the mic-point can be placed outside the 3D vibroacoustic mesh, allowing the mesh to be smaller in volume and significantly reducing the computational load of the simulation.

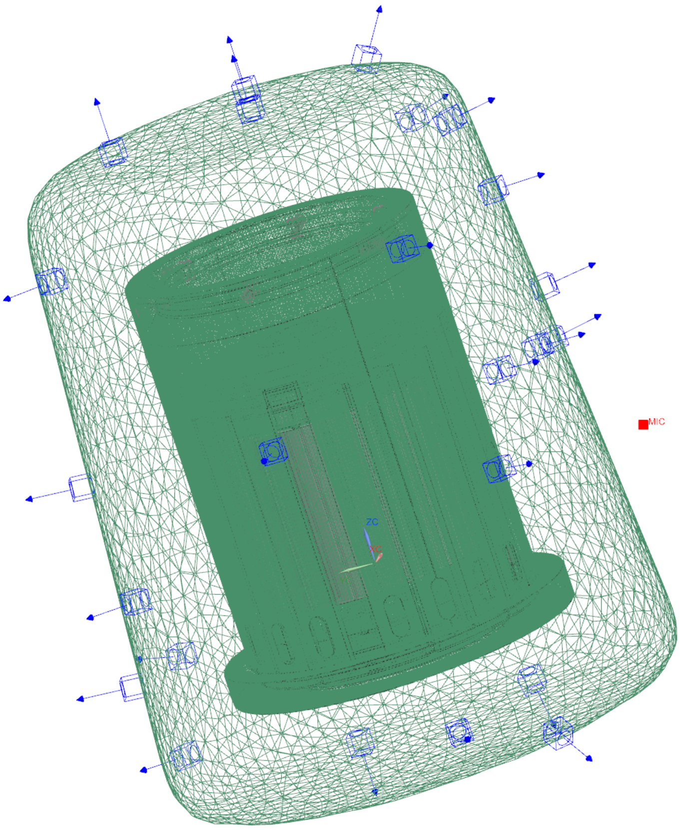

Figure 8.2: Model for ATVs computation.

8.3 Acoustic pressure level

Acoustic pressure level, also referred to as sound pressure level (SPL), is a measure of the pressure variation within a sound wave relative to the ambient atmospheric pressure. It quantifies the intensity of sound in a given environment and is expressed in decibels (dB). It's computed using the logarithmic ratio of the measured sound pressure to a reference pressure, typically 20 micropascals in air, which is the threshold of human hearing. This metric is crucial in various fields such as acoustics, audio engineering, and environmental noise assessment, as it helps in evaluating the loudness of sounds and their potential impact on human health and comfort.

The acoustic pressure level L_p is given by the formula:

$$L_p = 20 \log_{10} \left(\frac{p}{p_0} \right)$$

where:

- L_p is the sound pressure level in decibels (dB).
- p is the root mean square (RMS) sound pressure.
- p_0 is the reference sound pressure, typically $20\,\mu$Pa in air.

8.4 Model setup and parametrization

The ATVs frequency domain is set up according to the frequency range of interest of the vibroacoustic simulation. Since the frequency range of interest of the vibroacoustic simulation spans from 1 Hz to 12500 Hz, the ATVs have the same frequency domain.

Figure 8.2 shows the microphone point in red, positioned radially with respect to the e-motor cover at a distance of 250 mm from its center. Given that the stator case has a diameter of 250 mm, the mic point is located 125 mm radially from the e-motor cover. It is also positioned longitudinally at the center of the stator's teeth, at a distance of 130 mm from the constrained face (front cover).

8.5 Operating conditions

The simulation is conducted in the frequency domain, so the results from the 2D EM simulation are first subjected to a Fourier Transform. These transformed results are then mapped onto the inner surface of the stator, where they serve as the dynamic excitation for the simulation process. This process is described in detail in Section 11.3. The input data refer to a specific rotational speed of the electric motor, in steady-state conditions. Consequently, the results of the vibroacoustic simulation, expressed in terms of acoustic pressure levels, also refer to a steady-state rotational speed.

9. The 2D complete electromagnetic model

The 2D complete electromagnetic model computes the lumped EM forces that serve as inputs for the State Space model. This model is an extension of the partial EM one described in Chapter 6, comprehending the entire section. Due to the sectorial periodicity of the electric motor, the complete model is effectively a five-time circular replication of the partial one.

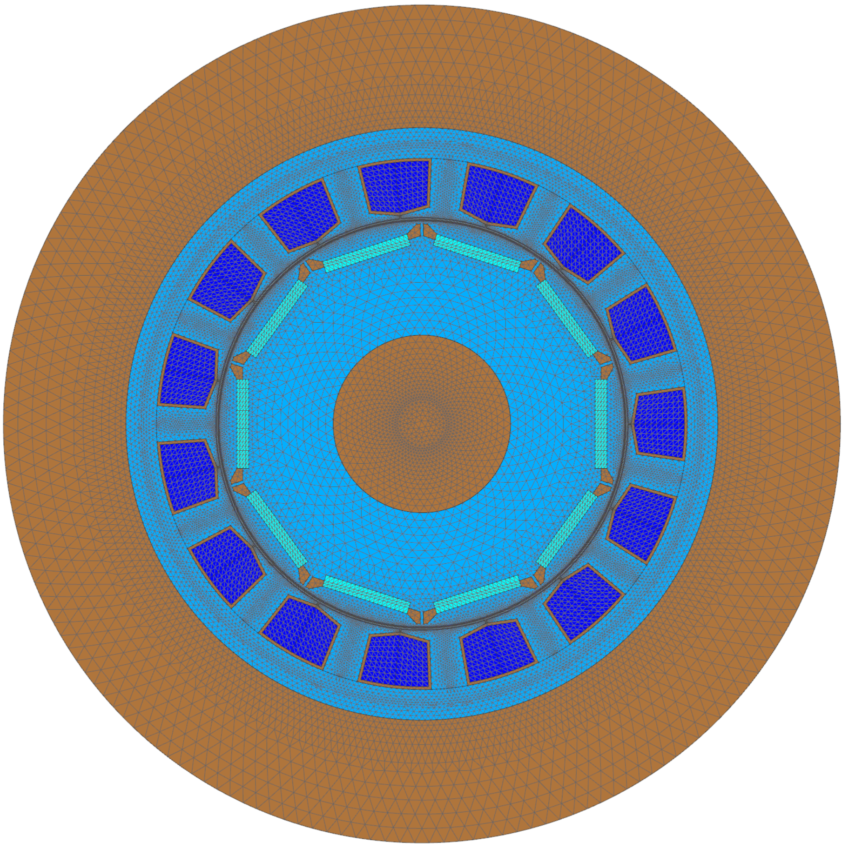

Figure 9.1: The complete EM model.

The simulation is conducted in the time domain under steady-state conditions with a constant rotational speed. Inputs from the 1D electric drive unit model include the rotor angular position and the three-phase currents as functions of time. Since the model is a 2D representation of a section of the motor, the lumped forces are computed by integrating along the perimeter of the teeth, as highlighted in Figure 9.2. The results are provided in the time domain and correspond to the time steps established in the simulation. The working conditions are identical to those in the FE simulation framework, allowing for a direct comparison between the results.

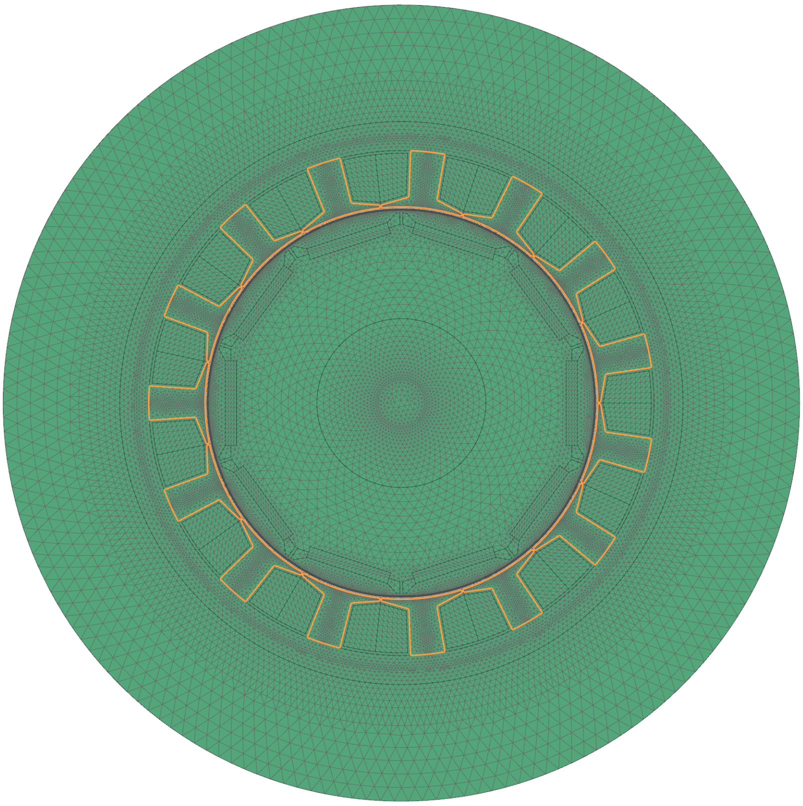

Figure 9.2: The complete EM model results.

The simulation calculates a lumped force for each tooth of the stator. Unlike the FE simulation framework, the concentrated force is the result of integrating all the nodal force densities acting on the tooth, including the portions of the tooth that extend beyond those making up the inner face of the stator. The results are organized into x-axis and y-axis components of the lumped force. The radial components of the lumped forces are computed for each tooth, so 15 lumped forces results are listed in function of the time steps. These values are then used as inputs for the State Space model.

10. The State Space model

State space models are mathematical frameworks used to describe the behavior of dynamic systems. These models represent the system's state variables and their time evolution using a set of first-order differential equations. The state variables capture the essential information about the system at any given time, and the state space representation provides a compact and efficient way to analyze and simulate the system's dynamics.

In the case study, the dynamic system represents the equivalent vibroacoustic model of the FE simulation framework. The state space model is data-derived, encompassing both the structural dynamic behavior of the stator in the electric motor and the propagation of sound waves from the motor's structure to the microphone point. The results are given in terms of acoustic pressure level in the time domain, referring to the simulation rotational speed. The acoustic pressure level signal is then processed using a Fourier transform to obtain the frequency domain signal, which is subsequently compared with the results from the FE framework.

In this project, a modal-based approach is used to derive the state space model from a set of measured frequency response functions (FRFs). This approach utilizes the Polymax modal parameter estimator to develop a modal model, which is then refined using the iterative MLMM algorithm. The clear stabilization diagram produced by Polymax serves as a valuable tool to determine the system's order under test. Once the order of the system is determined, the derived modal model is then converted into an equivalent state space model [5]. The entire procedure is performed on Siemens software Simcenter Testlab, which receives as inputs the FRFs and computes the State Space matrixes.

The state space representation of a dynamic system consists of two main equations: the state equation and the output equation. The state equation describes how the state of the system evolves over time. It is given by:

$$\dot{x}(t) = Ax(t) + Bu(t)$$

where:

- $\dot{x}(t)$ is the time derivative of the state vector $x(t)$, representing the rate of change of the system's state.
- A is the state matrix, which defines the relationship between the current state $x(t)$ and its time derivative $\dot{x}(t)$.
- B is the input matrix, which defines how the control input $u(t)$ influences the state of the system.
- $u(t)$ is the input vector, representing external inputs to the system.

The output equation describes how the current state and inputs of the system produce the observable outputs. It is given by:

$$y(t) = Cx(t) + Du(t)$$

where:

- $y(t)$ is the output vector, representing the observable outputs of the system.
- C is the output matrix, which defines the relationship between the state vector $x(t)$ and the output $y(t)$.
- D is the feedthrough matrix, which defines the direct relationship between the input $u(t)$ and the output $y(t)$.

The frequency response functions used to originate the State Space model are computed on the 3D vibroacoustic model of the FE framework, with some modifications. Instead of pre-processing and mapping the nodal force densities resulting from the 2D EM model, the inputs of the simulations are unit forces applied radially to selected nodes on the inner surface of the stator. The output of the FRFs is the acoustic pressure level, so the State Space model computes the equivalent of the sum of the effects of the different FRFs excited by the lumped forces in terms of acoustic pressure level. Figure 10.1 illustrates the selected nodes, 10 for each tooth. Since there are 15 teeth, the simulation computes 150 different FRFs.

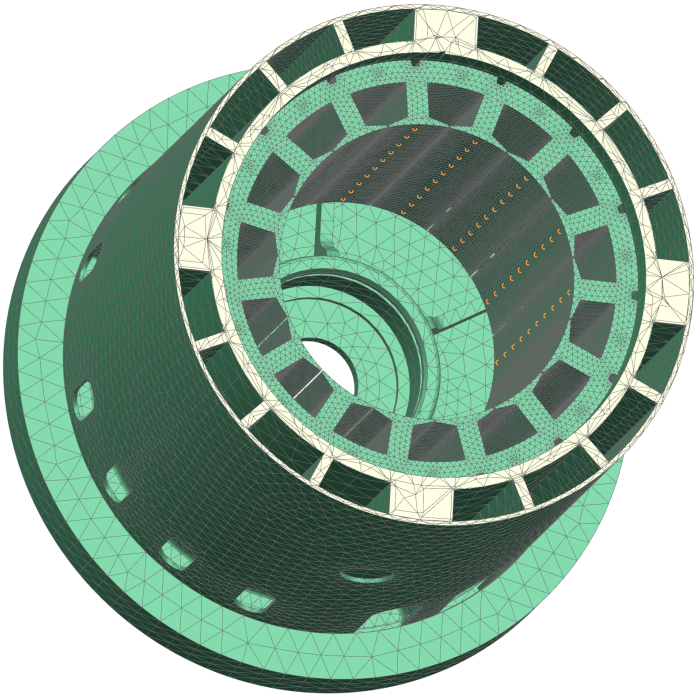

Figure 10.1: The selected nodes for FRF computation.

The frequency response functions are then processed using the Simcenter Testlab modal-based algorithm to derive the State Space model. The number of FRFs matches the number of lumped force inputs required by the State Space model: 150 in total. However, the lumped forces are only 15 because they are computed in the 2D model of the motor, which outputs one lumped force for each tooth. Therefore the lumped force is assumed to be homogeneous on the longitudinal direction of the electric motor and the results values obtained from the EM model are split equally on the 10 points of the tooth.

Figure 10.2 depicts 3 different frequency response functions, from 3 random points on different teeth.

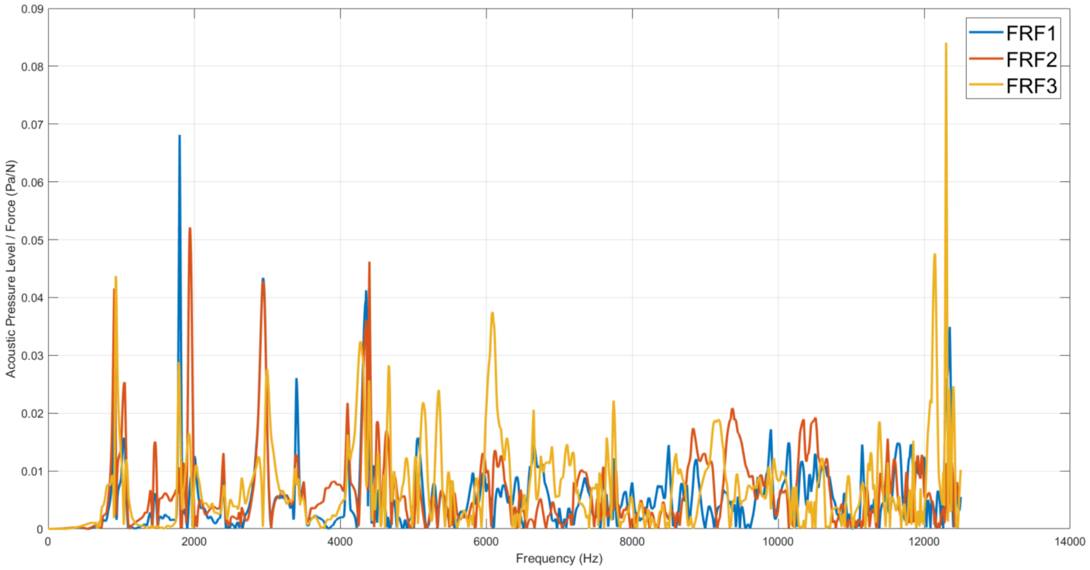

Figure 10.2: Frequency Response Functions.

11. Results of the FE simulation framework

The FE simulation framework consists of four interconnected models designed to compute the acoustic pressure level of the electric motor under constant rotational speed conditions. This chapter focuses on elaborating and analyzing the outputs derived from the different models to determine the acoustic pressure level on the microphone point.

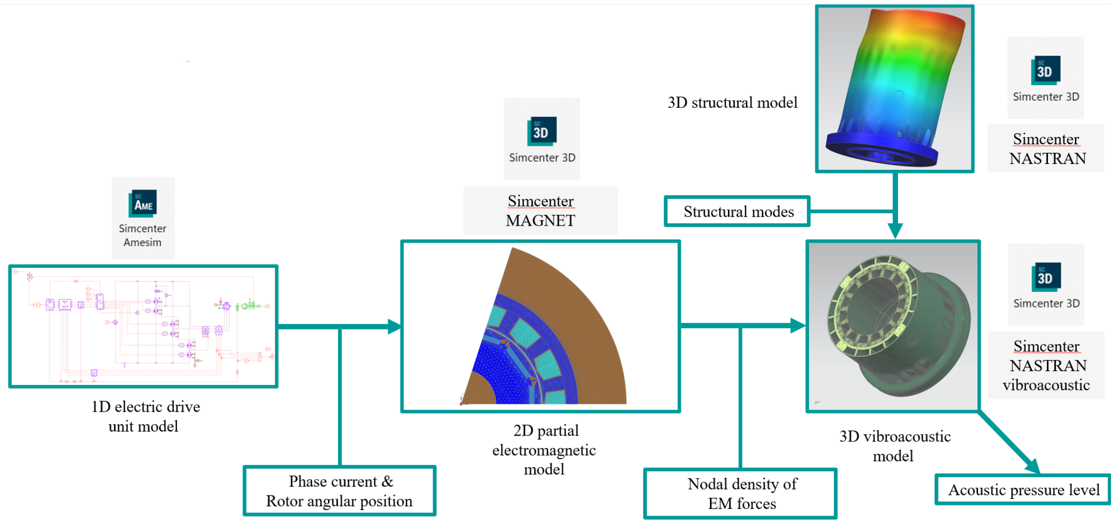

Figure 11.1: The FE simulation framework

The simulation framework has been improved by applying two major modifications to the simulation setup and results elaboration, described in section 11.2 and in section 11.4. The results from this framework are then compared to the ones obtained from the State Space framework in Chapter 12.

11.1 Results of the 1D electric drive unit model

The electric drive unit model setup is described in Chapter 5. This functional model computes the rotor angular position and the three-phase currents, which are then utilized as inputs for the 2D EM model. Both the results are in time domain. The first approach has the Electric machine block, described in Subsection 5.3.5, implementing a linear submodel with constant physical characteristics described by the electric motor's design parameters. This means that the EM properties in the electric motor's air gap do not depend on the angular position.

During the simulation, the rotational speed increases until it stabilizes at the target value. The model is configured to start printing output values from 0.6 seconds after the simulation begins, ensuring that steady-state conditions are achieved. Figure 11.2 illustrates the rotational speed trend in comparison to the reference value, in particular referring to a target rotational speed of 1300 RPM. The highlighted area corresponds to the period when the results are printed in the output dataset.

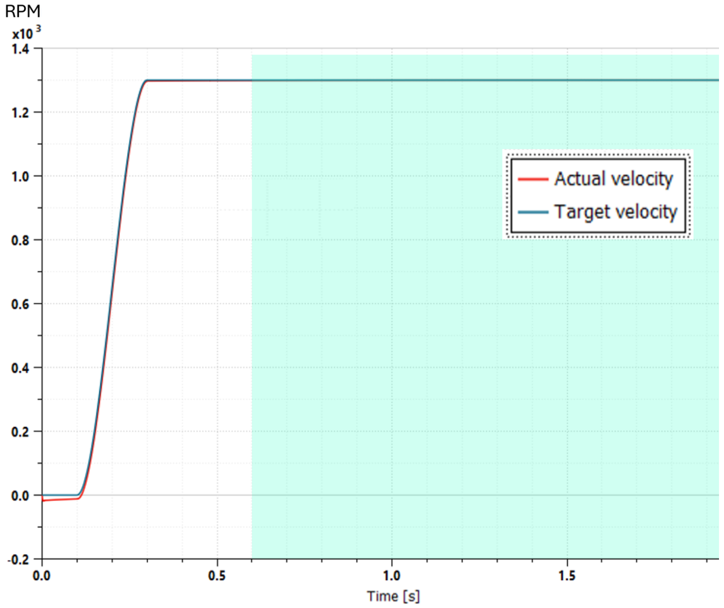

Figure 11.2: Target and actual values of the rotational speed of the electric motor.

The FE framework has been employed to obtain results across a range of rotational speeds from 500 RPM to 1500 RPM, with increments of 100 RPM.

Figure 11.3 and Figure 11.4 illustrate the results for a rotational speed of 1300 RPM, chosen as a representative example to perform the analysis of the results and the processing necessary to transfer them as input for the 2D EM model.

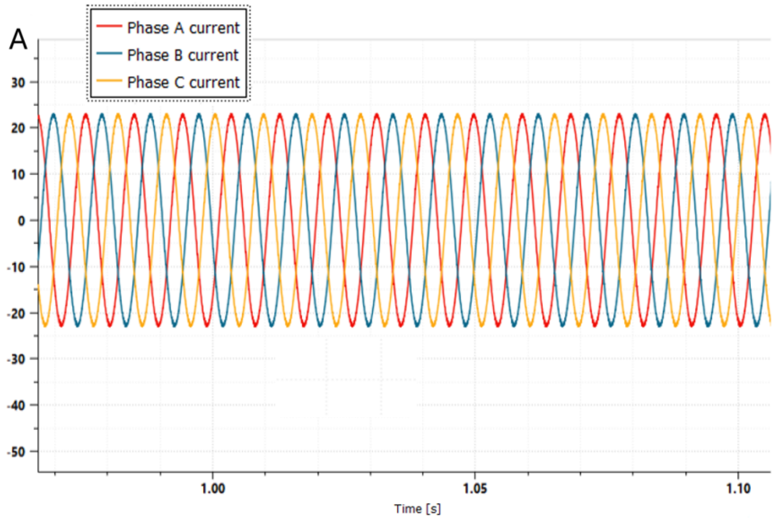

Figure 11.3: The output three-phase currents.

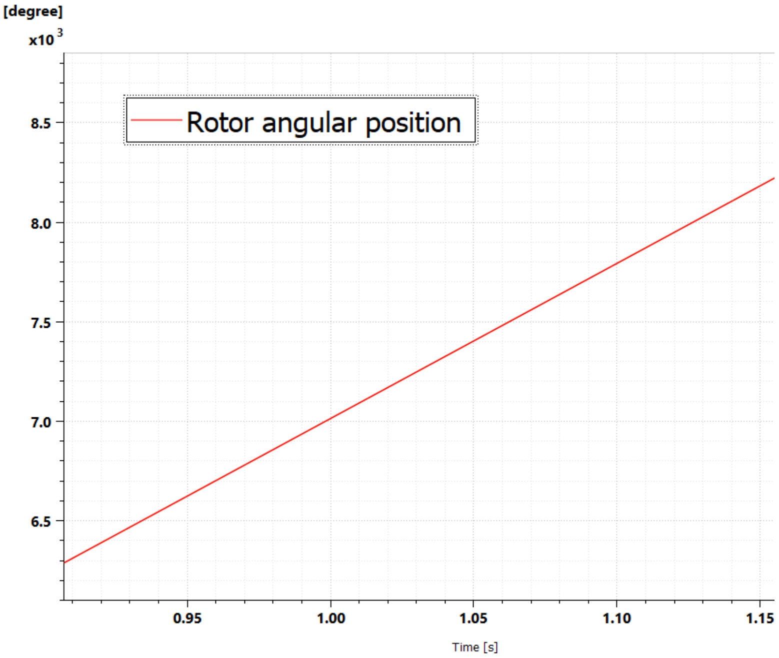

Figure 11.4: The rotor angular position.

Figure 11.4 shows that the rotor angular position is characterized by values that exceed 360°. This happens because the angular position sensor is incremental and does not reset every complete revolution. In the case study, the angular position is reset every 72°, which is the final position of the 2D EM partial model. Therefore, each one of the repetitions can be extracted and used as input for the subsequent simulation, along with the relative three-phase currents. As discussed before, this corresponds to one complete electric cycle.

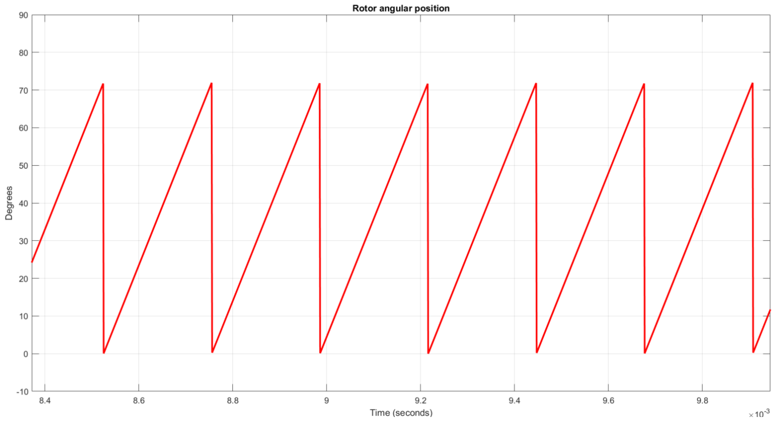

Figure 11.5: Rotor angular position, reset every electric cycle.

This output is generated as a piecewise file, a type of file that breaks down the data into discrete segments or intervals, in this case listing them with the corresponding time steps.

In order to extract the useful data that serves as input for the 2D EM simulation, the three-phase currents and the rotor angular position dataset are cut as illustrated in Figure 11.6.

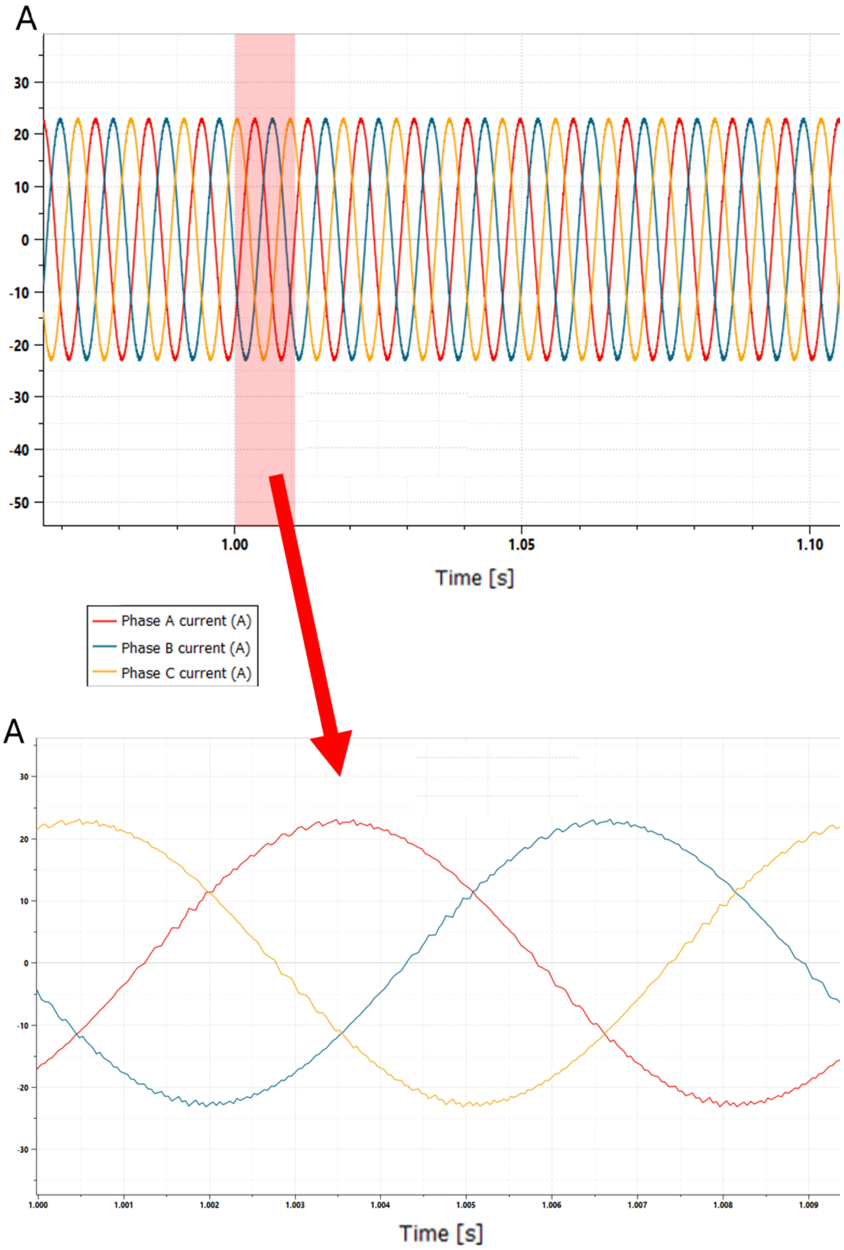

Figure 11.6: The extracted three-phase currents.

The graph magnification illustrated in Figure 11.7 highlights the ripples present in the current characteristics. These distortions, caused by the inverter switching mechanism, are the main responsible for the characteristic high-pitch component in the acoustic noise produced by PWM-fed electric machines [9].

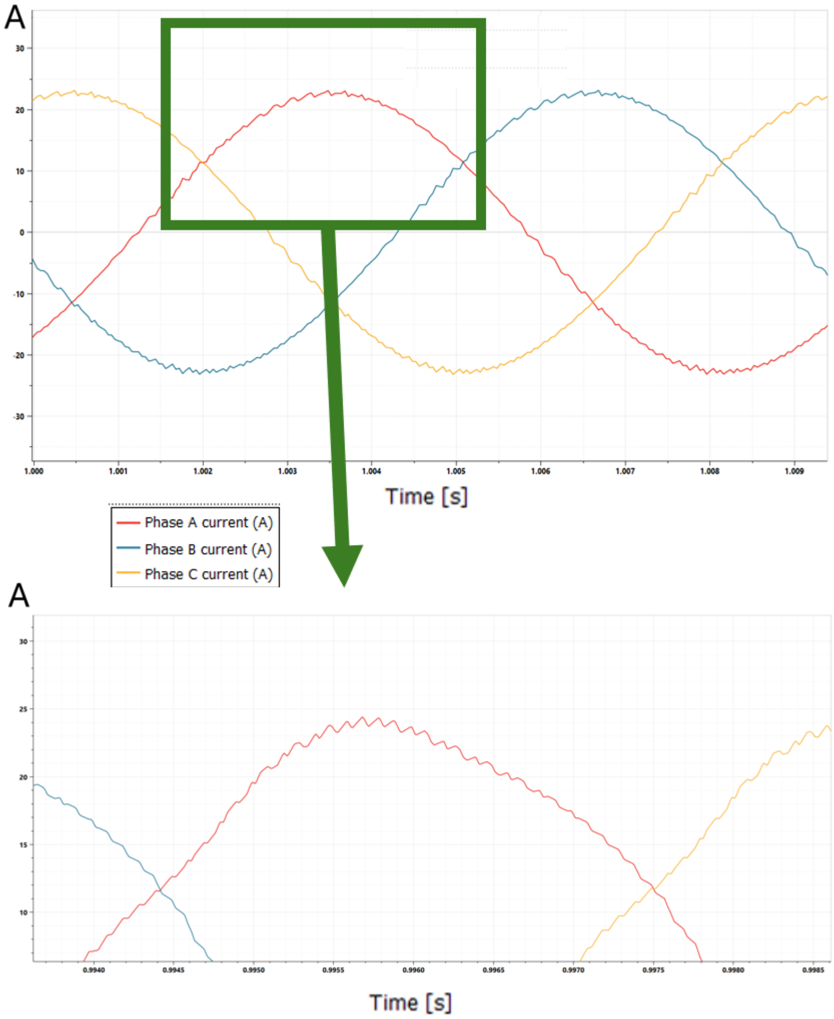

Figure 11.7: Current ripples.

The challenge of correctly introducing the data produced by the functional model as inputs in the EM simulation lies in accurately matching the initial positions of the rotor in the two models. As discussed before, the rotor angular position printed in the piecewise file begins with an offset. Furthermore, the starting angular position of the electric motor block itself, from which the rotor angular position information is obtained, is not a reliable indicator of the rotor position. There is no clear reference to determine the rotor's angular position in the 2D EM model that corresponds to the initial position of the electric motor block. The implemented linear submodel, described in Subsection 5.3.5, does not guarantee that the rotor's initial angular position is consistent between the two models.

Figure 11.8 illustrates a series of potential initial angular positions, along with the stator phases:

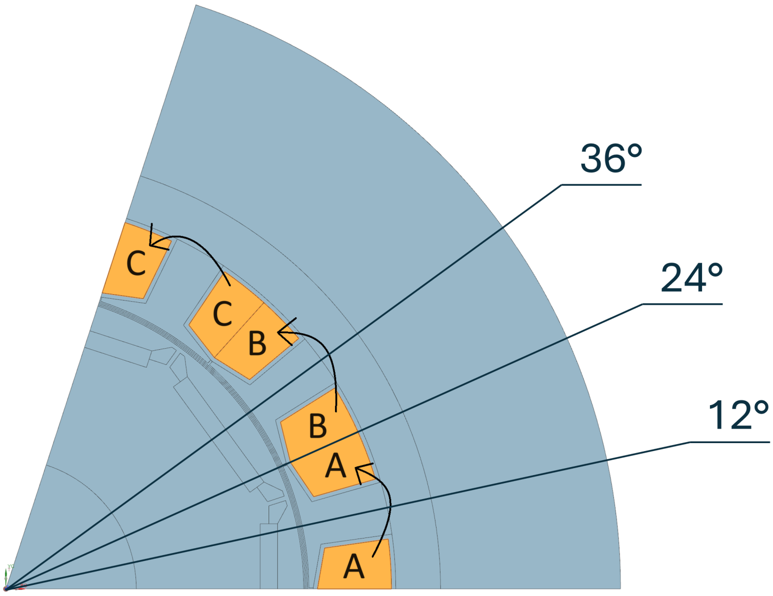

Figure 11.8: Potential initial position for the electric motor block on the 2D EM model.

The stator phases are depicted because the initial position of the rotor is typically placed across the phase A coils [33]: the 12° line above the horizontal plane in Figure 11.8. This indication has also been shared by the electric motor developer, but a verification procedure was nevertheless necessary to ensure the correct matching between the two models. The other initial positions have been selected randomly to serve as a verification.

11.2 Non-linear electric block submodel

The first major modification to the FE framework involved replacing the linear submodel of the electric motor with a non-linear submodel. In this updated approach, a non-linear, spatially-dependent submodel was implemented to more accurately represent the electromagnetic characteristics of the e-motor. Unlike the linear model, the flux linkage in the new submodel is decoupled between the direct and quadrature axes of the rotary reference frame and varies with the angular position. Additionally, the torque is another spatially-dependent parameter that also varies with the angular position.

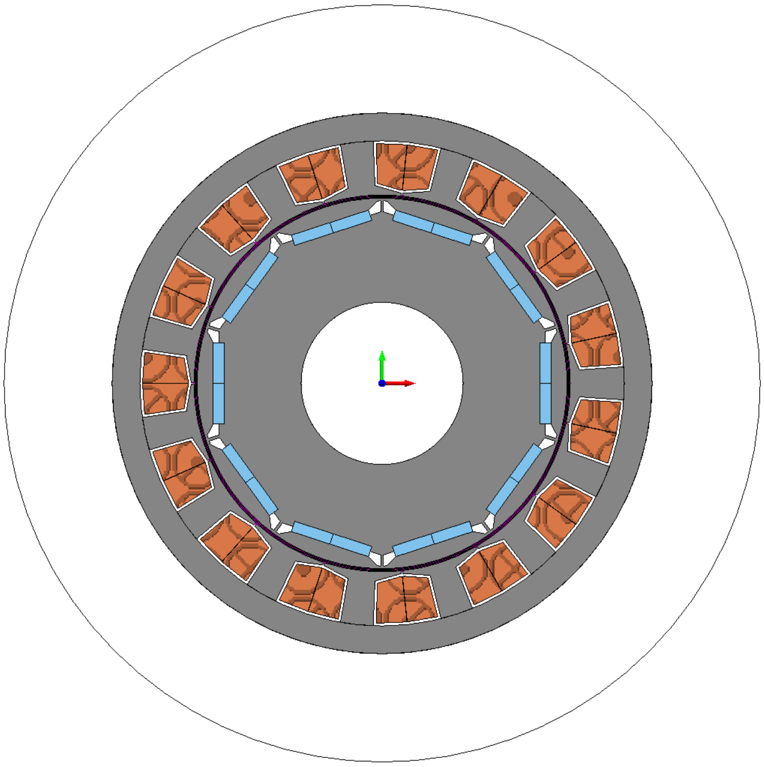

Figure 11.9: The 2D complete EM model.

As described in Subsection 5.3.5, the flux linkage on the q-axis, the flux linkage on the d-axis, and the torque characteristics have been determined using a separate 2D complete section EM model, which is not part of the FE simulation framework (Figure 11.9).

The implemented spatially-dependent submodel introduced slight oscillations in the speed, currents, and torque trends observed in the 1D electric drive unit simulations, as shown in Figure 11.10.

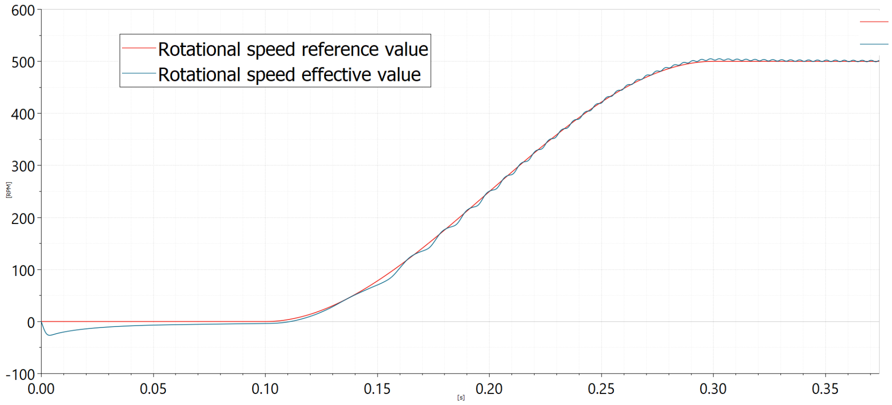

Figure 11.10: Comparison between reference and effective values of the rotational speed with non-linear submodel.

To verify the initial positions of the EM simulations, the torque characteristics computed from the electric drive unit model are compared to those computed from the EM model. Since the inputs for the EM model are derived from the same simulation that calculates torque in the functional model, the trends will only match if the datasets for currents and rotor angular positions are correctly mapped onto the EM model. This ensures that the initial positions of the two models are coherent.

Therefore, the 1D electric drive unit model has been modified to compute the torque on the electric motor shaft along with the three-phase currents and the rotor angular position. The torque characteristic has been determined through a simulation at 525 RPM. The torque data is extracted from the time domain dataset, with rotor angular position data being reset after each electric cycle, as discussed before.

The non-linear parameters were computed using a 2D EM complete model with the same physical features as the partial model. The initial position of these characteristics is set when the rotor is in the equivalent position of 12° in the partial model, following the previously mentioned guidelines. The subsequent verification can only confirm the coherence between the initial positions of the models, not the accuracy of these indications.

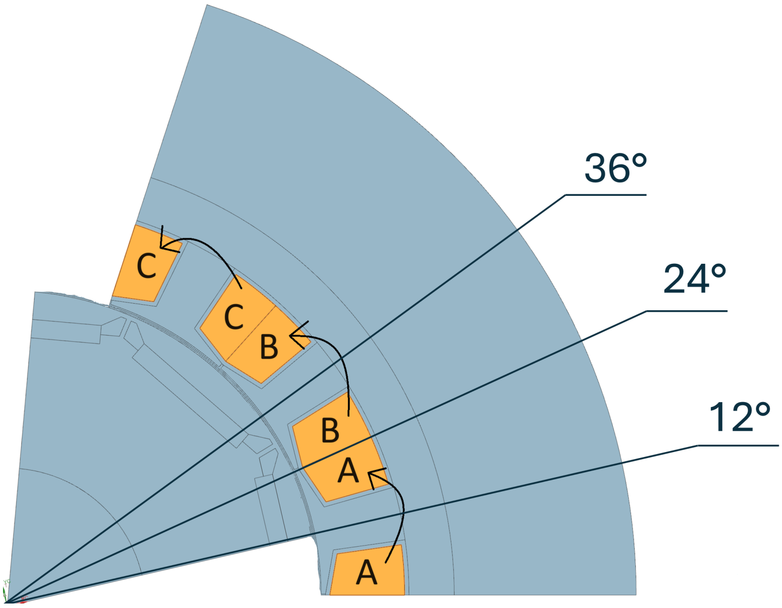

Figure 11.11: Rotor initial position in the EM model, according to the general guidelines.

The verification was carried out through iterative simulations in which the inputs of the EM simulation (rotor angular position and three-phase currents, computed by the same electric drive unit simulation that determines the torque characteristics) were offset to start the EM simulation at various potential initial angular positions, illustrated in Figure 11.11. The torque characteristic computed by the EM simulation was then compared to that of the functional model.

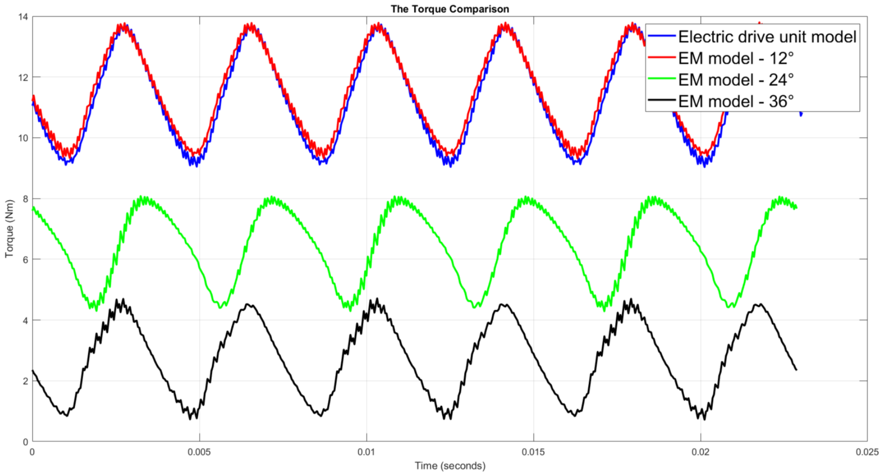

Figure 11.12: Torque characteristics.

As expected, the comparison between the torque characteristics of the two models shows that the correct matching is obtained when the initial position is 12° above the horizontal plane. This ensures that the outputs computed from the electric drive unit model are correctly mapped onto the 2D partial EM model and also verifies that the non-linear submodel in the electric machine block is set up correctly.

11.3 Results of the 2D FE Electromagnetic model

The 2D partial EM model receives the three-phase currents and rotor angular position signals as inputs from the 1D electric drive unit model. These datasets are accurately mapped onto the EM model to ensure consistency in the initial positions between the two models. As detailed in Chapter 6, the purpose of the EM simulation is to compute the nodal force densities acting on the inner surface of the stator. These EM forces need to be mapped onto the 3D vibroacoustic model for further analysis.

Since the EM forces refer to a partial 2D model, they must undergo a preprocessing procedure before being used as inputs for the simulation. The preprocessing of the input forces includes:

- **Extension from sector to full section**: The dataset is replicated spatially five times to complete the section. Figure 11.13 illustrates the dataset in green and the replicated sections in red.

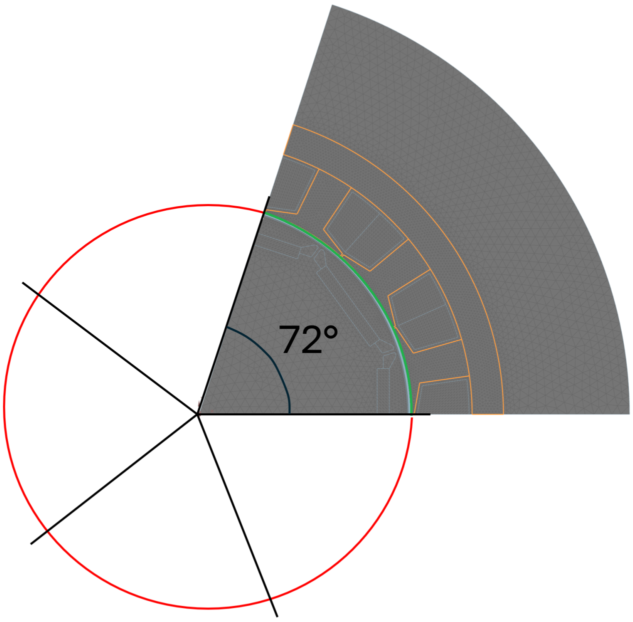

Figure 11.13: Extension from sector to full section.

- **Extrusion from 2D to 3D**: The complete section EM forces are extruded into a cylindrical shape, matching the length of the stator stack (150 mm).

- **Mesh mapping**: The EM forces have been computed on a 2D mesh, which differs from the mesh used in the 3D vibroacoustic model. The mesh mapping process between these two different models involves transferring data, such as the analyzed EM forces, from the 2D mesh to the 3D mesh. This process ensures that the results from the 2D computational analysis are accurately applied to the 3D model, despite the differences in mesh configuration. Figure 11.14 illustrates an example of mesh mapping between two different 2D models, the one on the left is an EM mesh while the one on the right is a structural mesh. Figure 11.15 presents the results of the mesh mapping process referring to the case study.

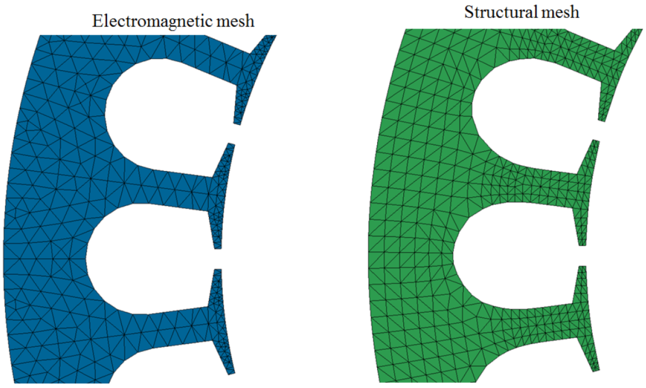

Figure 11.14: Mesh mapping example.

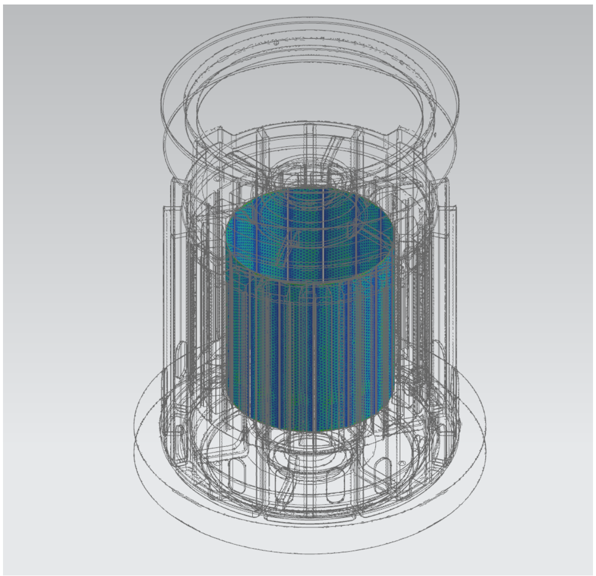

Figure 11.15: Mesh mapping process result.

- **Time signal processing**: The signal containing the input forces is in the time domain, referring to the time steps set up in the EM simulation. On the other hand, the vibroacoustic simulation is in the frequency domain, so the input signal has to undergo a Fourier Transform process.

To investigate the frequency components in the nodal force densities, a representative node is selected on the stator surface after completing the pre-processing. Figure 11.16 depicts the results of the mesh mapping process. The depicted nodal force densities refer to a rotational speed of 1300 RPM and the frequency displayed is 77.38 Hz.

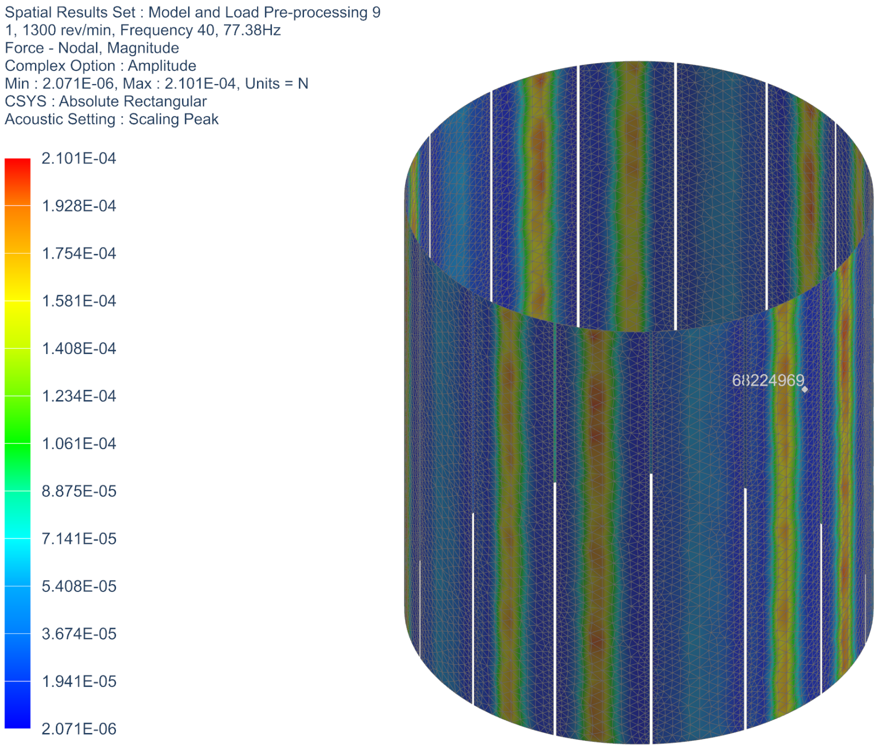

Figure 11.16: Pre-processed nodal force densities.

The frequency spectrum referring to the EM force acting on the selected node is then depicted in Figure 11.19.

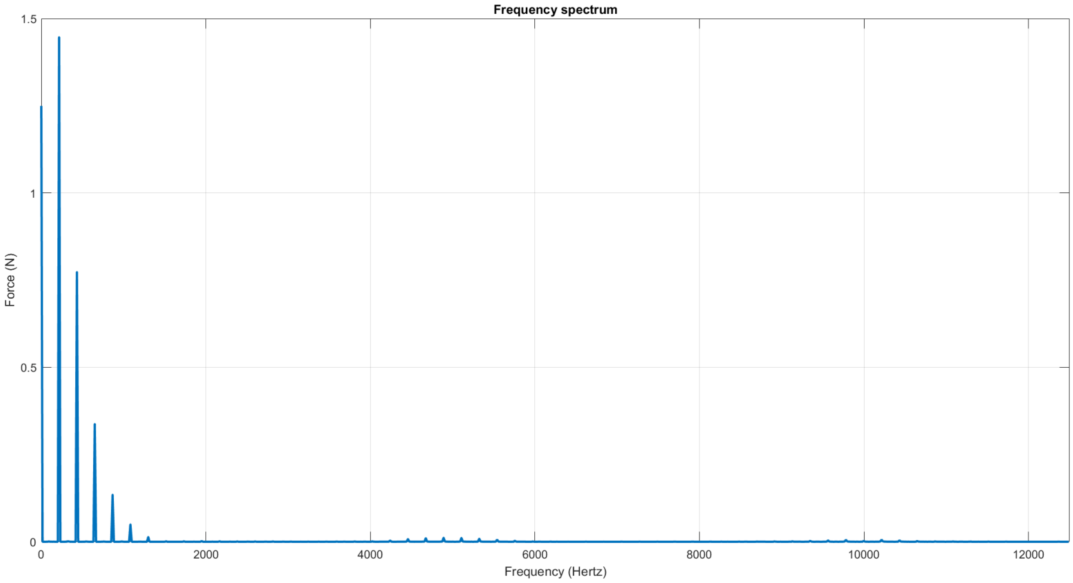

Figure 11.17: Frequency spectrum.

The graph in Figure 11.18 shows a magnification of the frequency spectrum, focusing on the PWM harmonics.

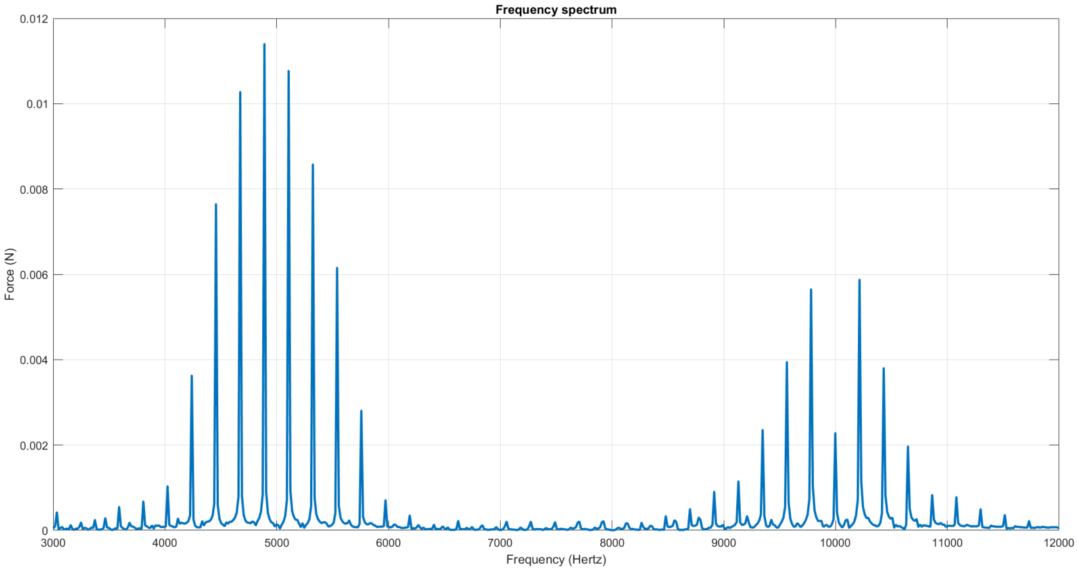

Figure 11.18: PWM harmonics.

The peaks in the left part of the frequency spectrum, spanning from 0 to 2000 Hz, are associated with slotting effect harmonics. The slotting effect is the consequence of the impact of the stator and rotor slots on the motor's electromagnetic performance, particularly in terms of noise and vibration. The slots create periodic variations in the air gap magnetic field, which induce harmonic components in the electromagnetic forces acting on the motor.

Additionally, the harmonics of the PWM carrier frequency, which is set at 5000Hz, result from the switching actions of transistors in the inverter arms. These high-frequency components are transmitted from the stator currents to the magnetic field in the air gap and ultimately influence the electromagnetic forces acting on the inner surface of the stator, leading to distinct peaks in the frequency spectrum.

Figure 11.18 clearly shows the carrier frequency's first and second harmonics. As described by other literature works [9] [34] [35], the PWM harmonics present multiple peaks:

- **First harmonic:** The first significant harmonic is at the fundamental switching frequency, that in the case study is set at 5000 Hz;
- **Higher-order harmonics**: Higher-order harmonics occur at integer multiples of the switching frequency. The entire simulation framework covers a maximum frequency range of 12,500 Hz, in order to be able to capture the effects of the second harmonic of the PWM, which is located at 10,000 Hz;
- **Sideband harmonics**: In addition to the main harmonics, sidebands can appear around the harmonic frequencies due to the interaction between the switching frequency and the fundamental electrical frequency of the motor. These sidebands are spaced at multiples of the motor's electrical frequency around the primary harmonics.

In the case study, the first harmonic of the PWM signal lacks a central band, evidenced by the absence of a peak at 5000 Hz. Instead, it is characterized by very prominent sidebands. Conversely, the second harmonic does exhibit central bands, but its peak is lower than that of the sidebands. These results align with expectations, as similar patterns have been documented in other literature works [9].

The previous analysis focused on a specific rotational speed of 1300 RPM. To gain a more comprehensive understanding of the e-motor orders and the impact of PWM harmonics at various rotational speeds, a Campbell diagram is illustrated in Figure 11.19. This allows for a detailed analysis of the frequency response across different operating conditions.

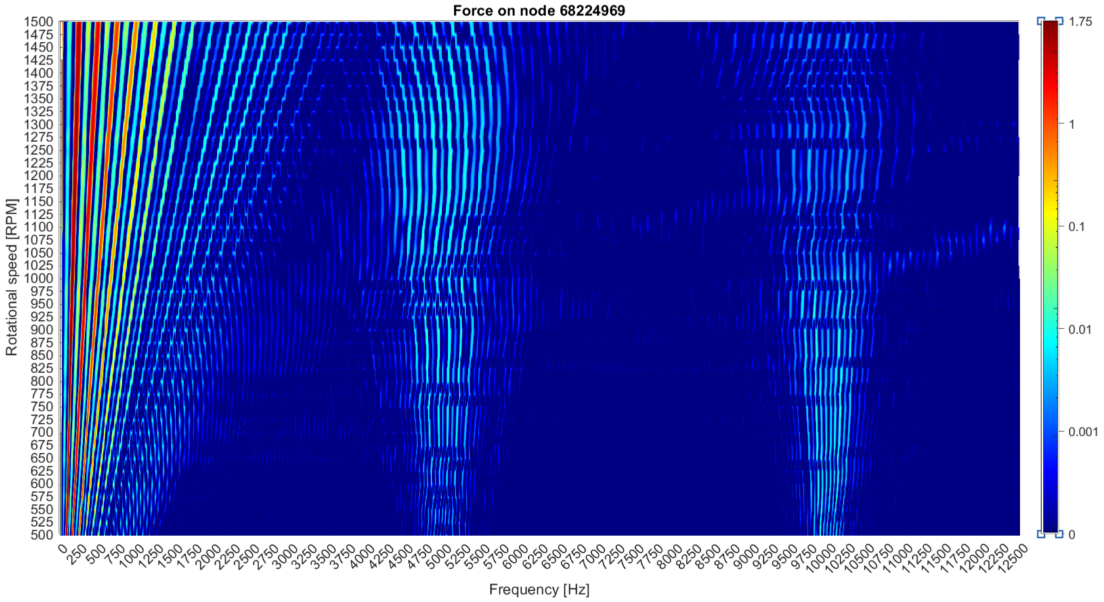

Figure 11.19: Campbell diagram.

The e-motor orders are clearly visible and behave as expected [36]. The logarithmic scale highlights the strong impact of the slotting effect on the electromagnetic forces, with order lines without offset (originating from 0 RPM, 0 Hz). The slope of each line corresponds to the specific order, where the 1st order has a steeper slope compared to higher orders.

The PWM harmonics are not clearly visible, and the sidebands are barely discernible for both the first and second harmonics of the carrier frequency. In the higher rotational speed region of the Campbell diagram, the band lines appear to lean left instead of spreading in straight lines as expected [34]. This "smearing" effect on the PWM harmonics is caused by spectral leakage [37]. To address spectral leakage and improve results, it is necessary to investigate the periodicity of the EM forces signal before applying a Fourier transform.

11.4 Signal periodicity

Ensuring that a signal is periodic before applying a Fourier transform is crucial to avoid spectral leakage, which can distort the analysis of the signal's frequency components: the Fourier transform inherently assumes that the signal is periodic by representing it as a sum of sinusoidal components [37]. When a signal is not periodic within the observation window, the transform effectively "sees" a discontinuity at the boundaries [38]. Figure 11.20 shows a non-periodic signal within the observation window, which is highlighted in light blue.

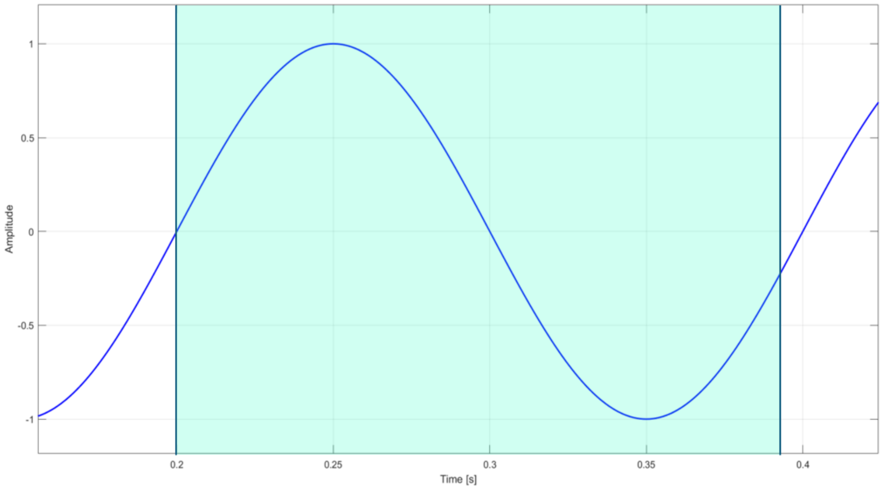

Figure 11.20: Non-periodic signal within observation window.

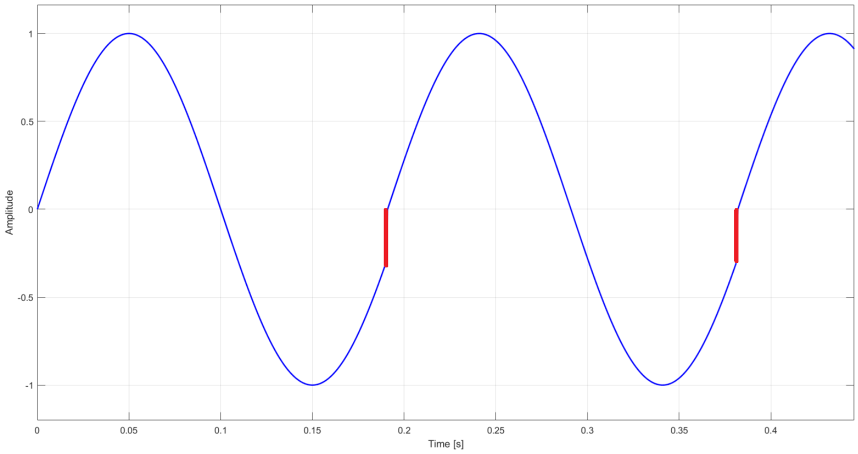

Figure 11.21: Non-periodic signal as "seen" by the Fourier transform.

In Figure 11.21 the discontinuity between consequent signals is highlighted in red. These abrupt jumps introduce high-frequency components that were not present in the original signal, which spread energy across the frequency spectrum. Instead of having sharp, distinct peaks at the actual frequencies of the signal, the energy "leaks" into adjacent frequencies. This smearing effect obscures the true spectral content, making it difficult to identify and measure the signal's frequency components accurately.

To mitigate the spectral leakage the following countermeasures are avaiable:

- **Extending the signal length**: Applying windowing functions can help reduce the impact of boundary discontinuities. These functions taper the signal at the edges, minimizing abrupt changes. In the study case, a Hanning windowing function had already been applied to the signal, but its effect is insufficient because it is linked to the signal length. The EM partial model has been set up to perform simulations lasting only one electrical cycle. This means that the time-domain signal of the electromagnetic forces is too short for the windowing function to be effective. At 1000 RPM, the duration is 0.012 s, but it decreases to 0.008 s as the rotational speed increases to 1500 RPM. Figure 11.21 shows the same non-periodic signal as Figure 11.21, after applying the Hanning window. Since the original signal was a pure sine wave, it's clear that the effect of the windowing function is not sufficient for short signals.

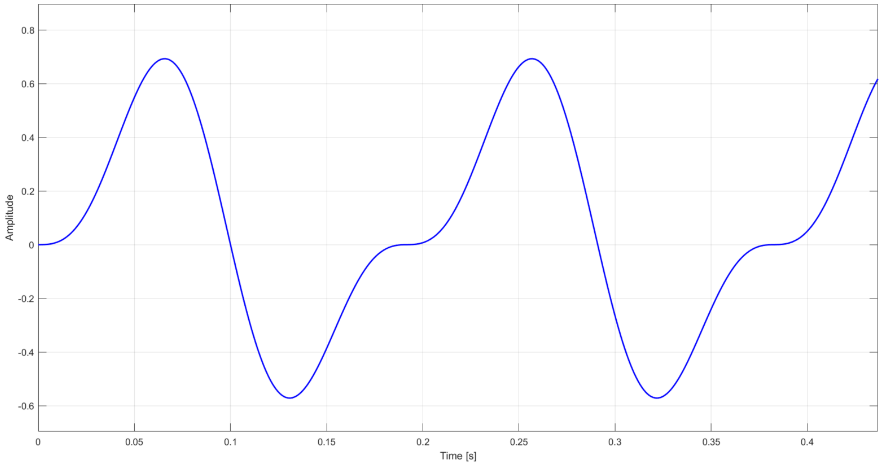

Figure 11.22: Windowed non-periodic signal.

- **Signal Conditioning**: Ensuring that the signal data is collected over an integer number of periods can enhance the Fourier transform results by making the signal appear periodic within the window. The initial approach of simulating one electric cycle should have addressed this, but the issue arises from the secondary frequency introduced by the inverter modulation.

The first point is implemented by extending the length of the currents signal to encompass multiple electric cycles. The number of electric cycles included in the current signal is not constant between different simulations: it increases with the rotational speed. This adjustment ensures the signal length remains as constant as possible despite varying rotational speeds, improving accuracy. Although this increases the computational time of the EM simulation, it remains more efficient than a complete section model. Table 9.1 compares the computational times, referring to simulations conducted at a rotational speed of 1000 RPM, whose extended simulation includes four electric cycles.

Model	Computational Time
Complete	11 min and 32 sec
Partial	5 min and 10 sec
Partial, extended simulations	8 min and 10 sec

Table 11.1: Comparison in the model computational time

The following table lists the number of electric cycles included in the simulations and the relative signal length:

Rotational speed [RPM]	Included electric cycles	Simulation time (s)
500	3	0.072
750	4	0.064
1000	6	0.072
1250	7	0.0672
1500	9	0.072

Table 11.2: Extended simulation time

Since a complete revolution consists of five electric cycles, simulations at rotational speeds of 1000 RPM and higher extend beyond a single revolution.

The second point is implemented by performing an "angular resampling" procedure of the three-phase currents. The current and the rotor angular position signals are originally computed by the 1D electric drive unit model in the time domain, printed in a piecewise file, and referring to time steps with a frequency sample of 25000 Hz. However, the extracted data was not periodic. Figure 11.23 illustrates the Phase A one-electric-cycle signal, used in the initial approach, replicated 5 times. The non-resampled data was not perfectly periodic and the little discontinuity highlighted by the orange dots in the magnification is enough to cause significant spectral leakage.

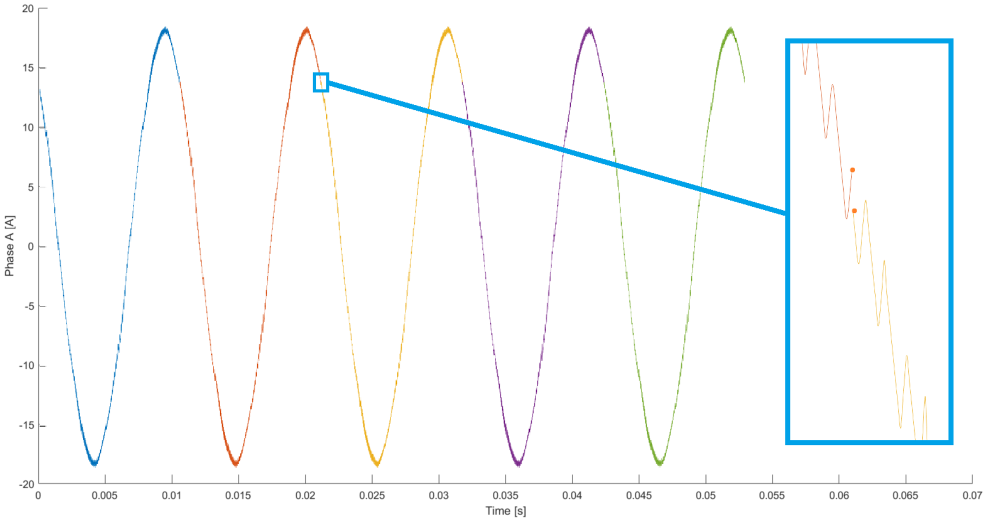

Figure 11.23: Replicated one electric cycle signal.

The resampling procedure converts the currents dataset from the time domain to the angular domain, producing a new dataset with values of the three different phases at an angular step of 0.2°. Implementing the resampled datasets in the EM model helps minimize discontinuity at the boundaries of the input signal. For example, in the simulation referring to a rotational speed of 800 RPM, 5 electric cycles are included: this is the equivalent of a complete revolution. With an angular step of 0.2°, Phase A's second-to-last value corresponds to 359.6°, and the last value to 359.8°. The next step is exactly 0° at the other end of the signal, ensuring signal continuity. For example, without resampling the last value could have been 359.5° and the first 0.6°, but the angular step should have been 0.3°, so this would have caused causing discontinuity.

Figure 11.24 shows the extended and resampled signals referring to 800 RPM, with the orange dots highlighting the boundaries of the signal.

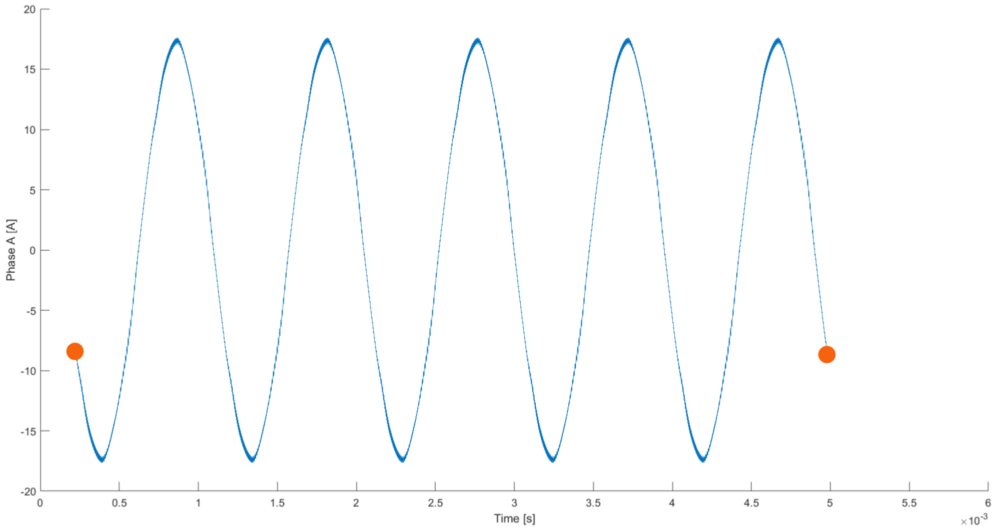

Figure 11.24: Extended and resampled signal.

After the two points have been implemented in the FE framework, the simulations have been repeated with this second approach to ensemble again the Campbell diagram, illustrated in Figure 11.25.

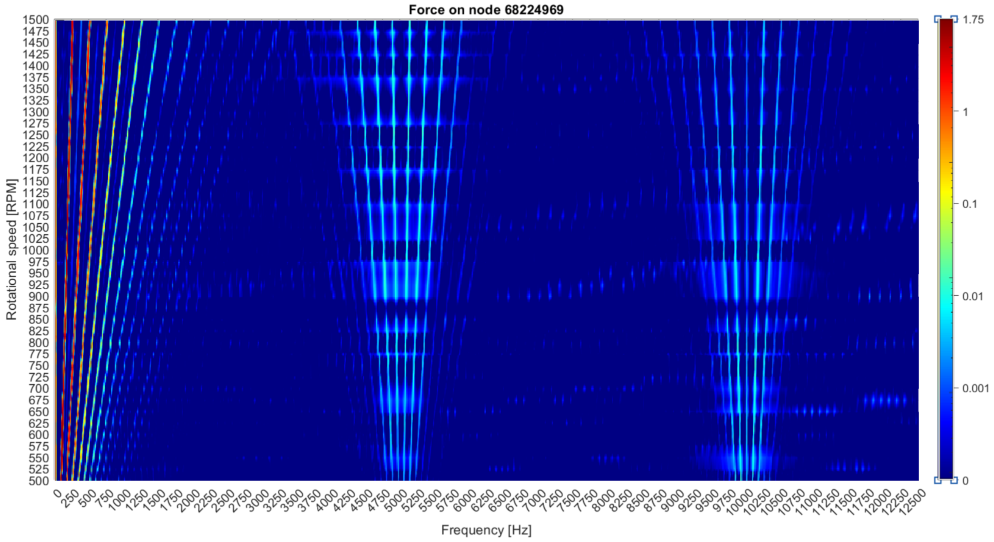

Figure 11.25: Campbell diagram, obtained with extended and conditioned signals.

To facilitate the diagram comparison, the Campbell diagram resulting from the first approach is presented again in Figure 11.26.

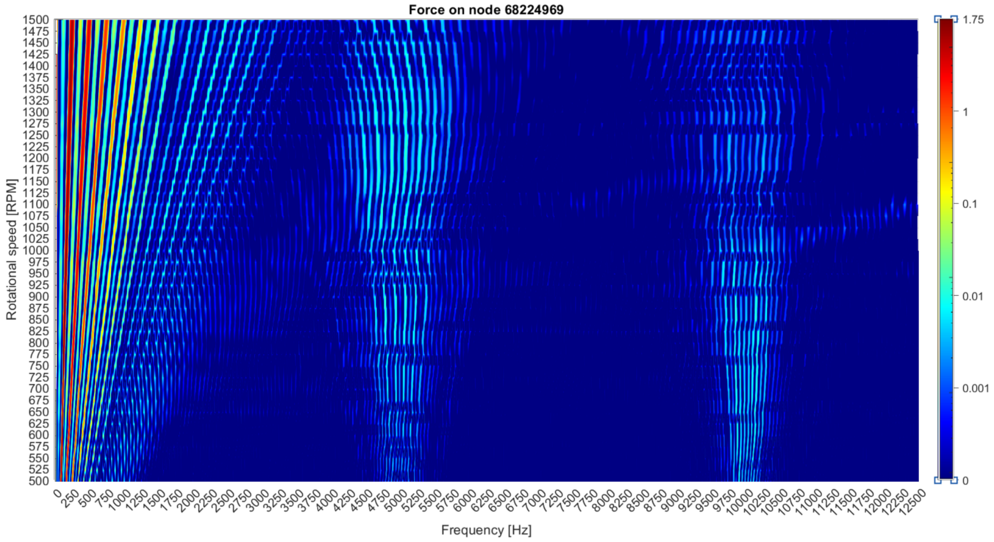

Figure 11.26: Campbell diagram, obtained without extended and conditioned signals.

The comparison between the Campbell diagrams demonstrates notable enhancements attributed to the reduction in spectral leakage. The slotting effect harmonics are distinctly visible on the left side of the diagram, as the e-motor orders become even more discernible. This improvement results from the corrective measures applied to the signal, which enhanced the periodicity of the phase currents to such an extent that it was no longer necessary to apply the Hanning windowing function before performing the Fourier Transform on the EM forces.

Figure 11.27 presents a comparison between the frequency spectrum at a rotational speed of 675 RPM, with a focus on the first harmonic of the PWM. The blue trend corresponds to a signal length of one electric cycles without resampling, while the orange trend corresponds to 9 electric cycles with resampling. Neither trend applied Hanning windowing, indicating that the observed improvements are solely due to enhanced signal periodicity.

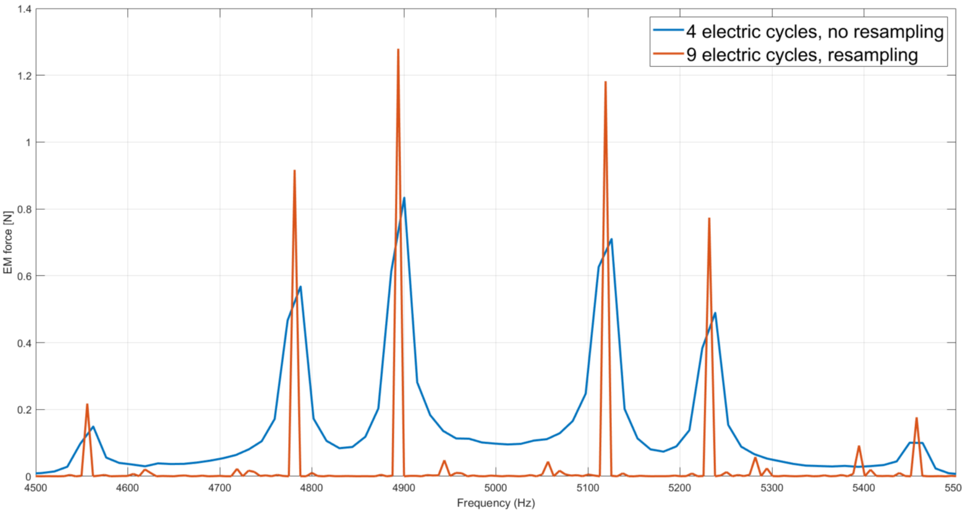

Figure 11.27: Frequency spectrum comparison between the first and second approach.

Since the Hanning windowing function typically results in wider and lower peaks, its removal leads to narrower and higher peaks, which is exactly what the adjourned Campbell diagram in Figure 11.25 shows. The PWM harmonics exhibit a characteristic spreading pattern that increases with rotational speed. This pattern occurs because the frequencies of the sidebands are a combination of the carrier frequency and the fundamental frequency of the signal. The fundamental frequency of the signal is the frequency of the alternating currents, which increases with the rotational speed in synchronous electric motors [34].

Contrary to the e-motor orders, which now appear very clean and discernible at any rotational speed, the PWM harmonics still present a certain degree of Spectrum leakage for some datasets. Figure 11.28 depicts the comparison of the first harmonic of the carrier frequency between the rotational speeds of 950 RPM and 1000 RPM. The analysis focuses on the first harmonic of the PWM carrier frequency.

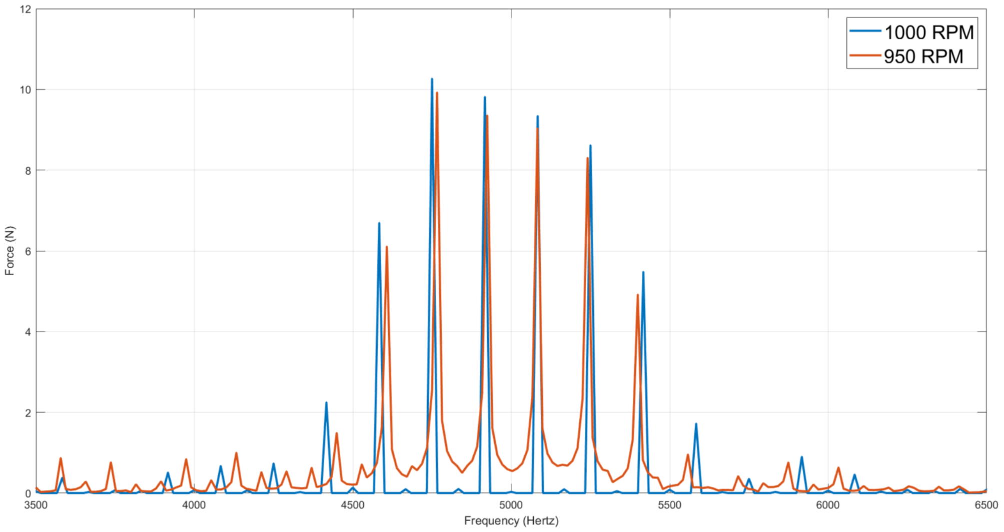

Figure 11.28: Frequency spectrum comparison between different rotational speeds.

Even though the quality of the results has been improved, the smearing effect remains visible at certain rotational speeds, such as the 950 RPM signal in Figure 11.28, because the simulation's signal is still not perfectly periodic. The problem can again be traced back to the three-phase currents. This current signal consists of two main harmonic components: the fundamental frequency and the PWM-source signal. While the resampling procedure ensures the perfect periodicity of the fundamental frequency component, it does not achieve the same for the secondary frequency linked to the PWM carrier frequency. The challenge in achieving a simulation without any spectral leakage lies in determining the appropriate simulation time for each rotational speed, ensuring the signal boundaries are perfectly periodic for both the primary and secondary harmonic components. However, extending the signal by including multiple electric cycles and resampling the signals has significantly improved the results.

11.5 Results of the 3D structural model

The 3D structural model computes the mode shapes of the stator structure. Some examples are illustrated in the following Figure:

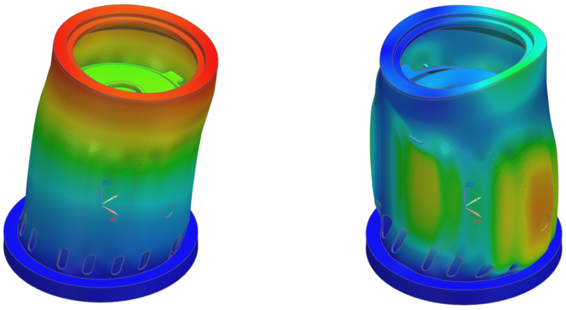

Mode 1 Mode 6

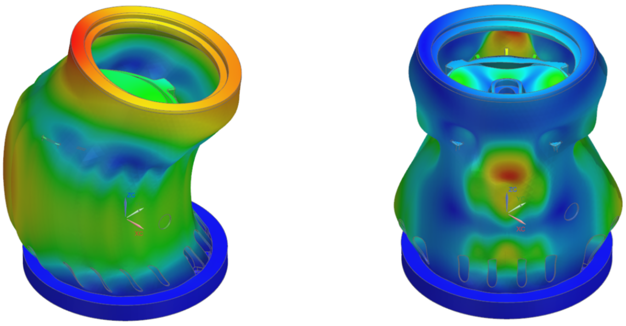

Mode 9 Mode 15

Figure 11.29: Mode shapes.

The following table lists the frequency of the mode shapes illustrated in Figure 11.29.

Mode shape number	Frequency
1	912 Hz
6	1927 Hz
9	2010 Hz
15	3426 Hz

Table 11.3: Frequencies of the mode shapes.

The 3D structural simulation computed a total of 376 mode shapes within a frequency range of 16,000 Hz. Prior to integrating the data into the subsequent 3D vibroacoustic model, certain mode shapes were excluded from the results dataset. These excluded mode shapes exhibited local displacements in non-critical areas, such as the unconstrained top end of the electric motor. Since this part of the motor was simplified during the design stage, excluding these local mode shapes was deemed an acceptable approximation. Figure 11.30 shows two examples of excluded mode shapes:

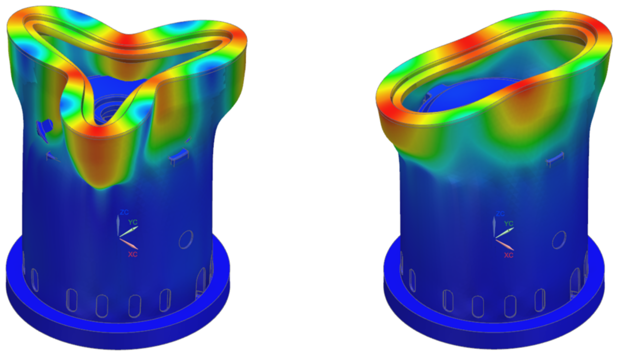

Mode 8 Mode 18

Figure 11.30: Excluded mode shapes.

The following table lists the frequency of the mode shapes illustrated in Figure 11.30.

Mode shape number	Frequency
8	1990 Hz
18	4013 Hz

Table 11.4: Frequencies of the excluded mode shapes.

The mode shapes have been assigned an arbitrary modal damping value of 2%. Modal damping refers to the mechanism by which vibrational energy is dissipated in a structure. It is a critical parameter in structural dynamics, influencing how quickly vibrations decay. By assigning a damping value of 2%, a moderate level of energy dissipation is simulated in the mode shapes, which helps in predicting more realistic dynamic behavior of the structure.

11.6 Results of the 3D vibroacoustic model

The final model in the workflow of the FE simulation framework receives the preprocessed electromagnetic forces and the mode shapes from the previous simulations. The acoustic pressure level is computed, and the Campbell diagram, covering rotational speeds from 500 RPM to 1000 RPM, is assembled in Figure 11.31.

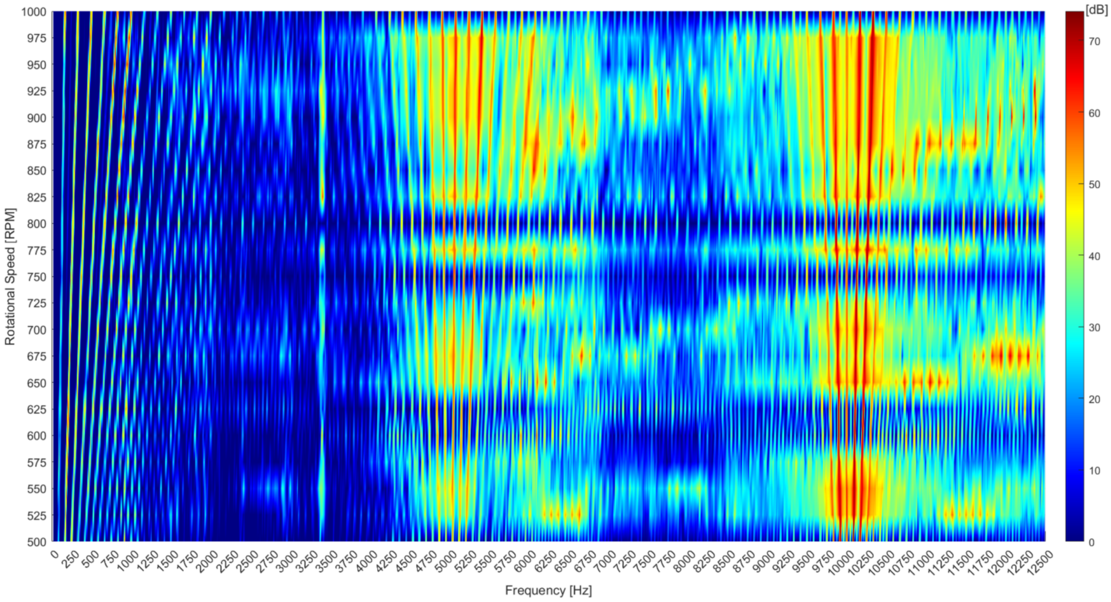

Figure 11.31: Acoustic pressure level Campbell diagram.

The spectral leakage, already observed in the EM simulation and resulting from the still present lack of periodicity in some rotational speeds, appears exacerbated in the acoustic pressure level results. As for the EM force results, the e-motor orders are clearly visible, while the PWM-induced harmonics exhibit the characteristic smearing effect. From this preliminary analysis, the second harmonic of the PWM carrier frequency appears more prominently, compared to the first one, in contrast to the observations in the EM forces Campbell diagram.

The Campbell diagram analysis reveals that the contribution of the e-motor orders is less significant compared to that of the PWM harmonics. Furthermore, the second harmonic of the PWM carrier frequency is more prominent than the first harmonic. These observations contrast with the behavior seen at the level of EM forces.

To better analyze the results, a single rotational speed of 800 RPM is displayed in Figure 11.32. This speed was chosen because it exhibits perfect periodicity of both the fundamental and the PWM-induced harmonic signals, thereby eliminating the smearing effect and enabling a clearer analysis.

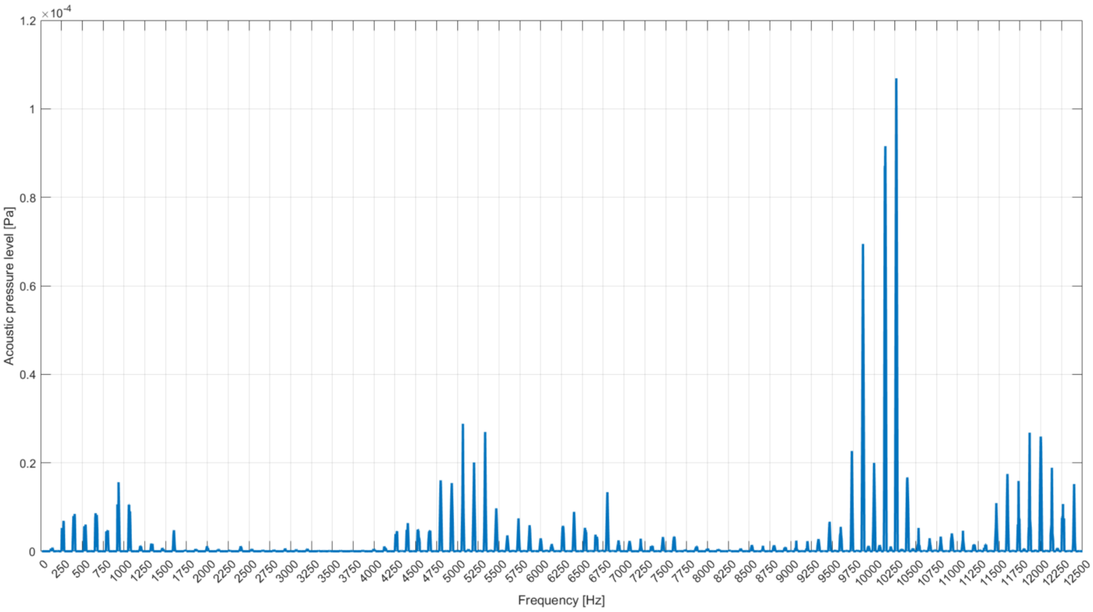

Figure 11.32: Frequency spectrum of the acoustic pressure level at 800 RPM

Contrary to the observations in the EM-forces analysis, the frequency spectrum of the acoustic pressure level at a rotational speed of 800 RPM shows that the contribution of the e-motor orders is less significant than that of the PWM harmonics. Notably, the second harmonic of the PWM carrier frequency is the primary contributor and is responsible for the presence of a high-pitch noise at approximately 10,000 Hz. This finding aligns with previous studies in the literature [9] [2] [4].

12. Results of the State Space framework

The State Space framework consists of the 1D electric drive unit model, shared between the two simulation frameworks, the 2D complete electromagnetic model, and the State Space model. The working conditions implemented in the 1D electric drive uni model are the same as in the FE framework workflow, ensuring complete consistency between the final results.

For the State Space framework workflow, it was decided to simulate the steady-state conditions at a rotational speed of 1000 RPM. This speed was chosen because it exhibits perfect periodicity of both the fundamental and PWM-induced harmonic signals, thereby eliminating the smearing effect and enabling clearer analysis.

The 2D complete electromagnetic model computes the time-domain lumped forces, which are then fed into the State Space model. Figure 12.1 shows the lumped forces for two different teeth at a rotational speed of 1000 RPM.

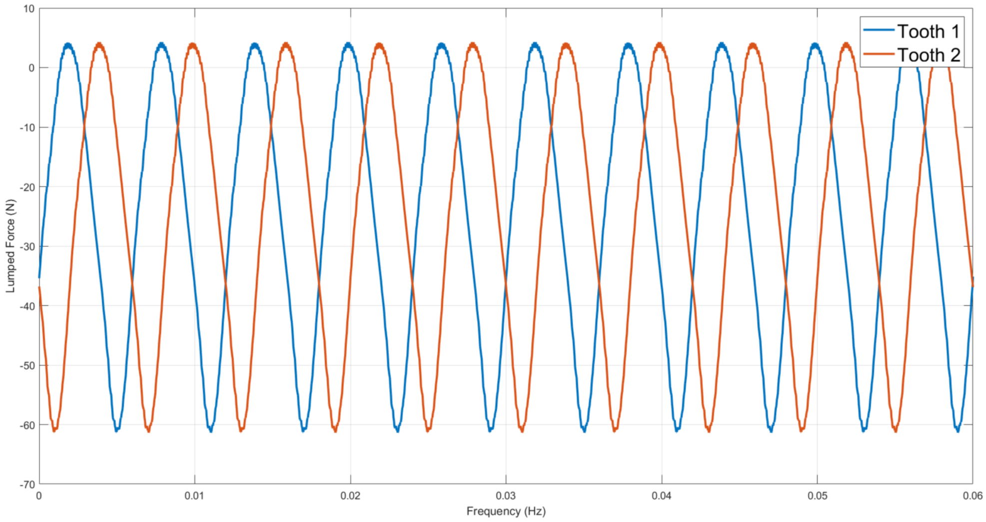

Figure 12.1: Lumped forces for different teeth.

The results displayed in Figure 12.1 show the lumped forces computed for two different teeth. These forces have the same amplitude but are out of phase, as expected. The lumped forces are a function of the rotor angle, with the oscillations originating from variations in the electromagnetic characteristics within the air gap. The oscillations in the EM force have a fundamental frequency that directly causes the slotting effect. Additionally, there are secondary harmonics induced by the PWM, which are linked to the harmonics of the PWM carrier frequency.

The computed EM lumped forces account for the entire tooth, including its three-dimensional expansion. The State Space model is configured to have 10 different application points for each tooth. Therefore, the lumped force resulting from the 2D electromagnetic model is evenly distributed on those 10 points.

The State Space model receives the lumped forces as inputs, distributed on 10 points for each of the 15 teeth. It computes the acoustic pressure level for the same time domain as the lumped forces, which then is processed with a Fourier Transform. The resulting frequency spectrum of the acoustic pressure level referring to a rotational speed of 1000 RPM is depicted in Figure 12.2.

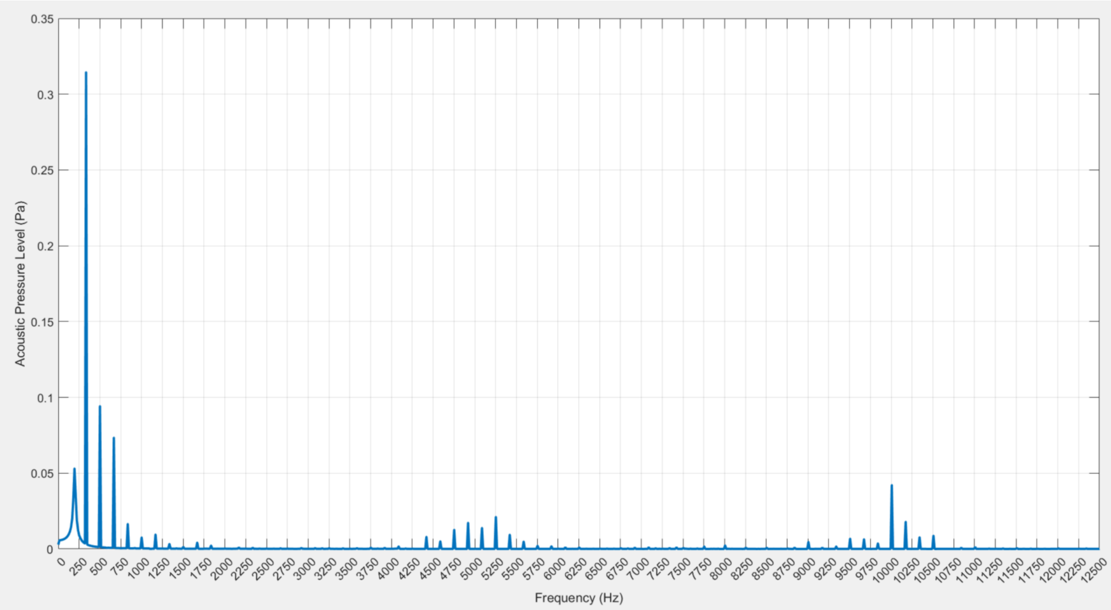

Figure 12.2: Acoustic pressure level frequency spectrum.

Figure 12.2 illustrates the e-motor orders and the PWM-induced carrier frequency harmonics, resembling the frequency spectrum obtained from the FE simulation framework. A detailed comparison of the different frameworks results is provided in Section 12.1.

12.1 Comparative Analysis of Framework Results.

The comparison between the FE simulation framework and the State Space simulation framework is illustrated in Figure 12.4.

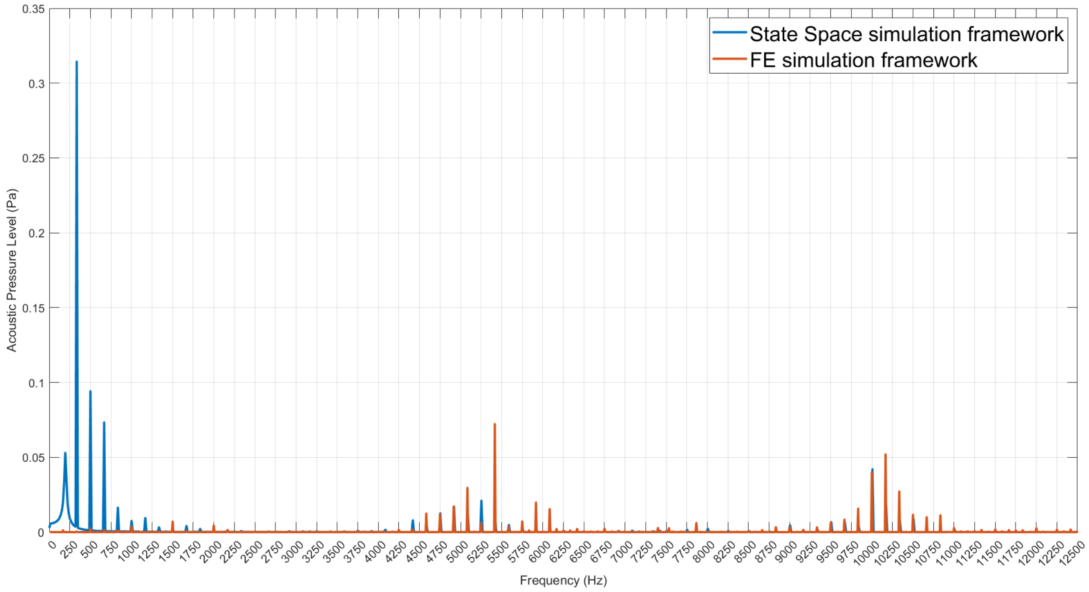

Figure 12.3: Comparison between different frameworks results.

The direct comparison of the acoustic pressure level results reveals that the State Space simulation framework exhibits a much more pronounced presence of e-motor orders in the frequency spectrum compared to the results obtained from the FE simulation framework. The PWM harmonics appear to match more between the two trends but a magnification is necessary to better analyse the results.

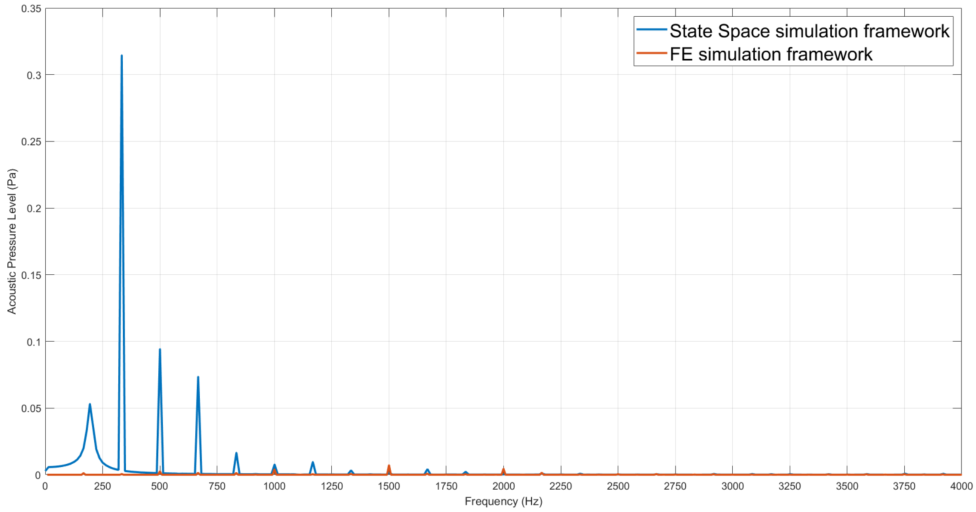

Figure 12.4: E-motor orders results comparison.

The comparison focusing on e-motor orders, illustrated in Figure 12.4, shows that the State Space simulation framework exhibits a much more pronounced presence of e-motor orders compared to the alternative framework's results. The first harmonic of the e-motor order, located at approximately 220 Hz, displays a 'smearing effect' similar to the one discussed in Section 11.4. The difference in trends arises from the derivation of the State Space model. Specifically, Figure 12.5 depicts the Simcenter Testlab modal synthesis, which approximates the input FRFs to derive the modal model.

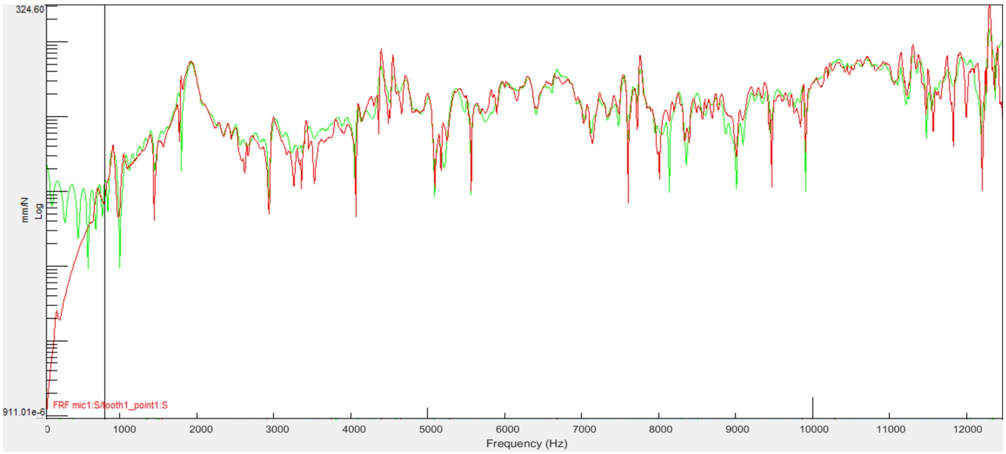

Figure 12.5: Testlab FRFs fitting tool.

The modal model is then used to derive the State Space model, as described in Chapter 10. As shown in Figure 12.5, the fitted FRFs do not match the original signal in the range from 0 Hz to 1000 Hz. This mismatch is due to an intrinsic limitation in the modal fitting procedure that is not able to reproduce a good fitting at the lowest frequencies. this is the cause of the differences in the acoustic pressure level results presented in Figure 12.4. Therefore, it can be concluded that the e-motor order-related frequencies are not accurately represented by the State Space framework.

Figure 12.6 illustrates the acoustic pressure level comparison focusing on the PWM-related harmonics.

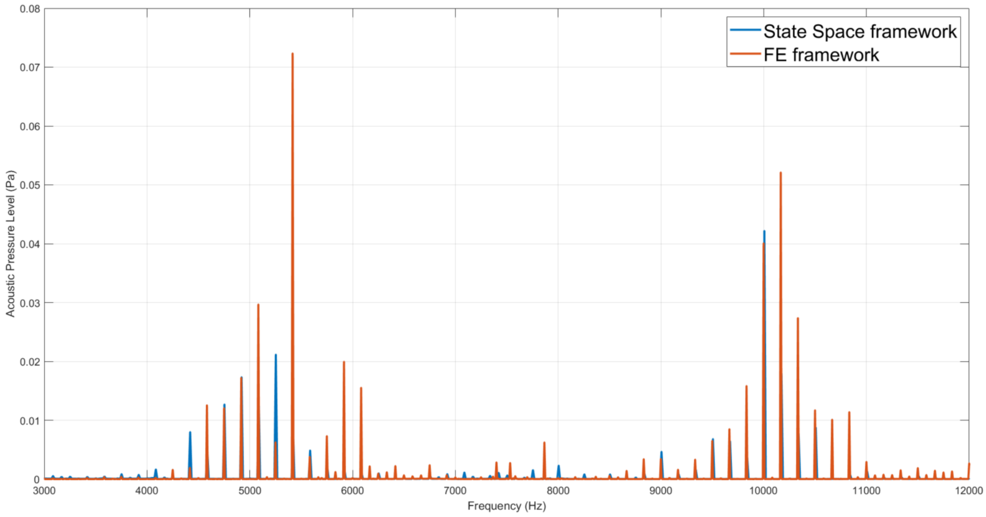

Figure 12.6: PWM harmonics results comparison.

The frequency range from 1000 Hz to 12500 Hz is characterized by a satisfactory match between the approximated signal and the original FRF, as illustrated in Figure 12.5. The PWM-related harmonics show a degree of coherence between the results, but there are still some inconsistencies between the outputs of the two different frameworks. Both the first and second harmonics of the carrier frequency exhibit the same principal peaks and sidebands, but their amplitudes differ.

The discrepancy can be attributed to several factors. Firstly, the approximation of the FRF is still not perfectly accurate. Secondly, the workflow approximates the lumped forces to have the same intensities across the 10 points along the longitudinal length of the teeth. This approach lacks accuracy and is a consequence of using a 2D EM model. With a 3D model, it would be possible to compute more accurate lumped forces with varying intensities acting on the 10 points of the teeth.

A third possible cause is that the 10 points are insufficient to accurately represent the EM excitation acting on the inner surface of the stator. The FE framework performs better in this regard because it computes and utilizes surface nodal densities as dynamic excitation. Lastly, the discrepancy may also be linked to the fact that the FE simulation framework considers only the dynamic excitation from the inner surface of the stator, mesh mapping the results as described in Section 11.3. Conversely, the State Space model computes the lumped forces by integrating the EM excitation acting along the entire perimeter of the stator tooth.

The comparative analysis of the framework results reveals that the State Space simulation frameworks still have certain limitations that impact the final outcomes. To enhance accuracy, several improvements can be made to the framework:

- **3D EM Model for Lumped Forces**: Computing the Lumped forces using a 3D EM model would allow for differentiation across various points on the teeth, providing a more precise representation.
- **Increasing the Number of Acting Points**: Increasing the number of acting points for the Lumped EM forces would better capture the dynamic excitation acting on the stator, thereby improving the overall simulation accuracy.
- **Improving Testlab Modal Synthesis Procedure**: Addressing the inherent limitations of the Testlab modal synthesis procedure could enhance the accuracy of acoustic pressure level results, particularly in the lower frequency range.

By implementing these modifications, the State Space framework can achieve a higher level of accuracy and provide more reliable simulation results. Despite its limitations, the State Space framework remains a valid option for modeling the vibroacoustic behavior of electric machines due to its intrinsic computational efficiency. Table 12.1 lists the computational time required by the State Space model and the time required by the 3D vibroacoustic model to compute the results depicted in Figure 12.4.

Model	Computational Time
3D vibroacoustic model	8 min 12 sec
State Space model	22 sec

Table 12.1: Comparison in the models computational time.

Bibliography

[1] Niccolò Remus, Mohammad Sedigh Toulabi, Shruthi Mukundan, Himavarsha Dhulipati, Wenlong Li, Colin Novak, and Narayan C Kar. «Electromagnetic noise and vibration in pmsm and their sources: An overview». In: *2020 IEEE Canadian Conference on Electrical and Computer Engineering (CCECE).* IEEE. 2020, pp. 1–4 (cit. on pp. 1, 13).

[2] Koen Delaere, Ward Heylen, Ronnie Belmans, and Kay Hameyer. «Comparison of induction machine stator vibration spectra induced by reluctance forces and magnetostriction». In: *IEEE Transactions on Magnetics* 38.2 (2002), pp. 969–972 (cit. on pp. 1, 13, 101).

[3] Rajesh M Pindoriya, Rishi Kant Thakur, Bharat Singh Rajpurohit, and Rajeev Kumar. «Numerical and experimental analysis of torsional vibration and acoustic noise of PMSM coupled with DC generator». In: *IEEE Transactions on Industrial Electronics* 69.4 (2021), pp. 3345–3356 (cit. on pp. 1, 2).

[4] Etienne Parizet, Karl Janssens, Pedro Poveda-Martínez, Andreia Pereira, Jakub Lorencki, and Jaime Ramis-Soriano. «NVH analysis techniques for design and optimization of hybrid and electric vehicles». In: *NVH analysis techniques for design and optimization of hybrid and electric vehicles* (2016), pp. 313–355 (cit. on pp. 1, 101).

[5] Mahmoud Elkafafy and Bart Peeters. «Robust Identification of Stable MIMO Modal State Space Models». In: *Topics in Modal Analysis & Parameter Identification, Volume 8: Proceedings of the 40th IMAC, A Conference and Exposition on Structural Dynamics 2022.* Springer. 2022, pp. 81–95 (cit. on pp. 3, 69).

[6] Philip J Berry and Essam S Hamdi. «An investigation into damper winding failure in a large synchronous motor». In: *2015 50th International Universities Power Engineering Conference (UPEC).* IEEE. 2015, pp. 1–4 (cit. on p. 6).

[7] Tiandong Xi, Sebastian Kehne, Marcel Fey, and Christian Brecher. «Application of optimal control for synchronous reluctance machines in feed drives of machine tools». In: *2022 International Conference on Electrical, Computer and Energy Technologies (ICECET).* IEEE. 2022, pp. 1–6 (cit. on p. 6).

[8] Hyeoung Seob Kim, Sun-Ki Hong, Ji Hoon Han, and Dong Jin Choi. «Dynamic modeling and load characteristics of hysteresis motor using preisach model». In: *2018 21st International Conference on Electrical Machines and Systems (ICEMS)*. IEEE. 2018, pp. 560–563 (cit. on p. 7).

[9] Nicolò Salamone, Claudio Colangeli, Fabio Bianciardi, Korcan Kucukcoskun, Mathieu Sarrazin, Karl Janssens, and Wim Desmet. «Multi-Physic Analysis of Power Electronic Control Parameters in a Simulation Framework». In: *Surveillance, Vibrations, Shock and Noise*. 2023 (cit. on pp. 9, 14, 30, 78, 88, 101).

[10] Ehab Sayed, Yinye Yang, Berker Bilgin, Mohamed H Bakr, and Ali Emadi. «A comprehensive review of flux barriers in interior permanent magnet synchronous machines». In: *IEEE Access* 7 (2019), pp. 149168–149181 (cit. on p. 9).

[11] Jacek F Gieras, Chong Wang, and Joseph Cho Lai. *Noise of polyphase electric motors*. CRC press, 2018 (cit. on pp. 13, 14).

[12] Raphaël Pile, Emile Devillers, and Jean Le Besnerais. «Comparison of Main Magnetic Force Computation Methods for Noise and Vibration Assessment in Electrical Machines». In: *IEEE Transactions on Magnetics* 54.7 (2018). Accessed: 2024-06-29, pp. 1–13. DOI: `10.1109/TMAG.2018.2828388`. URL: `https://hal.science/hal-01960033` (cit. on pp. 13, 14, 42, 56).

[13] U. Kim and D.K. Lieu. «Magnetic field calculation in permanent magnet motors with rotor eccentricity: with slotting effect considered». In: *IEEE Transactions on Magnetics* 34.4 (1998), pp. 2253–2266. DOI: `10.1109/20.703863` (cit. on p. 14).

[14] Liting Jing, Jiaxin Wang, Jing Xie, Di Feng, Jianxiang Wang, Xiang Peng, and Shaofei Jiang. «A quantitative simulation-based conceptual design evaluation approach integrating bond graph and rough VIKOR under uncertainty». In: *Journal of Cleaner Production* 380 (2022), p. 134928 (cit. on p. 20).

[15] Peter J Gawthrop and Geraint P Bevan. «Bond-graph modeling». In: *IEEE Control Systems Magazine* 27.2 (2007), pp. 24–45 (cit. on p. 20).

[16] Surajit Chattopadhyay, Madhuchhanda Mitra, Samarjit Sengupta, Surajit Chattopadhyay, Madhuchhanda Mitra, and Samarjit Sengupta. «Clarke and park transform». In: *Electric Power Quality* (2011), pp. 89–96 (cit. on pp. 23, 28–30).

[17] Sergio Galeani, Sophie Tarbouriech, Matthew Turner, and Luca Zaccarian. «A tutorial on modern anti-windup design». In: *European Journal of Control* 15.3-4 (2009), pp. 418–440 (cit. on p. 25).

[18] C Bohn and DP Atherton. «An analysis package comparing PID anti-windup strategies». In: *IEEE Control Systems Magazine* 15.2 (1995), pp. 34–40 (cit. on p. 26).

[19] Joris Lemmens, Piet Vanassche, and Johan Driesen. «PMSM drive current and voltage limiting as a constraint optimal control problem». In: *IEEE Journal of emerging and selected topics in power electronics* 3.2 (2014), pp. 326–338 (cit. on p. 27).

[20] Siemens Digital Industries Software. *Simcenter Amesim Help Documentation*. Available with Simcenter Amesim software. 2024 (cit. on p. 29).

[21] Siemens Digital Industries Software. *Simcenter 3D Solution Guide*. Accessed: 2024-06-29. 2024. URL: `https://resources.sw.siemens.com/en-US/e-book-simcenter-3d-solution-guide` (cit. on pp. 39, 63).

[22] Somà Aurelio. *Introduzione al metodo FEM*. Progettazione di prodotto con metodi numerici, Politecnico di Torino. Available only attending the course. 2022 (cit. on p. 40).

[23] Kenneth J. Baumeister. *Finite Element Analysis of Electromagnetic Propagation in an Absorbing Wave Guide*. Tech. rep. NASA-TM-88866. Accessed: 2024-06-29. NASA Lewis Research Center, 1986. URL: `https://ntrs.nasa.gov/api/citations/19870008958/downloads/19870008958.pdf` (cit. on p. 40).

[24] CJ Carpenter. «Surface-integral methods of calculating forces on magnetized iron parts». In: *Proceedings of the IEE-Part C: Monographs* 107.11 (1960), pp. 19–28 (cit. on p. 41).

[25] Jian-Ming Jin. *The Finite Element Method in Electromagnetics*. Third Edition. Wiley, 2014. ISBN: 978-1-118-57136-1 (cit. on p. 41).

[26] Korchan Kucukcoskun. *Simcenter 3D Low Frequency EM Tutorial: IPM Traction Motor 2D Partial Model*. Accessible with software purchase. 2022 (cit. on p. 45).

[27] Siemens Digital Industries Software. *Simcenter Pre-Post*. Version 23062. Documentation accessible with software purchase. Siemens Digital Industries Software. Plano, TX, 2023 (cit. on pp. 55, 57, 63).

[28] JM Roesset, RV Whitman, and R Dobry. «Modal analysis for structures with foundation interaction». In: *Journal of the Structural Division* 99.ST10 (1973), pp. 2109–2122. DOI: `10.1061/JSDEAG.0003457`. URL: `https://ascelibrary.org/doi/abs/10.1061/JSDEAG.0003457` (cit. on p. 55).

[29] Thomas D Rossing. «Modal analysis». In: *Springer Handbook of Acoustics*. Springer, 2007, pp. 1165–1177 (cit. on p. 55).

[30] Tata Steel Europe. *M270-35A Technical Specifications.* Tech. rep. 2024. URL: `https://www.tatasteeleurope.com/sites/default/files/m270-35a_1.pdf` (cit. on p. 58).

[31] AZoM Materials. «Aluminium / Aluminum 2014 Alloy (UNS A92014)». In: (Sep 27 2012). URL: `https://www.azom.com/article.aspx?ArticleID=6614` (cit. on p. 58).

[32] Hans Zhou. *How to differentiate between 304 stainless steel plate and 201 stainless steel plate.* 2023. URL: `https://www.linkedin.com/pulse/how-differentiate-between-304-stainless-steel-plate-201-` (cit. on p. 58).

[33] Zhiqiang Wang, Bo Yao, Liyan Guo, Xuefeng Jin, Xinmin Li, and Huimin Wang. «Initial rotor position detection for permanent magnet synchronous motor based on high-frequency voltage injection without filter». In: *World Electric Vehicle Journal* 11.4 (2020), p. 71 (cit. on p. 79).

[34] Takafumi Hara, Toshiyuki Ajima, Yosuke Tanabe, Masanori Watanabe, Katsuhiro Hoshino, and Kazuto Oyama. «Analysis of vibration and noise in permanent magnet synchronous motors with distributed winding for the PWM method». In: *IEEE Transactions on Industry Applications* 54.6 (2018), pp. 6042–6049 (cit. on pp. 88, 89, 96).

[35] M Glesser, S Ni, K Degrendele, S Wanty, and J Le Besnerais. «Sound quality analysis of electric drive units under different switching control strategies». In: *November 2021 Conference: SIA Automotive NVH Confort Conference At: Le Mans.* Vol. 11. 2021 (cit. on p. 88).

[36] Emile Devillers. *What is an electrical/mechanical order?* 2022. URL: `https://www.linkedin.com/pulse/what-electricalmechanical-order-eomys/` (cit. on p. 89).

[37] Douglas A Lyon. «The discrete fourier transform, part 4: spectral leakage». In: *Journal of object technology* 8.7 (2009) (cit. on pp. 89, 90).

[38] Daan Huybrechs. «On the Fourier extension of nonperiodic functions». In: *SIAM Journal on Numerical Analysis* 47.6 (2010), pp. 4326–4355 (cit. on p. 90).